The surrogate-reaction method and excitation-energy sorting in nuclear fission

Beatriz Jurado

▶ **To cite this version:**

Beatriz Jurado. The surrogate-reaction method and excitation-energy sorting in nuclear fission. Nuclear Experiment [nucl-ex]. Université de Bordeaux, 2015. tel-01262708

HAL Id: tel-01262708
https://hal.in2p3.fr/tel-01262708

Submitted on 27 Jan 2016

HAL is a multi-disciplinary open access archive for the deposit and dissemination of scientific research documents, whether they are published or not. The documents may come from teaching and research institutions in France or abroad, or from public or private research centers.

L'archive ouverte pluridisciplinaire **HAL**, est destinée au dépôt et à la diffusion de documents scientifiques de niveau recherche, publiés ou non, émanant des établissements d'enseignement et de recherche français ou étrangers, des laboratoires publics ou privés.

Habilitation à diriger des recherches

présentée par

BEATRIZ JURADO

The surrogate-reaction method and excitation-energy sorting in nuclear fission

Soutenue publiquement au CENBG le 27/03/2015 devant le jury composé de :

Rapporteurs	Jérôme Giovinazzo	Chargé de recherche CNRS CENBG
	Magne Guttormsen	Professeur Université d'Oslo (*Président*)
	René Reifarth	Professeur Université de Francfort
Examinateurs	Fanny Farget	Chargée de recherche CNRS GANIL
	Vincent Méot	Directeur de Recherche CEA-DAM-DIF
	Karl-Heinz Schmidt	Chercheur émérite GSI Darmstadt

Acknowledgments

I have not always been very motivated by the idea of writing a “habilitation”, but after all I am rather happy of having done it! By writing these pages I have learnt a lot, taken a global view, found connexions between subjects that were apparently rather distinct and carefully thought about future perspectives. When I look back to the previous ten years I see some tough moments but also extremely pleasant moments where I felt so touched by the beauty of nature. It is such a great privilege to work on research!

First of all I would like to thank Fanny, Jérôme, Karl-Heinz, Magne, René and Vincent. It was a great honour to have you in my habilitation committee! Each of you is a model for me and I deeply wish we will continue (start) to work together. Particular thanks go to Karl-Heinz. You have taught me so many things (since my PhD!) and made me enjoy physics; if I am here today is to a great extent thanks to you! I am always amazed by the way you can “tame” nature and “see” the underlying simplicity behind very complex observations…

I would also like to express my gratitude to Grégoire, Guillaume and Quentin, the three PhD students with whom I have intensively worked over the last ten years. It was a great pleasure to work and learn with you! Grazie mille Paola for carefully reading the manuscript and for all your “nasty” questions that made me think a lot! I am also very grateful to all the members (former and present) of the ACEN group of the CENBG. Special thanks go to all the colleagues from the CEA, IPNO and the University of Oslo for their help during the experiments, without you we wouldn’t have made it! Merci infiniment à tous les groupes et services du CENBG et tout particulièrement à Christian Guitou pour sa profonde gentillesse. I am also deeply grateful to Manfred from the MPI Heidelberg for his crucial help in establishing the feasibility of in-ring fission experiments, I really hope we will make these measurements one day…!

Enfin, j’aimerais exprimer ma plus profonde gratitude à ma famille Medhi et Sabine (bolilla eins et bolilla zwei!) pour TOUT. Vous êtes mes racines, d’où je puise mon énergie et mon équilibre, vous êtes mon « chez moi ».

Preface

This manuscript summarises the main activities that I have carried out during the last ten years of research at the Centre d'Études Nucléaires de Bordeaux-Gradignan (CENBG). It is, to a great extent, a synthesis of nine articles. They can be consulted by the reader that would like to have more detailed information. These articles are denoted as Article I, II… all along the manuscript. The manuscript is intended to be accessible to PhD students not familiar with the topic.

Chapter 1 recalls some of the basic ideas of statistical mechanics and discusses the applicability of the concepts to nuclei. Some of these concepts, in particular the concept of statistical equilibrium, are essential for the topics covered by chapters 2 and 3. Chapter 2 summarises the studies performed by the CENBG collaboration on the surrogate-reaction method in the last ten years. Chapter 3 summarises part of the work done on the modelling of nuclear fission in collaboration with Karl-Heinz Schmidt, it considers the partition of excitation energy and unpaired nucleons in fission on the basis of statistical mechanics. Chapters 2 and 3 contain the bulk of my work, each of them has its own introduction and conclusion sections. Chapter 4 presents the medium and long-term experimental perspectives for the topics described in chapters 2 and 3.

Beatriz Jurado

Gradignan, 16 March 2015

Contents

Chapter 1: Statistical mechanics and nuclei

Some concepts of statistical mechanics will be central all along this manuscript. Therefore, in this chapter we will briefly recall some of the main ideas of this fundamental theory, which is, together with quantum mechanics and relativity, one of the cornerstones of modern physics. To prepare this chapter we have used the excellent book “Physique statistique” by B. Diu et al. [Diu01], which we strongly recommend to anyone interested in the subject.

The aim of statistical mechanics is to explain the behaviour of macroscopic systems on the basis of their microscopic characteristics. Quantum mechanics describes the properties and the evolution of a physical system on a microscopic scale. Therefore, statistical mechanics is built on the basis of quantum mechanics. If the Hamiltonian of the system is independent of time, its eigenstates are stationary: if the system is in one eigenstate (or a linear combination of eigenstates) it will remain indefinitely in that state and the system properties will not vary with time. However, the Hamiltonian of a macroscopic system can only be defined approximately and as a consequence its eigenstates are not stationary, the system evolves continuously from one quantum state to the other in an uncontrolled manner. In that situation, the macroscopic state (often named “macrostate” in literature) is a statistical mixture of quantum-mechanical states i (“microstates”) characterized by an ensemble of probabilities $\{P_i\}$ of finding the system in that particular microstate. Nuclei are not macroscopic systems in a strict sense. However, in many cases (e.g. for mid-shell medium and heavy nuclei) nuclei are sufficiently complex quantum systems for requiring a statistical description as the one we have just described.

The fact that the system evolves continuously from one microstate to another leads to fluctuations in time of the associated physical quantities. Therefore, in statistical mechanics one has to consider the time average of the physical quantities. This procedure provides an accurate description of the properties of the macrostate as long as the fluctuations remain small compared to the average value. The importance of fluctuations depends strongly on the size of the system. To illustrate this, let us consider a container with a gas of A molecules and let us count the number of molecules in one half of the container. The number of molecules measured as function of time will show fluctuations around the mean value $A/2$ and the relative amplitude of the fluctuations can be quantified by $\sqrt{A/2}/(A/2)$. Therefore, the relative impact of fluctuations will decrease as A increases. In nuclei, the microstates associated to a macrostate can be very different, e.g. the intrinsic excitation energy may be shared by a strongly different number of nucleons. In addition, because of the limited number of nucleons, the number of microstates is much smaller than for a macroscopic system, and the relative contribution of each microstate will be larger. For these reasons, fluctuations can be significant when dealing with nuclei.

Determining the time averages of the properties of one unique system requires that the microscopic fluctuations are faster than the macroscopic evolution. To avoid this constraint,

one replaces time averages of one particular system by averages over a statistical ensemble including a large number of identical systems. One distinguishes between different types of statistical ensembles. The microcanonical ensemble is made of a large number of isolated systems. Isolated systems cannot exchange energy and particles with the environment. Therefore, the energy and the number of particles remain constant and serve, among other conserved quantities, to define the macrostate. In the microcanonical ensemble all the systems have the same energy and number of particles leading to the same macrostate, whereas the microstates associated to each system of the ensemble differ one from the other. In the canonical ensemble the systems are not isolated, they are in contact with a thermostat or a heat bath that plays the role of an energy reservoir. In this case, the energy of the macrostate can vary significantly with time. The macrostate is characterised by the temperature, which is constant and equal to the temperature of the thermostat.

Before decay, nuclei are isolated systems and are therefore best described with the microcanonical ensemble. However, in nuclear fission for example one often considers the evolution of collective nuclear degrees of freedom assuming that these degrees of freedom are coupled to a heat bath formed by the rest of nuclear degrees of freedom (intrinsic and collective). In that case, the collective nuclear degree of freedom is best represented by the canonical ensemble. In this manuscript, we will mainly consider the evolution of nuclei and not of particular nuclear degrees of freedom. Therefore, here we will only deal with the microcanonical ensemble.

For an isolated system, the time evolution of the probability P_i of finding the system in the microstate i is given by:

$$\frac{dP_i}{dt} = \sum_j \left[a_{ij} P_j(t) - a_{ji} P_i(t) \right] \tag{1}$$

where a_{ij} and a_{ji} represent the transition probabilities per unit of time from the microstate j to the microstate i and vice versa. The transition probabilities a_{ij} verify:

$$a_{ij} = a_{ji} \tag{2}$$

and

$$a_{ij} = 0 \text{ if } E_i \neq E_j \tag{3}$$

Eqs. (1-3) say that the probability of finding the system in the microstate i at a given time t is equal to the population of that state by a transition from any other microstate j of the same energy E_i, minus the depopulation due to a transition from the state i to any other microstate j that satisfies energy conservation.

At statistical equilibrium, the population probabilities P_i are independent of time, i.e.:

$$\frac{dP_i}{dt} = \sum_j \left[a_{ij} P_j(t) - a_{ji} P_i(t) \right] = 0 \tag{4}$$

which means that in statistical equilibrium the population probability P_i of a state is independent of time because the population of the microstate i is exactly compensated by its depopulation, and not because the system is always in the same microstate. It can be shown [Diu01] that for an isolated system with energy E there is only one solution to the system of differential equations represented by eq. (4). This solution corresponds to the macrostate in which all the microstates that are accessible have equal population probabilities P_i. In other words, for an isolated system in statistical equilibrium we have:

$$\begin{aligned} P_i^{eq}(E) &= \frac{1}{N(E)} = \frac{1}{\Omega(E)dE} \; if \; E_i = E \\ &= 0 \qquad if \; E_i \neq E \end{aligned} \tag{5}$$

where N is the number of available microstates and Ω is the density of available microstates per unit of energy. It can be shown [Diu01] that for $t \to \infty$ the solution of eq. (1) is eq. (5), independently of the initial ensemble of population probabilities $\{P_i(t_0)\}$. This is a very fundamental result, since it implies that any isolated system left to its own evolves towards the macrostate of statistical equilibrium and will reach it if we wait a sufficiently long time. The relaxation time, i.e. the time the system needs to reach statistical equilibrium, depends on the specific values of the transition probabilities a_{ij}. However, due to the complexity of the system, it is usually not possible to determine exactly the coefficients a_{ij}. Therefore, to evaluate the relaxation time, one often uses a simplified physical model or considers it as a parameter that is empirically determined.

In statistical mechanics, the entropy is defined as:

$$S(t) = -k \sum_i P_i(t) \ln\left[P_i(t) \right] \tag{6}$$

where k is Boltzmann constant, that we will set equal to 1 all along this manuscript. It can be shown that the entropy of the system is maximum if all the microstates are equiprobable and $P_i = 1/N$. In that case,

$$S_{\max} = \ln N = \ln \Omega \tag{7}$$

where we have neglected the quantity $\ln(dE)$. Therefore, when an isolated system out of equilibrium is left to its own, its evolution is accompanied of a continuous increase of its entropy. This spontaneous evolution stops when the system reaches statistical equilibrium, where all the accessible microstates are equally probable and the entropy is maximum.

From the definition of the entropy given in eq. (6), it is easily understandable that the entropy measures the lack of information we have of the system. If for example we know that the system is in a particular microstate m, then all the population probabilities P_i will be 0 except

P_m=1 and from eq. (6) it follows that the entropy is 0. In this case we have the complete information on the system, we know exactly in which microstate the system is. On the other hand, when all the population probabilities are equal, the lack of information on our system is maximum, because we cannot say that one microstate has a higher probability to be populated than any other. In addition, we expect intuitively that the larger the number of available microstates, the larger will be the lack of information on the system, which is clearly reflected by eq. (7).

We define the microcanonical temperature T as:

$$T = \left(\frac{dS}{dE} \right)^{-1} \tag{8}$$

and the microcanonical chemical potential μ as:

$$\mu = -T \cdot \left(\frac{dS}{dA} \right) \tag{9}$$

where A is the number of microscopic constituents of the system. As for the entropy, the temperature and the chemical potential are quantities associated to the macrostate of a given system. It makes for example no sense to talk about the temperature of a microstate of the system.

In Chapter 3, we will apply statistical mechanics to the situation where two nuclei are in thermal contact, which takes place during the fission process. We will show now how a system made of two subsystems in thermal contact can be described in the frame of statistical mechanics. If an isolated system consists of two isolated systems at equilibrium with a number of microstates N_1 and N_2, we can associate to each microstate of system 1 any microstate of system 2. Therefore, the total number of microstates of the whole system N_{tot} at equilibrium is:

$$N_{tot} = N_1 \cdot N_2 \tag{10}$$

Using eqs. (7) and (10) we have that the total entropy of the global system at equilibrium S_{tot} is:

$$S_{tot} = S_1 + S_2 \tag{11}$$

Suppose we now set the two subsystems defined above in thermal contact, this means that the two sub-systems can exchange energy. We suppose that the global system is isolated. The Hamiltonian H_{tot} of the global system is:

$$H_{tot} = H_1 + H_2 + H_{12} \tag{12}$$

where the term H_{12} represents the interaction between the two systems. If the coupling between the two systems is weak enough for the term H_{12} to be negligible with respect to the

individual Hamiltonians H_1 and H_2, the energies E_1, E_2 of the individual systems will continue to be well defined. For weak coupling, the eigenstates of H_{tot} are the eigenstates of H_1 and H_2 and the total energy of the system E_{tot} is:

$$E_{tot} = E_1 + E_2 \tag{13}$$

Since the global system is isolated, the total energy E_{tot} is conserved but the individual energies of the subsystems E_1 and E_2 can vary due to the thermal coupling. At statistical equilibrium the total number of microstates of the global system at energy E_{tot} is:

$$N_{tot}(E_{tot})=N_1(E_1)\cdot N_2(E_{tot}-E_1) \tag{14}$$

For the coupling term H_{12} to be negligible, the interaction forces between the microscopic constituents of the two subsystems have to be of short range. In that case, most of the microscopic constituents of the individual subsystems do not “feel” the presence of the other system. In nuclei, this is fulfilled by the nuclear force but not for the Coulomb force between the protons of both subsystems. This issue will be further discussed in Chapter 3.

Chapter 2: The surrogate-reaction method

Neutron-induced reaction cross sections of short-lived nuclei are important in several domains such as fundamental nuclear physics, nuclear astrophysics and applications in nuclear technology. These cross sections are key input information for modelling stellar element nucleosynthesis via the s and r-processes [Rei14-2]. They play also an essential role in the design of advanced nuclear reactors for the transmutation of nuclear waste or reactors based on innovative fuel cycles like the Th/U cycle. The most hazardous type of wastes currently generated by nuclear power plants are the fission products and the so-called minor actinides. Although they represent only about 0.2% of the total volume of the generated wastes, they concentrate 95% of the radioactivity [Cea14]. The produced minor actinides are mainly Np, Am and Cm isotopes. The envisaged waste-management strategies combine waste "incineration" and storage in deep and stable geological sites [Cea14]. The term "incineration" means here to transmute these heavy nuclei into less radioactive species by making them fission in dedicated nuclear reactors. Simulating the incineration capability of a reactor requires an accurate knowledge of the neutron-induced fission and capture cross sections of these minor actinides. However, very often these cross sections are extremely difficult (or even impossible) to measure due to the high radioactivity of the targets involved.

Most of the minor actinides decay by alpha emission, but some of them fission spontaneously and therefore also emit neutrons (between 2 and 3 neutrons per fission event, see Chapter 3). The production of minor-actinide targets implies manipulating important quantities of radioactive material and the fabrication procedure is subject to significant radioprotection constraints. For this reason, it is rather difficult to find nowadays a laboratory where good-quality samples can be produced. Moreover, if the targets are not produced at the place where the measurement is foreseen, a special and costly transport has to be organized, not to mention the administrative work that has to be done in most countries for a laboratory to be authorized to import the samples. The handling of the sample during the experiment is also extremely complicated because one has to ensure that in case of damage the rests of the target sample remain confined in a container that is completely isolated from the environment. In addition, one has to deal with the background signal generated by the activity of the target in the detector. Indeed, one has for example to disentangle the neutron-induced fission events of interest from the pile-up of alpha particles and from the spontaneous-fission events originating from the radioactivity of the target. Finally, the intense flux of alpha particles can severely damage the detectors, in particular solid-state detectors.

The surrogate-reaction method is an indirect technique to determine cross sections for reactions that proceed through a compound nucleus, i.e. a nucleus that is in a state of statistical equilibrium. In this method, an alternative or surrogate reaction (e.g. a transfer or inelastic scattering reaction) is used to produce the same compound nucleus as in the neutron-induced reaction of interest. In some cases, the surrogate reaction involves a target-projectile combination that is experimentally more accessible. This makes the method extremely powerful since it gives access to neutron-induced cross sections of very short-lived nuclei that

cannot otherwise be measured. The surrogate-reaction method was developed at the Los Alamos National Laboratory by Cramer and Britt in the 70's [Cra70]. After sinking into oblivion in the 80's and 90's, it received renewed attention in the years 2000 when, almost simultaneously, two groups at the CENBG and the Lawrence Livermore National Laboratory in the USA, considered it for extracting cross sections of interest for reactor physics. The CENBG group first used the surrogate method to extract the neutron-induced fission and capture cross sections of ^{233}Pa [Pet04, Boy06]. This nucleus has a half life of only ($T_{1/2}$=27 d) and is important for the development of the Th/U cycle.

In the following, we will consider the compound-nucleus concept, which follows from the assumption of statistical equilibrium (discussed in Chapter 1), and is the basis of the surrogate-reaction method. We will present the surrogate-reaction method and discuss its validity. The experimental method used to extract the data via the surrogate method will be presented, with emphasis on the most important experimental difficulties. We will conclude this chapter by discussing our results and the short-term perspectives.

1. Compound-nuclear reactions

In the frame of an independent-particle model, the interaction of an incident particle with a nucleus with a radius of about 5 fm and a potential well depth of several 10 MeV leads to single-particle states that have a typical spacing of several hundred keV and widths of the order of 10 keV or larger. In addition, the interaction takes place in a time of the order of the time the impinging particle needs to traverse the target nucleus (less than 10^{-19}s) and the particle has a significant probability of not being absorbed. However, this picture is in complete disagreement with the results of the experiments carried out in the 1930's especially by Fermi and his group in Rome on thermal-neutron scattering by light and heavy nuclei. These results revealed the existence of numerous narrow resonances with average spacing D of few eV and a strong probability for the absorption of the neutrons with subsequent gamma emission. The width Γ of the resonances of the order of an eV implied through the uncertainty principle a life time of the excited states of about 10^{-15} s. To account qualitatively for the data, Bohr proposed his compound-nucleus model in 1936 [Boh36].

1.1. The compound-nucleus hypothesis

Bohr proposed that, because of the strong interaction, the projectile is captured by the target and shares its energy among all the nucleons in the compound system. It takes a long time (long in comparison with the time it takes a nucleon with the Fermi velocity to traverse the nucleus) for the compound nucleus to accidentally concentrate the available energy back onto a single nucleon which can then be reemitted. Since 10^{-14} or 10^{-15} s are typical lifetimes for electromagnetic transitions, gamma-ray emission may compete favourably with particle emission. The compound nucleus lives long enough for complete statistical equilibrium to be established and has no memory of its formation, so that the processes of formation and decay are completely independent of each other. This is the Bohr independence hypothesis, which makes it possible to calculate the cross sections of compound-nuclear reactions. Indeed, the associated cross section can be factorized in the product of the cross section for the formation

of the compound nucleus σ_{α}^{CN} in an entrance channel α and the probability P_{χ} that the compound nucleus decays via a decay channel χ:

$$\sigma_{\alpha\chi} = \sigma_{\alpha}^{CN} \cdot P_{\chi} \tag{1}$$

More precisely, the independence hypothesis states that the decay of a compound nucleus is determined entirely by its energy, angular momentum and parity. Therefore, the expression used before, that the compound nucleus forgets the way it was formed, is an oversimplification since it cannot forget the total energy of the system, which is conserved during the relaxation process (see Chapter 1). The angular momentum conservation in compound-nuclear reactions is demonstrated by the observed anisotropy of the angular distribution of the emitted particles. If the compound nucleus would forget the total angular momentum of the entrance channel, the angular distributions would be isotropic. This important aspect of the total angular-momentum conservation is sometimes forgotten in discussions regarding the validity of the compound-nucleus hypothesis.

Historically, the compound-nucleus hypothesis was explained by the high density of particles in the nucleus that would make extremely likely that an incoming neutron would share its energy completely before traversing the nucleus. This “blackness” of the nucleus was also in accord with the strength and the short range of the nuclear force. This strongly absorbing nuclear model is sometimes called the “black nucleus”. The properties of the compound nucleus were then predicted in analogy with the properties of a liquid drop, in which the heat energy is shared among all the molecules of the drop. The black-nucleus model gives an average cross section for the formation of a compound nucleus that is inversely proportional to the neutron velocity and therefore decreases monotonically with neutron energy.

During the period when neutron cross sections were first measured, the predictions of the black nucleus or the liquid-drop model seemed to be adequately fulfilled. Around 1945, several evidences indicated that the black-nucleus model was not completely correct. The existence of magic numbers showed that particles in the nucleus could move in the mean field generated by all the other particles, a behaviour not at all expected on the basis of a strongly interacting liquid-drop model. Another phenomenon that demanded modification of the black-nucleus model was the observation of forward-focussed, high-energy neutrons inelastic scattered by heavy nuclei. This type of events was qualitatively well explained by direct processes in which the incident particle is assumed to "kick" off particles from the nuclear surface without formation of a compound state. Definitive evidence for shell structure came from neutron cross sections themselves. Measurements with fast neutrons showed that the total cross sections did not always decrease monotonically with energy. The behaviour of the cross sections is more a smooth long-wavelength dependence on energy, superimposed on a monotonic decrease. A wavelike dependence in any physical phenomenon immediately suggests an optical interference effect. In fact, the observed effects are extremely close to those observed when light passes into a crystal sphere. Feshbach, Porter and Weisskopf [Fes54] developed the optical model, where the nucleus is represented by a potential with a real and an imaginary component. The imaginary component accounts for the absorption of the incident particle. From the magnitude of the imaginary component found necessary to fit

the experimental data it followed that a neutron may move a considerable distance in nuclear matter before being absorbed. The nucleus is not a “black box” but is partly transparent.

The optical model gives a common basis for explaining direct and compound reactions. Direct reactions are fast, peripheral reactions that involve only few interactions between the incident and target nucleons and bring only few degrees of freedom into play. More complex situations can occur in which the incident particle shares its energy with more and more nucleons, eventually leading to the formation of a compound nucleus. In fact, there is a continuous transition from direct reactions to compound-nuclear reactions. In between the two extremes there are intermediate situations in which a nucleon is emitted before relaxation, this is the so called pre-equilibrium decay. While the thermalisation hypothesis holds well for energies close to the neutron separation energy, pre-equilibrium emission typically occurs at neutron energies above at least 5-6 MeV [Esc12].

The compound-nucleus hypothesis has implications that can be in principle tested experimentally. For this purpose, the same compound nucleus has to be formed via different entrance channels and one should verify if the cross sections for the subsequent emission of various types of particles are indeed identical. However, it is not possible to measure directly the time of emission of particles from a nuclear reaction to select experimentally the reaction mechanism. All what we can measure is the energy spectra of the particles of different types as a function of emission angle. The unambiguous discrimination of the different processes from the measured spectra is not obvious, since particles originating from compound, direct or pre-equilibrium processes may populate the same energy and angular ranges.

Let us stress that the compound-nucleus states are not single-particle states, neither collective nuclear states (like rotations or vibrations) where all the nucleons move in a coordinated motion. Compound-nucleus states are extremely complex quasi-bound states, whose description involves the ensemble of the nucleons. In fact, compound-nuclear states and reactions are a relevant subject of study for the Random Matrix Theory, which is a generic theory of quantum chaotic systems [Wei09, Mit10].

1.2. Statistical model of compound-nuclear reactions

It is useful to divide compound-nuclear reactions according to whether the states in the compound nucleus are resolved. This depends partly on the target nucleus and the incident energy, and partly on the energy resolution ΔE of the incident beam.

At low energies where the width of the resonances Γ is much smaller than their average spacing D ($\Gamma << D$), the reaction may go through a single state in the compound nucleus to a single state in the final nucleus. This domain corresponds to the resolved resonance region, which was described at the beginning of this section and lead to the compound-nucleus concept [Wei09]. The ‘phenomenological’ R-matrix method is usually used to parameterise the cross sections in this region [Des10].

When the incident energy increases, the width Γ of the resonances increases and the nuclear states start to overlap. At some point we reach a situation in which $\Gamma >> D$. If the energy

resolution $\Delta E < \Gamma$, the cross sections show very complicated fluctuations of the same magnitude as the average cross section [Mit10] and Bohr hypothesis does not hold.

The situation of interest in the present work is when $\Gamma >> D$ and $\Delta E >> \Gamma$. That is, the energy resolution of the incident beam is broad enough so that many levels of the compound nucleus are excited. In that situation, the corresponding scattering wave functions are assumed to have a random phase so that when phase averages are performed all interference terms will vanish [Hau52]. From this assumption it follows that it is then possible to divide the inelastic scattering process into two independent parts, one related to the formation of the compound nucleus and one to its decay by particle emission: the validity of eq. (1) is restored. This is the basis of the statistical model, also known in literature as the Hauser-Feshbach formalism. The statistical model provides energy-averaged compound-nuclear cross sections in the region of non-resolved resonances.

The statistical model is based on the assumption of statistical equilibrium described in Chapter 1. Very often, one uses the term "channels" instead of "microstates". As mentioned in Chapter 1, the probability of decay to a particular channel is 1/*N*, where *N* is the total number of open channels. If a centrifugal, Coulomb or other type of potential barrier is present, the probability of the population of that channel is simply reduced by the transmission coefficient. According to the Hauser-Feshbach formalism, the average cross section per unit energy in the outgoing channel for reactions proceeding to an energy region in the final nucleus described by a level density is given by:

$$\frac{d\sigma_{\alpha\chi}(E_a)}{dE_\chi} = \pi\lambda\!\!\!^{-2}_{\alpha} \sum_{J\pi} \omega_\alpha^J \sum_{lsl's'I'} \frac{T^J_{\alpha ls} T^J_{\chi l's'} \rho_{I'}(U') W_{\alpha\chi}(J)}{\sum_{\chi'' l'' s''} T^J_{\chi'' l'' s''} + \sum_{\chi'' l'' s'' I''} \int T^J_{\chi'' l'' s''}(E_{\chi''}) \rho_{I''}(U'') dE_{\chi''}} \qquad (2)$$

Here E_a is the kinetic energy of the projectile, and $\lambda\!\!\!^{-}_{\alpha}$ is the reduced wavelength associated to the incident channel. The spin of the incident (outgoing) particle is *i* (*i'*), the target (residual nucleus) spin is *I* (*I'*), the spin for the entrance (exit) channel is $\vec{s} = \vec{i} + \vec{I}$ ($\vec{s}' = \vec{i}' + \vec{I}'$) and *l* (*l'*) is the orbital angular momentum in the incident (outgoing) channel. The channel spin combines with the orbital angular momentum to give the compound-nucleus angular momentum *J*. π is the parity of the compound nucleus. The statistical-weight factor ω_α^J is $(2J+1)/[(2i+1)\times(2I+1)]$ and gives the probability that the different spins and orbital angular momenta combine to give a particular *J*. The transmission coefficients for the entrance and exit channels are written as $T^J_{\alpha ls}$ and $T^J_{\chi l's'}$, respectively, and $\rho_{I'}(U')$ denotes the density of levels of spin *I'* and excitation energy *U'* of the residual nucleus. All energetically possible open or final channels χ'' have to be taken into account, thus the denominator includes contributions from decays to discrete levels in the residual nuclei (given by the first sum in the denominator) as well as contributions from decays to regions described by a level density in the residual nuclei (given by the second sum in the denominator, which involves an energy integral of transmission coefficients and level densities in the residual nuclei). The quantity $W_{\alpha\chi}$ corresponds to the width fluctuation correction.

Equation (2) is not yet the quantity of interest. Indeed, to get the total cross section we have to integrate expression (2) over all energies $E\chi$ of the final-state channels, which for fission corresponds to the energies of the transition states built on top of the fission barriers and for neutron emission to the energies of the states of the residual nucleus formed after neutron emission. For radiative capture, we usually need only the integral over the energy spectrum of primary gamma rays emitted from the compound nucleus. The Hauser-Feshbach formalism has been used in Article IV to calculate fission, neutron-emission and gamma-decay probabilities.

The width fluctuation correction $W_{\alpha\chi}$ takes into account the correlation between incident and outgoing waves in the elastic channel because of quantum-mechanical interference. It was not introduced by Hauser and Feshbach [Hau52] but by Vager [Vag71] about 20 years later. The width fluctuation correction has the effect of enhancing the elastic scattering cross section and, through the requirement of flux conservation, of decreasing the cross sections in the other non-elastic channels. This depletion rarely exceeds 10–20%, even at relatively low incident energies (below approximately 2 MeV). As the excitation energy of the compound nucleus increases and many reaction channels become available, the effect of the width fluctuations becomes quickly negligible for the nonelastic channels [Hod87]. If we neglect the width fluctuation correction, for each total spin and parity J^{π}, expression (2) factors into a product of two terms, one of which contains the transmission coefficients for the entrance channel. The other factor describes the probability of decay into the exit channel; i.e., it is the sum over exit channel transmission coefficients divided by the denominator representing the decay into all energetically available channels. Therefore, we find again the factorisation of the reaction cross section into the product of the formation cross section and the decay probability inherent to the compound-nucleus independence hypothesis.

Despite the fact that the theory of compound nuclear reactions was developed long ago, the existing models ignore many detailed features of nuclear structure and the reaction is treated in some average sense. As discussed in [Car14], there are still many challenges to make the existing theories valid in a more general case. Open questions are how to treat reactions that are between the two limiting conditions $\Gamma << D$ and $\Gamma >> D$, and how to improve and test the models used to consider the correlations between the different reaction channels. In addition, the existing pre-equilibrium models do not yet include all the necessary physics. Another considerable challenge for the theory of compound nuclear reactions is how to treat surrogate reactions where a direct-reaction process is used to initiate the formation of a compound nucleus. The latter difficulty will be discussed below.

1.2.1. The Weisskopf-Ewing limit

Neglecting width fluctuations and integrating over all final-state energies, eq. (2) yields for a neutron-induced reaction to:

$$\sigma_{n\chi}(E_n) = \sigma_n^{CN,tot}(E_n)\sum_{J\pi} F_n^{CN}(E_n, J^{\pi})G_{\chi}(E^*, J^{\pi}) \qquad (3)$$

where $\sigma_n^{CN,tot}(E_n)$ is the total cross section for the formation of a compound nucleus after the absorption of a neutron of incident energy E_n, which is directly related to the transmission coefficients for the entrance channel $T_{\alpha ls}^{J}$. F_n^{CN} is the probability to populate a compound state J^π after interaction with a neutron and corresponds to $F_n^{CN}(E_n, J^\pi) = \frac{\sigma_n^{CN}(E_n, J^\pi)}{\sigma_n^{CN,tot}(E_n)}$. G_χ is the probability or the branching ratio for the decay of the compound state into the exit channel χ. The compound-nucleus excitation energy E^* and the neutron energy E_n are related via:

$$E^* = \frac{A-1}{A} E_n + S_n \tag{4}$$

where A-1 is the mass of the target nucleus and S_n is the neutron separation energy of the compound nucleus A. We define the probability that a compound nucleus with E^* formed after neutron absorption decays through channel χ as:

$$P_{n,\chi}(E^*) = \sum_{J\pi} F_n^{CN}(E^*, J^\pi) G_\chi(E^*, J^\pi) \tag{5}$$

Then, eq. (3) becomes:

$$\sigma_{n\chi}(E_n) = \sigma_n^{CN,tot}(E_n) P_{n,\chi}(E^*) \tag{6}$$

The total compound-nucleus formation cross section $\sigma_n^{CN,tot}$ and the population probability F_n^{CN} can be calculated with optical potentials with an uncertainty of less than 10% [Esc12]. However, the theoretical predictions for the branching ratios G_χ are often quite uncertain because the competition between all possible decay channels has to be modelled. This requires accurate knowledge of spins and parities of excited nuclear states, γ-branching ratios for these states, nuclear level densities, and transmission coefficients for particles, photons, and fission. This information is available to some extent for nuclei located close to the stability valley where experimental data exist. Outside this domain, one has to rely on systematics or on extrapolations, which typically leads to significantly increased uncertainties in the calculated cross sections.

In the continuous level-density region, the functions $\rho_{I'}$ and $\rho_{I''}$ which appear in the numerator and the denominator of eq. (2) can be written as [Boh98]:

$$\rho(E^*, J) \approx \frac{\rho_{\text{int}}(E^*)}{\sqrt{8\pi}\sigma_K} \sum_{K=-J}^{J} \exp\left[-\frac{\hbar^2}{2T\Im_{\parallel}} K^2 - \frac{\hbar^2}{2T\Im_{\perp}}\left(J(J+1) - K^2\right)\right] \tag{7}$$

Here $\rho_{int}(E^*)$ is the continuum intrinsic level density and the other terms account for the increase of the level density caused by collective effects. The different contributions to the level density will be further discussed in Chapter 3. In eq. (7), T is the temperature given by the inverse of the logarithmic derivative of ρ_{int}, K is the projection of J on the nucleus symmetry axis and σ_K is the so-called spin cut-off, which is closely related to the nucleus

momenta of inertia $\Im_{\parallel}$ parallel and $\Im_{\perp}$ perpendicular to the nuclear symmetry axis. For the actinides at excitation energies close to S_n, σ_K takes values of about 6-7. When the excitation energy E^* is large compared to the rotational energy $\hbar^2K^2/2\,\Im_{\parallel}$ and K is smaller than σ_K, the level densities are proportional to $(2J+1)\rho_{int}(E^*)$, this situation is called the Weisskopf-Ewing limit.

In the Weisskopf-Ewing limit the branching ratios $G_\chi\,(E^*,J^\pi)$ become independent of J^π, i.e. $G_\chi\,(E^*,J^\pi) \approx G_\chi(E^*)$. Then $G_\chi(E^*)$ can be taken out of the summation sign in eq. (5) and, since $\sum_{J\pi} F_n^{CN}(E_n,J^\pi) = 1$, $P_{n,\chi}(E^*) = G_\chi(E^*)$, eq. (6) becomes:

$$\sigma_{n\chi}(E_n) = \sigma_n^{CN,tot}(E_n)\cdot G_\chi(E^*) \tag{8}$$

It is important to stress that the Weisskopf-Ewing limit is only valid when the compound nucleus decays to continuum states of the final nucleus. This limit is expected to break down at low energies when the nucleus decays predominantly to well-defined, individual final states. In addition, as shown in Figs. 7 and 8 of [Esc06], the Weisskopf-Ewing limit breaks down even at high excitation energy if the spin considered is significantly larger than the spin cut-off parameter.

2. The surrogate-reaction method

We have seen before that statistical-model calculations are subject to significant uncertainties when used for predicting neutron-induced cross sections of short-lived nuclei where no experimental information is available. The uncertainties concern mainly the branching ratios G_χ. The objective of the surrogate-reaction method is to determine or constrain G_χ using an alternative or surrogate reaction that leads to the same compound nucleus as the neutron-induced reaction of interest. This method is schematically represented in Fig. 1. The left part of Fig. 1 illustrates a neutron-induced reaction on target A-1, which leads to the nucleus A^* at an excitation energy E^*. The nucleus A^* can decay via different exit channels: fission, gamma-decay, neutron emission, etc… On the right part of Fig. 1, the same compound nucleus A^* is produced by a surrogate reaction. In Fig. 1, the surrogate reaction is a transfer reaction between a projectile y (a light nucleus) and a target X, leading to the heavy recoil nucleus A^* and an ejectile w. In most applications of the surrogate method, the surrogate reaction is used to measure the decay probability $P_\chi^{surro}(E^*)$ and the desired neutron-induced reaction cross section is obtained by applying the equation:

$$\sigma_{n\chi}(E_n) = \sigma_n^{CN,tot}(E_n)\cdot P_\chi^{surro}(E^*) \tag{9}$$

where $\sigma_n^{CN,tot}(E_n)$ is obtained from an optical model calculation.

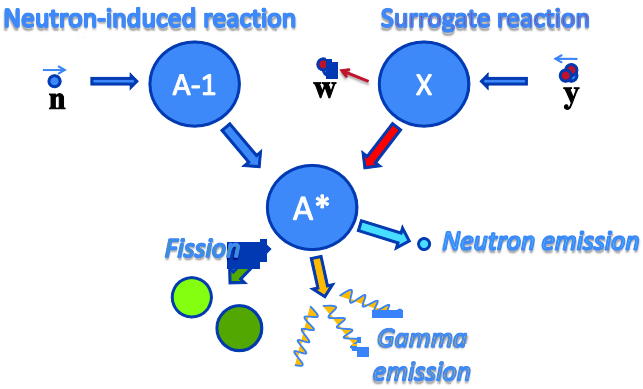

Figure 1: Schematic representation of the surrogate-reaction method. The surrogate reaction is here a transfer reaction $X(y,w)A^*$. Three possible exit channels (fission, gamma emission and neutron emission) are represented.

Transfer channel	Neutron-induced reaction	Equivalent neutron energies [MeV]	Half-life
^{243}Am(^{3}He,d) ^{244}Cm	^{243}Cm(n,f)	0-3	^{243}Cm($T_{1/2}$=29.1 y)
^{243}Am(^{3}He,t) ^{243}Cm	^{242}Cm(n,f)	0-10	^{242}Cm($T_{1/2}$=162.8 d)
^{243}Am(^{3}He,α) ^{242}Am	^{241}Am(n,f)	0-10	^{241}Am($T_{1/2}$=432.2 y)

Table 1: Transfer channels investigated in the reaction ^{3}He+^{243}Am at 24MeV and the corresponding neutron-induced fission reactions. This reaction was studied in Articles I and IV.

The greatest benefit of the surrogate method is that in some cases one can find a surrogate reaction where the target X is stable or less radioactive than the target A-1. But this is not the only advantage. In the surrogate reaction there are two bodies in the outgoing reaction channel and the excitation energy of the heavy nucleus E^* follows a broad probability distribution extending from 0 to several tens of MeV. In addition, several transfer channels are simultaneously populated. Therefore, one can determine decay probabilities over a wide range of E^* for various nuclei from a single projectile-target combination and a single beam energy. As an example, we have employed few-nucleon transfer reactions using a ^{3}He projectile at 24 MeV on a ^{243}Am target as surrogate reactions to infer neutron-induced fission cross sections on various Cm and Am isotopes. This work is described in Articles I and IV. Table 1 lists the transfer channels considered in the reaction ^{3}He + ^{243}Am, and the corresponding neutron-induced reactions. The populated neutron-equivalent energies and the half-lives of the targets associated to the neutron-induced reactions are shown in the two last columns. Note that these half-lives are much shorter than the half-live of 7370 y of the ^{243}Am target used in the surrogate experiment.

2.1. Validity of the surrogate-reaction method

The first condition for the surrogate method to be valid is that the decaying nucleus has to be a compound nucleus in both, the desired neutron-induced and surrogate reactions. Only under this condition it is possible to factorise the cross section into the product of a compound-

nucleus formation cross section and a decay probability. From the theoretical side, one has to ensure that the direct and pre-equilibrium contributions are correctly calculated and subtracted from the total neutron-induced reaction cross section. For neutron-induced reactions, the optical model can be used to calculate the direct and compound nucleus contributions rather accurately, but the situation is more complicated concerning pre-equilibrium emission where the appropriate theoretical tools are still under development [Car14]. From the experimental side, one should in principle ensure that only compound-nuclear events have been selected. As it will be shown below, with present experimental techniques one detects the ejectiles and uses mass and charge conservation to identify the corresponding decaying nucleus A^*. It is expected that direct and pre-equilibrium reactions lead to ejectiles with higher energies and smaller emission angles than ejectiles originating from compound reactions. However, in practice it is not possible to unambiguously separate the different mechanisms because the ejectile distributions populated by the compound nucleus mechanism are rather large and overlap with the distributions associated to direct and pre-equilibrium reactions.

The decay probability $P_{\chi}^{surro}(E^*)$ is given by:

$$P_{\chi}^{surro}(E^*) = \sum_{J\pi} F_{surro}^{CN}(E^*, J^{\pi}) G_{\chi}(E^*, J^{\pi}) \tag{10}$$

Note that the branching ratios $G_{\chi}(E^*, J^{\pi})$ are the same as in eq. (5), reflecting that the decay of the compound nucleus is independent of the way it was formed. By comparing eqs. (5) and (10), it follows that the surrogate method as given by eq. (9) is strictly applicable only in two cases:

-If the Weisskopf-Ewing limit is valid, and therefore $G_{\chi}(E^*, J^{\pi}) = G_{\chi}(E^*)$ and $P_{\chi}^{surro}(E^*) = G_{\chi}(E^*) = P_{n,\chi}(E^*)$

or

-If the J^{π} distributions populated in both reactions are equal $F_{n}^{CN}(E^*, J^{\pi}) = F_{surro}^{CN}(E^*, J^{\pi})$

There is no reason to expect that the spin-parity distributions F populated in the neutron-induced and surrogate reactions are the same, and the Weisskopf-Ewing limit is only valid at high excitation energies. In fact, at low excitation energy the branching ratios G_{χ} may strongly depend on J and π. Therefore, the spin-parity mismatch between the neutron-induced and surrogate reactions can lead to significant differences between the cross sections obtained with the two methods.

While it is possible to calculate the angular-momentum and parity distributions populated in neutron-induced reactions using optical potentials, this is by far not the case when the compound nucleus is formed via a transfer reaction (see [Esc12]). Transfer reactions populate single-particle states, such as single neutron states in the (d,p) reactions, single proton states in the (^{3}He,d) reaction and single neutron-hole states in the (^{3}He,^{4}He) reactions. This quite

simple picture is valid at low excitation energies, and has been extensively used in the past in nuclear-structure studies. However, in the excitation-energy region of interest in this work ($E^* > S_n$), these single-particle states are strongly mixed with the highly dense and complex compound-nuclear states, whose decay is described by the statistical model. In other words, the strength of the particular single-particle states populated by the direct reaction "spreads out" over a large number of compound levels [Lew75]. One can imagine the surrogate reactions as a two-step process where the single particle state initially populated by the transfer reaction readily mixes with the continuum of compound levels that have the same quantum numbers (J^π), leading eventually to the formation of a compound nucleus. The main difficulty is to theoretically estimate how the initial single-particle states are fragmented into the complex many-body states in the continuum and usually different approximations are used [And70, Tho06], see also Article IV.

Since for most surrogate reactions it is not yet possible to predict the populated spin/parity distribution, the validity of the surrogate method has to be verified a posteriori, by comparing the obtained results with well known neutron-induced data. To achieve reliable conclusions out of this comparison it is very important to identify and, if possible, correct for any systematic error in the measurement of $P_\chi^{surro}(E^*)$.

3. Surrogate-reaction studies performed by the CENBG collaboration

The CENBG, in collaboration with other laboratories in France and abroad, performs experiments to investigate the surrogate-reaction method since approximately the year 2000. The surrogate reactions studied and the associated references are listed in Table 2. As it can be seen, we have measured fission and gamma-decay probabilities. Therefore, in the following sections we will consider only aspects related to the experimental determination of the probabilities of these two decay modes.

4. Measurement of the decay probability

In our surrogate experiments, the decay probability is obtained with the following expression:

$$P_\chi^{surro}(E^*) = \frac{N_{ejec-\chi}^{coin}(E^*)}{N_{ejec}^{singles}(E^*)\varepsilon_\chi(E^*)} \tag{11}$$

Here $N_{ejec}^{singles}$ is the so-called "singles spectrum", i.e. the total number of detected ejectiles *w*, $N_{ejec-\chi}^{coin}$ is the "coincidence spectrum" corresponding to the number of ejectiles detected in coincidence with the observable that identifies the decay mode, e.g. a fission fragment or a gamma ray, and ε_χ is the associated efficiency. In the absence of parasitic transfer reactions with the same ejectile, the quantity $N_{ejec-\chi}^{coin}(E^*)/\varepsilon_\chi$ gives the fraction of compound nuclei A^* that have decayed via the channel χ (by e.g. fission or gamma emission) with respect to the number of formed compound nuclei $N_{ejec}^{singles}(E^*)$.

Surrogate reactions	Measured quantity	References
^{232}Th(^{3}He,p)^{234}Pa ^{232}Th(^{3}He,d)^{233}Pa ^{232}Th(^{3}He,t)^{232}Pa ^{232}Th(^{3}He,^{4}He)^{231}Th	Fission probability	[Pet04]
^{232}Th(^{3}He,p)^{234}Pa	Gamma-decay probability	[Boy06]
^{243}Am(^{3}He,d)^{244}Cm ^{243}Am(^{3}He,t)^{243}Cm ^{243}Am(^{3}He,^{4}He)^{242}Am	Fission probability	PhD Thesis of G. Kessedjian (2008) (Article I) (Article IV)
^{174}Yb(^{3}He,p)^{176}Lu ^{174}Yb(^{3}He,^{4}He) ^{173}Yb	Gamma-decay probability	PhD Thesis of G. Boutoux (2011) (Article II) (Article III)
^{238}U(d,p)^{239}U ^{238}U(^{3}He,d)^{239}Np ^{238}U(^{3}He,t)^{238}Np ^{238}U(^{3}He,^{4}He)^{237}U	Fission and gamma-decay probabilities	PhD thesis of Q. Ducasse (2015) [Duc15]

Table 2 : Surrogate reactions studied by the CENBG collaboration and related references.

For determining the gamma-decay probability we need to determine the number of compound nuclei that decay through a gamma cascade $N_{ejec-gamma}^{coin}$. Therefore, what we actually need to measure is the number of detected cascades and not the number of detected gammas. In our experiments, the solid angle of the gamma-detector array is relatively small so that, in most cases, we detect only one gamma ray of the cascade. For the few cases where more than one gamma detector is hit in one event, we randomly select one detector signal amplitude in the offline data analysis. In that way we ensure that each detected gamma ray corresponds to a gamma cascade.

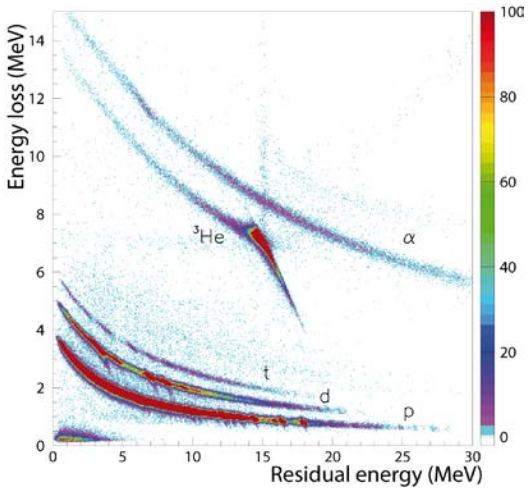

Figure 2: Energy loss versus residual energy in one of the Si telescopes for the ^{3}He + ^{243}Am reaction at 24 MeV. The ejectiles associated to the different *Z* lines are indicated.

Eq. (11) defines the experimental set-up needed. Typically, a ΔE/E particle telescope is used to identify the ejectiles and determine their kinetic energies and angles. An identification plot is presented in Fig. 2. The telescope is surrounded by different detectors for the decay particles. The time elapsed between the detection of an ejectile and the detection of a decay particle is recorded in order to identify the coincident events. Schematic figures of our experimental setups can be seen in Article I (or Article IV) and in Article II. As an example, Fig. 3 shows the setup we used at the Oslo cyclotron in June 2012. The ejectiles were detected at backward angles (126 to 140 degrees) with the SiRi multi-strip silicon telescope [Gut11-2]. The fission detector was located at forward angles and consisted of 4 PPACs covering a solid angle of 41% out of 4π [Tor14]. The reaction chamber housing SiRi, the PPACs and the target was surrounded by the CACTUS array with 28 high-efficiency NaI detectors. CACTUS was used to detect gamma rays with energies ranging from a few keV to about 10 MeV in coincidence with the ejectiles. With this equipment we could measure fission and gamma-decay probabilities of different compound nuclei formed by transfer reactions between deuteron and ^{3}He projectiles, and a ^{238}U target.

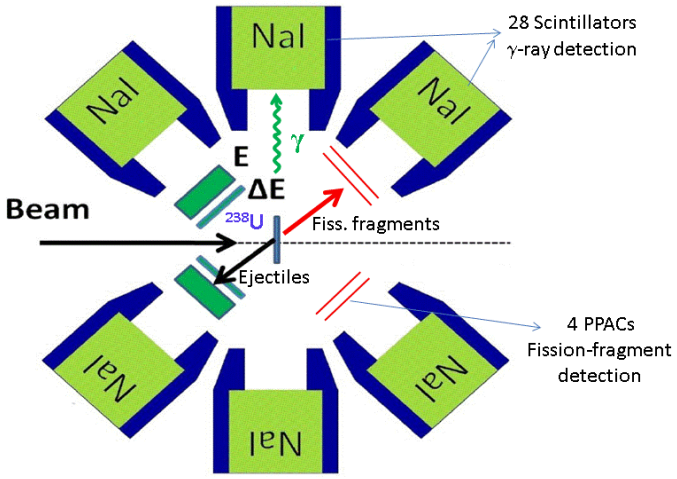

Figure 3: Schematic view of the set-up used at the Oslo cyclotron for decay-probability measurements.

4.1. Determination of the excitation energy of the compound nucleus

In a recent work [Rod14], where fission was induced via multinucleon transfer between ^{12}C and ^{238}U, a non negligible probability of exciting the carbon-like ejectiles was observed, that questioned the commonly used assumption that the excitation energy available in the transfer reaction is found only in the heavy reaction partner. As shown in Table 2, all the reactions studied by the CENBG collaboration involve protons, deuterons, tritons or α particles as ejectiles. Protons, deuterons and tritons have no bound excited states. The first excited state of ^{4}He is located at 20.2 MeV but in our experiments the maximum total available excitation energy considered is essentially below 20 MeV. Therefore, all the *detected* ejectiles are in their ground state and all the excitation energy available in the reaction can safely be attributed to the fissioning nucleus *A*. The excitation energy E^* can then be unambiguously determined from the measured kinetic energy E_w and emission angle θ of the ejectile, by applying energy and momentum conservation laws:

$$E^* = \frac{M_A Q - E_y (M_y - M_A) - E_w (M_A + M_w) + 2\sqrt{M_y M_w E_y E_w}\cos\theta}{M_A} \quad (12)$$

where the different M_i represent the masses of the nuclei involved in the reaction, Q is the Q-value of the transfer reaction and E_y is the beam energy.

In our measurements, E^* is determined with an uncertainty of typically 100 keV, which is due to the uncertainties on the different quantities involved in eq. (12). This uncertainty is well adapted for the measurement of decay probabilities with a significant E^* dependence, which is the case at the fission threshold for the fission probability, and close to S_n for the gamma-decay probability. Our measurements not only require that E^* is measured with good precision but also that it is determined with high accuracy. If E^* is incorrectly determined, it can lead for example to an energy shift of the fission threshold and to serious misinterpretations when the data are compared with neutron-induced data. Obviously, any lack of accuracy in the quantities involved in eq. (12) will be propagated to E^*. In particular, the beam energy needs to be well defined. This was an issue in our experiment at the Oslo cyclotron. We think there was a shift as large as 1 MeV in the ^{3}He beam energy delivered by the Oslo cyclotron, possibly due to a wrong setting of the cyclotron frequency. Using the expected beam-energy value of 24 MeV in the determination of the excitation energy, the fission thresholds were shifted by several MeV with respect to the fission thresholds measured with neutron beams. In addition, our fission threshold for the ^{238}U(^{3}He,t) reaction was significantly shifted with respect to the fission threshold measured by Gavron et al. [Gav76] using the same reaction with very similar experimental conditions: 25 MeV beam energy and telescope centred at 120 degrees. After testing many different hypotheses, we came to the conclusion that the actual beam energy was 23 MeV [Duc15]. Unfortunately, it has not been possible to find out what was the actual cyclotron frequency during the experiment and there is no way to confirm that the actual beam energy was 23 MeV. Problems with the beam-energy definition have also been encountered at the Texas Cyclotron [Meo13], where surrogate-reaction studies are conducted by the Livermore group.

The measurement of the ejectile kinetic-energy is also crucial for the determination of E^* and efforts should be made to determine it as accurately as possible. The kinetic energies relevant in our surrogate experiments range from few to several tens of MeV. Thus, the kinetic energies can be much higher than the kinetic energies of the alpha particles originating from a standard calibration source. Besides, it is well known that the response of Si detectors to hydrogen isotopes differs from the response to alphas of the same kinetic energy [Kno00]. Therefore, it is not appropriate to calibrate the particle detectors only with a standard alpha source. In our experiments the telescopes are calibrated with known energy lines from chosen reactions on a lead target. More precisely, we typically use a ^{208}Pb target and a ^{3}He beam to populate the first excited states of ^{209}Bi and ^{207}Pb via the transfer reactions ^{208}Pb(^{3}He,d) and ^{208}Pb(^{3}He,^{4}He), respectively. Since the E^* of the first excited states of these nuclei are known with high accuracy, we can in this way have a source of different ejectiles with very well defined kinetic energies in the range of interest for the surrogate measurement. The calibration procedure is described in Article IV.

4.2. Determination of coincidence events

Due to the high kinetic energies of the fission fragments (about 1 A MeV), their unambiguous detection is rather straightforward and there is generally no major problem in the determination of $N^{coin}_{ejec-fission}$, see Article IV. The situation can be more complicated for determining $N^{coin}_{ejec-gamma}$ when one uses scintillator detectors. Neutrons emitted by the compound nucleus A^* can interact with the scintillator material and lead to signals that have to be distinguished from the signals induced by gamma rays. When one uses C_6D_6 detectors, as was done in Article II, neutrons can be disentangled from gamma rays via pulse-shape discrimination. For NaI detectors, the neutron/gamma discrimination can be done by using the time-of-flight differences between neutrons and gammas. This method was used in the analysis of the data taken at the Oslo cyclotron [Duc15].

Scintillators have a relatively low energy resolution and one loses the information on the gamma energy E_γ. Therefore, it is not possible to tell whether the gamma ray comes from compound nucleus A^* or from the residual nucleus A-1 produced after neutron emission. However, the gamma rays emitted by nucleus A-1 have a maximum energy $E_\gamma = E^*- S_n$ and can be removed from the $N^{coin}_{ejec-\chi}$ spectrum by applying the gamma-energy threshold $E_\gamma > E^*-S_n$ in the two dimensional spectrum that represents the excitation energy versus the energy of the gamma rays measured in coincidence with the telescope. This is shown in Fig. 4 for the ^{174}Yb(^{3}He,p) reaction studied in Article II. As discussed in Article II, in that experiment we used two types of gamma detectors for determining $P^{surro}_{gamma}(E^*)$, C_6D_6 liquid scintillators and high-purity Ge detectors. With the Ge detectors it is possible to select only the gamma rays coming from nucleus A, however this strongly limits the statistics. We found that the gamma-decay probabilities obtained with the two types of detector were in good agreement, demonstrating that neutrons and gamma rays originating from nucleus A-1 were properly removed when using C_6D_6 detectors.

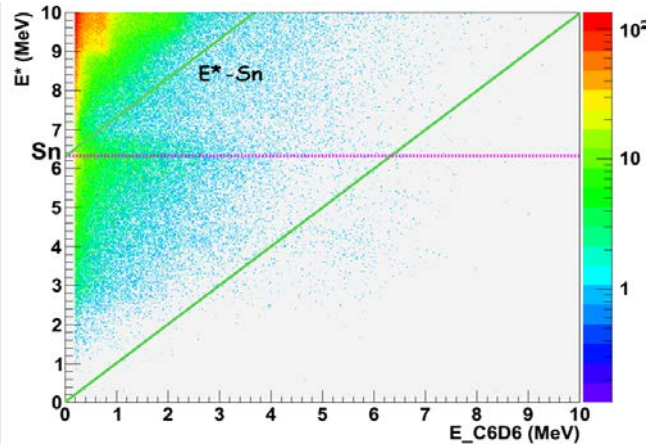

Figure 5: Excitation energy of the compound nucleus as a function of the detected gamma-ray energy for the ^{174}Yb(^{3}He,p)^{176}Lu reaction studied in Article II. The horizontal dotted line represents the neutron separation energy of ^{176}Lu*, the upper 45º diagonal on the left corner corresponds to the events that satisfy E_γ=E^*-S_n and the lower diagonal to E_γ=E^*.

A more complicated situation arises if the compound nucleus undergoes fission. In this case, it is also necessary to remove the prompt gamma rays emitted by the fission fragments (see Chapter 3). This can be done by measuring the fission-fragment gamma rays in coincidence with the fission detector:

$$N^{coin}_{ejec-gamma} = N^{tot}_{gamma} - \frac{N^{fiss}_{gamma}}{\varepsilon_{fission}} \tag{13}$$

Here, N^{tot}_{gamma} is the total number of gamma cascades detected in coincidence with the ejectiles and N^{fiss}_{gamma} is the total number of gamma cascades detected in coincidence with the ejectiles and with the fission detector. The uncertainty in $N^{coin}_{ejec-gamma}$ is directly related to the fission efficiency $\varepsilon_{fission}$ and its uncertainty. It can be shown [Duc15] that the relative uncertainty on $N^{coin}_{ejec-gamma}$, without considering the correlation between the different quantities, is:

$$\frac{Var(N^{coin}_{ejec-gamma})}{\left(N^{coin}_{ejec-gamma}\right)^2} = \frac{Var(N^{tot}_{gamma})}{\left(N^{coin}_{ejec-gamma}\right)^2} + \frac{Var(N^{fiss}_{gamma})}{\left(\varepsilon_{fission} N^{coin}_{ejec-gamma}\right)^2} + \delta^2 \frac{Var(\varepsilon_{fission})}{\left(\varepsilon_{fission}\right)^2} \tag{14}$$

where *Var* is the variance, and

$$\delta \approx \frac{P_{fission} M^{\gamma}_{fission}}{P_{gamma} M^{\gamma}_{gamma}} \tag{15}$$

where $M^{\gamma}_{fission}$ and M^{γ}_{gamma} are the gamma-ray multiplicities for fission and gamma-decay, respectively. The gamma multiplicity of a fission event is about two times larger than for a gamma-decay event. We thus see from eq. (14) that the relative uncertainty increases when $\varepsilon_{fission}$ decreases and that the uncertainty in $\varepsilon_{fission}$, included in the third term of eq. (14), becomes preponderant when fission is the dominating decay mode and δ is large.

4.3. Fission detection efficiency

As described in Article IV, the efficiency for detecting a fission event $\varepsilon_{fission}$ is determined by the solid angle of the fission detector and by the angular anisotropy of the fission fragments. The latter depends on the angular-momentum distribution of the fissioning nucleus and on its recoil energy, which leads to a kinematical focusing of the fission fragments in the direction of the fissioning nucleus. The detector solid angle can be determined experimentally with a ^{252}Cf source of known activity and the fission-fragment angular anisotropy by using a position-sensitive fission detector. The influence of the fission-fragment angular anisotropy on the final fission efficiency decreases considerably with increasing solid angle. In the measurement described in Articles I and IV, the fission efficiency was (45.2 ± 1.5)%. Unfortunately, the PPACS used in the Oslo experiment were not position sensitive and we could not measure the fission-fragment angular anisotropy. For the deuteron-induced reaction ^{238}U(d,p) we could find experimental information on the angular anisotropy in [Cra70].

However, we do not have this information for the ^{3}He-induced reactions, which leads to a significant relative uncertainty in $\varepsilon_{fission}$ of more than 10%.

4.4. Efficiency for detecting a gamma cascade

For measurements of the gamma-decay probability, rather than the efficiency for detecting a gamma ray of particular E_γ, one needs to determine the efficiency for detecting a decay that proceeds through the emission of a gamma cascade. In other words, one needs to determine the gamma-cascade detection efficiency.

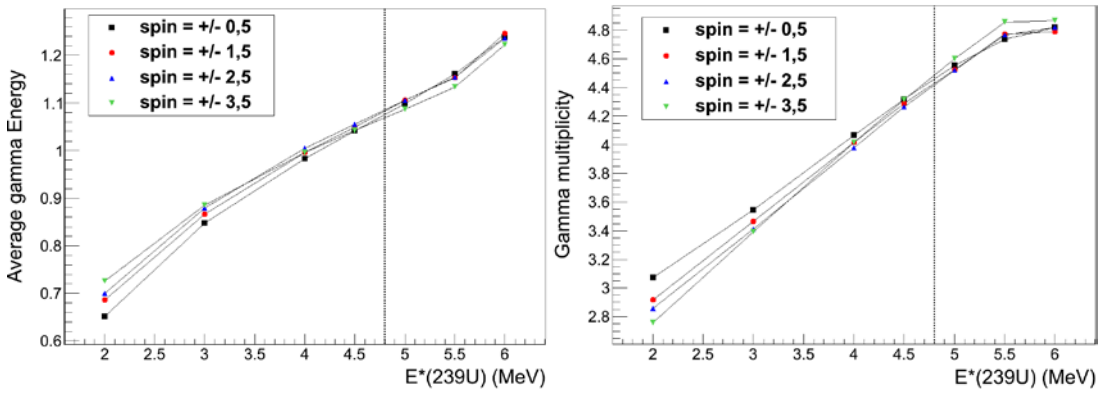

Figure 6: Average gamma-ray energy and multiplicity as a function of excitation energy calculated for the gamma decay of ^{239}U with the EVITA code [Mor13]. The legends indicate the spin and parity of the initial state of ^{239}U. The vertical dashed line represents the neutron separation energy S_n of ^{239}U.

The efficiency for detecting a gamma cascade depends on the gamma multiplicity of the cascade and on the energies of the gammas of the cascade. The multiplicity and the energies of the gammas of a cascade depend on E^*. Moreover, in the quasi-continuum and the continuum regions, the cascade paths can be very different from one event to the other, even if E^* is the same for all the events. Therefore, it is rather difficult to determine the gamma-cascade detection efficiency at $E^* \geq S_n$. Note that this is not a specific problem of surrogate-reaction experiments, but it is also found in neutron-induced radiative-capture measurements. In these experiments the Pulse-Height Weighting-function Technique (PHWT) is used to determine the gamma-cascade detection efficiency. The principle of this technique is described in Article III and references therein. As discussed in Article III, the PHWT is quite complicated as it requires to determine the response functions of the detector array for many incident gamma-ray energies E_γ ranging from few hundred keV to about S_n + 1 MeV in steps of few hundred keV. In Article III, we presented an alternative method for determining the gamma-cascade detection efficiency in surrogate-reaction experiments, called the EXtrapolated-Efficiency Method, EXEM, which is much simpler than the PHWT.

In a surrogate reaction it is possible to populate excitation energies below the neutron separation energy. For neutron-rich nuclei that do not fission below S_n, the only possible mode of desexcitation is gamma decay and we have:

$$P_{gamma}^{surro}(E^*) = 1 = \frac{N_{ejec-gamma}^{coin}(E^*)}{N_{ejec}^{singles}(E^*)\varepsilon_{gamma}(E^*)} \qquad \text{for } E^* < S_n \tag{16}$$

From eq. (16) it follows:

$$\varepsilon_{gamma}(E^*) = \frac{N_{ejec-gamma}^{coin}(E^*)}{N_{ejec}^{singles}(E^*)} \qquad \text{for } E^* < S_n \tag{17}$$

Therefore, for excitation energies below S_n, the gamma-cascade detection efficiency $\varepsilon_{gamma}(E^*)$ can be directly obtained from the ratio between $N_{ejec-gamma}^{coin}(E^*)$ and $N_{ejec}^{singles}(E^*)$. For medium mass and actinide nuclei in the region of continuum level densities there is no reason to expect a drastic change in the characteristics of the gamma cascades, and thus of $\varepsilon_{gamma}(E^*)$, at S_n. This is indeed demonstrated by the calculation shown in Fig. 6, where the average gamma-ray energy and multiplicity obtained with the Monte-Carlo statistical code EVITA [Mor13] for the gamma decay of ^{239}U are represented. The calculation shows that for both quantities there is nearly no change in the slope at S_n. In Fig. 7, we show the measured ratio $N_{ejec-gamma}^{coin} / N_{ejec}^{singles}$ as a function of E^* for the ^{238}U(d,p) reaction. We can see that the efficiency increases with E^* below S_n. This is explained by the calculations of Fig. 6, which show that the average gamma-ray energy and multiplicity increase with E^*. The ratio $N_{ejec-gamma}^{coin} / N_{ejec}^{singles}$ drops at S_n because neutron emission becomes possible leading to a drastic decrease of $N_{ejec-gamma}^{coin}$. It is thus well justified to extrapolate the functional form of ε_{gamma} with E^* measured below S_n to E^* above S_n. This is the essential idea behind the EXEM. Fig. 6 shows that the multiplicity starts to saturate at about 5.5 MeV, which probably defines the limit of the maximum excitation energy to which the efficiency can be extrapolated. As shown in Article III, the validity of the EXEM was demonstrated by comparing its results with the ones obtained using the PWFT. The efficiency derived from the EXEM for the ^{238}U(d,p) reaction will be also compared to the efficiency obtained with the PHWT in [Duc15].

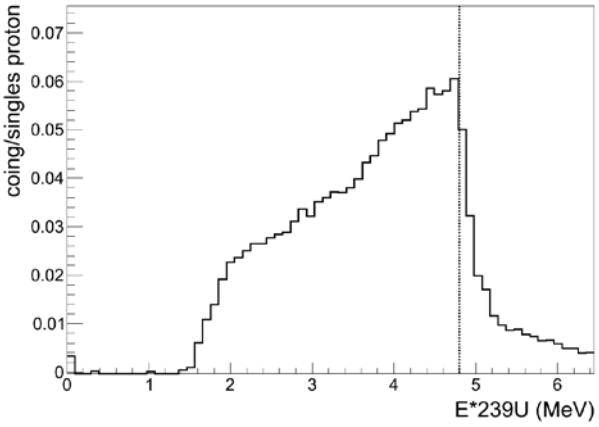

Figure 7: Measured ratio $N_{ejec-gamma}^{coin} / N_{ejec}^{singles}$ as a function of the excitation energy of ^{239}U for the ^{238}U(d,p). The vertical dashed line represents the neutron separation energy S_n of ^{239}U.

Both techniques, the EXEM and the PHWT, have drawbacks. The main limitation of the EXEM is that it is not clear up to which E^* it is possible to extrapolate the behaviour observed below S_n. For instance, we have observed that the efficiency of a NaI increases with the energy of the incident gamma ray up to about E_γ =1.3 MeV and decreases slightly above this energy. When the average gamma energy of the cascade reaches this value, it can lead to a change in the efficiency that invalidates the extrapolation. On the other hand, aside from the arduousness of the PHWT, a significant issue of this technique is that it requires the knowledge of the detected gamma spectrum below the electronic threshold down to E_γ =0 MeV. Both issues can be studied by simulating the cascade-detection efficiency of the detection array, but this requires the use of models to generate the gamma cascades.

4.5. Contaminants in singles and coincidence spectra

We see from eq. (11) that the determination of the decay probability is based on the detection of the ejectiles and not of the recoil nuclei A^*. If there are other reactions that lead to the same ejectiles, they will affect the ejectile spectra. There are different sources of background: reactions on the target backing and on target contaminants, breakup of the beam and/or the ejectiles and charged particles originating from fusion-evaporation reactions. In fission experiments, it is possible to solve the contaminant issue by using the surrogate ratio method [Ple05]. This method is discussed in section 5.

Spurious events due to reactions on the target backing can be in principle eliminated by subtracting from the total singles spectrum the singles spectrum measured separately with the carbon backing only. One of the major problems we have encountered in our measurements is the presence of contaminants in the target. Transfer reactions between the beam and the contaminant nuclei can then lead to a background in the $N_{ejec}^{singles}(E^*)$ spectrum that cannot be subtracted. Therefore, the chemical purity of the targets is extremely important in surrogate reaction experiments [Jur10]. While it is possible to produce targets of very high isotopic purity, it is almost impossible to completely avoid the presence of light contaminants in the target, in particular oxygen. Light target contaminants do not affect the fission-coincidence spectrum but they can pollute the gamma-coincidence spectrum if one uses scintillator detectors. The presence of light target contaminants leads to broad peaks in the $N_{ejec}^{singles}(E^*)$ spectrum, as shown in Fig. 8, which was taken from Article IV.

One way to cope with the problem of light-target contaminants is to place the particle telescopes at backward angles. In that way, due to reaction kinematics, the contaminant peaks are located at the highest compound-nucleus excitation energies leaving a broad range of excitation energy free from background, see Fig. 8. To determine $N_{ejec}^{singles}$ in an excitation-energy region where contaminant peaks are present we interpolate the singles spectrum below the contaminant peak, see Fig. 8. This introduces a significant uncertainty, as discussed in Article IV.

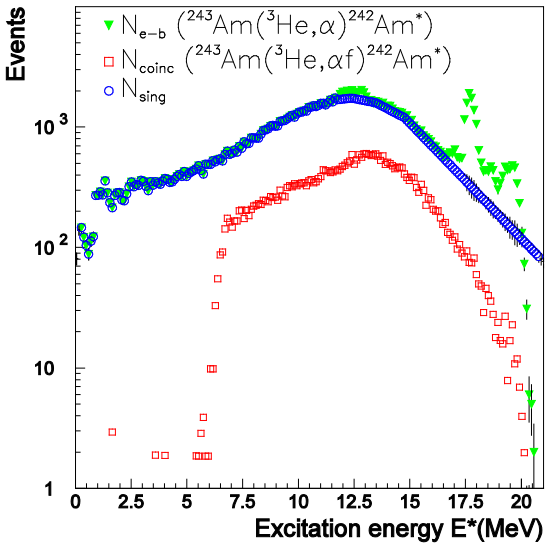

Figure 8: Number of detected ^{4}He (green triangles) ejectiles as a function of the excitation energy of ^{242}Am after subtraction of events coming from reactions on the target backing. The ^{4}He ejectiles stemming from reactions on target contaminants are present above 12 MeV. The blue circles represent the singles spectrum after interpolation and the red squares the fission coincidence spectrum for ^{242}Am. The data correspond to the ^{243}Am(^{3}He,^{4}He) reaction studied in Articles I and IV.

Deuterons, tritons and ^{3}He break up at excitation energies of 2.2, 6.2 and 5.5 MeV, respectively. In principle, the protons and the deuterons that result from the breakup may also pollute the corresponding singles spectra. However, in the work by Gavron et al. [Gav76] the fission probabilities of various nuclei formed by both (^{3}He,d) and (^{3}He,t) reactions were compared and found to be approximately equal, thus demonstrating that contamination due to ^{3}He or triton breakup can be disregarded. For these measurements, Gavron et al. used a beam energy of 25 MeV and a particle telescope placed at 120 degrees. Therefore, to avoid a possible background created by ^{3}He or triton breakup we have used in our measurements experimental conditions similar to Gavron et al. The breakup of the deuterons produced in the (^{3}He,d) reaction may pollute the singles spectrum of the (^{3}He,p) reaction. However, the ^{233}Pa(n,f) cross section obtained using the ^{232}Th(^{3}He,p) reaction in [Pet04] is in good agreement with the corresponding neutron-induced data, indicating that this transfer channel was not polluted by the deuteron breakup from the ^{232}Th(^{3}He,d) channel. The reason may be that the probability that the ejectiles acquire sufficient excitation energy to breakup is very low because of the huge difference between the level densities of the ejectile and compound nuclei, which tends to drive the excitation energy to the heavy compound nucleus. Finally, we stress that, while the breakup of the ^{3}He projectile is not an issue under our experimental conditions, this is certainly not the case for deuteron-induced reactions, as will be discussed below.

Other nuclear reactions like fusion evaporation are in principle also possible. Evaporated particles do not have specific energies but populate a broad energy distribution and may therefore contaminate a wide range of *E** in the singles spectrum. When the beam fuses with the heavy actinide target nucleus a heavy neutron-rich excited nucleus is formed, for which

the probability of evaporating light charged particles is rather low. In fact, the most probable reaction after the fusion of the beam with the target is fission, preceded by the emission of several neutrons. Fusion of the beam with light target contaminants is more problematic, because the resulting nuclei are neutron deficient and can evaporate charged particles. This problem will be further discussed in section 7.

5. Comments on the surrogate ratio method

The surrogate ratio method was developed by Plettner et al. [Ple05] and it has been widely used since then, mainly by the Livermore collaboration, see [Esc12] and refs. therein. This method is also based on the Weisskopf Ewing limit (eq. 9) and considers the ratio *R* of two neutron-induced cross sections leading to two different nuclei *A* and *B*:

$$R(E^*) = \frac{\sigma_{n,\chi}^{A}}{\sigma_{n,\chi}^{B}} \approx \frac{\sigma_{n}^{CN,A}(E^*)P_{\chi}^{surro,A}(E^*)}{\sigma_{n}^{CN,B}(E^*)P_{\chi}^{surro,B}(E^*)} \tag{18}$$

Combining eq. (11) and eq. (18) we get:

$$R(E^*) = \frac{\sigma_{n}^{CN,A}(E^*)N_{ejec-\chi}^{coin,A}(E^*)N_{ejec}^{sing,B}(E^*)\varepsilon_{\chi}^{B}(E^*)}{\sigma_{n}^{CN,B}(E^*)N_{ejec-\chi}^{coin,B}(E^*)N_{ejec}^{sing,A}(E^*)\varepsilon_{\chi}^{A}(E^*)} \tag{19}$$

If target nuclei *A*-1 and *B*-1 are close enough so that $\sigma_{n}^{CN,A}(E^*) \approx \sigma_{n}^{CN,B}(E^*)$ and $\varepsilon_{\chi}^{A}(E^*) \approx \varepsilon_{\chi}^{B}(E^*)$, and if the two surrogate reactions involve the same projectile and ejectile and the associated transfer-reaction cross sections are similar, then we can write:

$$R(E^*) = F\,\frac{N_{ejec-\chi}^{coin,A}(E^*)}{N_{ejec-\chi}^{coin,B}(E^*)} \tag{20}$$

where *F* is a constant that can be determined from the beam current, the target thickness and the experiment live time. If one measures *R*(*E**) and if $\sigma_{n,\chi}^{B}(E^*)$ is known, the cross section of interest can be derived:

$$\sigma_{n,\chi}^{A}(E^*) = \sigma_{n,\chi}^{B}(E^*)R(E^*) \tag{21}$$

From the previous lines it follows that the application of the surrogate ratio method involves the use of two surrogate reactions to form compound nuclei *A* and *B* with two targets and the same experimental setup. The advantage with respect to the “standard” surrogate approach studied in this work is that one only needs to measure the coincidence spectra for the two targets, thus solving the contaminant issue described in the previous section. In addition, it was shown in [Esc06] that the surrogate ratio approach is expected to be less sensitive to the spin-parity mismatch and to pre-equilibrium effects than the “standard” surrogate method. In fact, when the two nuclei *A* and *B* are close enough, effects due to the spin-parity mismatch or to pre-equilibrium are similar and cancel in the ratio. In reality, the comparison between neutron-induced data and results obtained with the surrogate-ratio method has shown that the

ratio method somewhat reduces, but does not eliminate the effect of the spin-parity mismatch at excitation-energies where the Weisskopf-Ewing limit does not apply, see [Esc12].

The surrogate ratio method has also some disadvantages. It requires two targets of neighbouring nuclei. This implies severe limitations when one is interested in a region dominated by radioactive nuclei, such as minor actinide isotopes, where target fabrication and handling is rather difficult. In addition, if one uses low gamma-energy resolution detectors, the surrogate-ratio method does not solve the problem of the background generated by light target contaminants because these nuclei emit gamma rays that pollute also the coincidence spectra. Moreover, this method introduces additional sources of uncertainty that contribute to the final uncertainty of the desired cross section. These sources are the quantities needed to determine the factor F and the uncertainty of the reference cross section $\sigma_{n,\chi}^{B}(E^*)$. Finally, significant deviations from neutron-induced data have been observed when there is an important mismatch between the S_n of nuclei A and B and the Q values of the surrogate reactions. An example will be shown in section 7.

According to us, the conditions under which the surrogate-ratio method can be used with confidence are still unclear. Although it is certainly desirable to continue to investigate this approach, we believe that it is important to pursue in parallel investigations on the standard surrogate method. In the surrogate ratio method, different effects might cancel or add up in a complicated manner and the interpretation of the results can be rather difficult.

6. Uncertainty analysis

The accurate determination of the uncertainties requires very detailed information on the experimental procedure, which is best known by the experimentalists who performed the measurements. In Article IV, we have shown that the variance of the measured probabilities can be strongly affected by the correlation between some of the quantities involved in the measurement. Moreover, in our experiments the probabilities were measured at different excitation energies with the same set-up. Thus, they are not completely independent, and the covariance between the fission probabilities at different energies should be determined, see Article IV. This information is very important for the evaluation process. Indeed, when data at different energies are partially correlated, there is a degree of “stiffness”, which implies that the data at a given energy cannot be modified independently from the data at the other energies. The covariance matrix of experimental data represents a key piece of information for providing the evaluated covariance matrix [Kaw08], which can have a strong impact in applications like e.g. the simulation of critical assemblies. In this manuscript we will discuss one aspect that influences significantly the variance of $P_{\chi}^{surro}(E^*)$ and we refer to Article IV and to [Duc15] for a complete description of the uncertainty analysis. To our knowledge this is the first time that such a rigorous study of uncertainties for transfer-induced decay probabilities has been performed.

According to eq. (11), the relative uncertainty of P_{χ}^{surro} at a given E^* is:

$$\frac{Var(P_{\chi}^{surro}(E^*))}{\left(P_{\chi}^{surro}(E^*)\right)^2}=\frac{Var(N_{ejec-\chi}^{coin}(E^*))}{\left(N_{ejec-\chi}^{coin}(E^*)\right)^2}+\frac{Var(N_{ejec}^{\text{singles}}(E^*))}{\left(N_{ejec}^{\text{singles}}(E^*)\right)^2}+\frac{Var(\varepsilon_{\chi}(E^*))}{\left(\varepsilon_{\chi}(E^*)\right)^2}$$
$$-2\cdot\frac{Cov(N_{ejec-\chi}^{coin}(E^*);N_{ejec}^{\text{singles}}(E^*))}{N_{ejec-\chi}^{coin}(E^*)\cdot N_{ejec}^{\text{singles}}(E^*)}-2\cdot\frac{Cov(N_{ejec-\chi}^{coin}(E^*);\varepsilon_{\chi}(E^*))}{N_{ejec-\chi}^{coin}(E^*)\cdot\varepsilon_{\chi}(E^*)}+2\cdot\frac{Cov(N_{ejec}^{\text{singles}}(E^*);\varepsilon_{\chi}(E^*))}{N_{ejec}^{\text{singles}}(E^*)\cdot\varepsilon_{\chi}(E^*)} \quad (22)$$

where *Cov* represents the covariance of the measured quantities. The covariance measures the inter-dependency between the quantities involved in the determination of the decay probability. Interestingly, eq. (22) shows that taking into account the covariance between the parameters affects the relative uncertainty of $P_{\chi}^{surro}(E^*)$. As described in Article IV, our experimental procedure allows us to neglect the two last covariance terms in eq. (22) for fission-probability measurements. This is also the case for gamma-decay probability measurements when the PHWT is used to derive ε_{gamma}, because in that case the determination of the efficiency is completely independent from the measured quantities. The situation is different when the EXEM is used to determine ε_{gamma}, as this method is based on the measured singles and coincidence spectra. In next section, we present a procedure to determine the term $Cov(N_{ejec-\chi}^{coin}(E^*);N_{ejec}^{singles}(E^*))$ that is different from the procedure described in Article IV and we will deepen into the meaning of the covariance of two quantities.

6.1. Covariance between coincidence and single events $Cov(N_{ejec-\chi}^{coin}(E^*);N_{ejec}^{singles}(E^*))$

For simplicity, in this section we will slightly modify the notation and replace $N_{ejec-\chi}^{coin}(E^*)$ by N^{coin} and $N_{ejec}^{singles}(E^*)$ by N^{sing}. To assess $Cov(N^{coin}; N^{sing})$ we can consider the number of single events as the union of two sets: the fission-fragment(or gamma)−ejectile coincidence set, associated to the random variable N^{coin}, and the set of ejectiles in anticoincidence with a fission fragment or a gamma, associated to the random variable N^{acoin}:

$$N^{sing} = N^{coin} + N^{acoin} \quad (23)$$

Using eq. (23) we obtain:

$$Cov(N^{coin}; N^{sing}) = Var(N^{coin}) + Cov(N^{coin}; N^{acoin}) \quad (24)$$

In Article IV it is shown that $Cov(N^{coin}; N^{acoin}) \approx 0$ and therefore:

$$Cov(N^{coin}; N^{sing}) = Var(N^{coin}) \quad (25)$$

The linear interdependence between N^{sing} and N^{coin} can be quantified with the correlation coefficient *Corr*, defined as the ratio of the covariance over the product of the standard deviations. It is a dimensionless quantity with values within the interval [-1;1]:

$$Corr(N^{coin}; N^{sing}) = \frac{Cov(N^{coin}; N^{sing})}{\sqrt{Var\left(N^{coin}\right)\cdot Var\left(N^{sing}\right)}} \quad (26)$$

Using eqs. (11), (25) and (26) it is easy to show that:

$$Corr(N^{coin}; N^{sing}) = \sqrt{P_\chi \varepsilon_\chi} \tag{27}$$

To derive eq. (27) we have assumed that the variables follow Poisson statistics. Eq. (27) says that the correlation between N^{sing} and N^{coin} increases with the decay probability P_χ and with the detection efficiency ε_χ, and that N^{sing} and N^{coin} are only fully (linearly) correlated if ε_χ =1 and P_χ=1. In our gamma-decay probability measurements, $P_{gamma} \approx 10\%$ and $\varepsilon_{gamma} \approx 10\%$, leading to $Corr(N^{sing}; N^{coin}) \approx 0.1$. In our fission-probability measurements, $P_{fission} \approx 50\%$ and $\varepsilon_{fission} \approx 50\%$ leading to $Corr(N^{coin}; N^{sing}) \approx 0.5$. Consequently, neglecting $Cov(N^{coin}; N^{sing})$ in fission experiments can lead to a significant overestimation of the uncertainty of the fission probability. Indeed, in Table 2 of Article IV we show that the relative uncertainty of the fission probability neglecting the covariance between N^{sing} and N^{coin} is overestimated by more than 30%.

Let us now present an alternative approach to evaluate $Cov(N^{coin}; N^{sing})$. The quantity $Cov(N^{coin}; N^{sing})$ measures how fluctuations in N^{sing} affect the value of N^{coin}. One way to determine it, is by making several (hundreds) measurements with exactly the same experimental conditions (geometry, beam intensity, etc.) and the same duration, and by representing the measured N^{sing} versus N^{coin}. Even though the experimental conditions are exactly the same, N^{coin} and N^{sing} will fluctuate, because they are random variables that follow Poisson statistics. Of course, this is generally not done. Alternatively, one can make groups of independent events with values for N^{sing} that are sampled from a Gaussian distribution centred at a given value of N^{sing} (e.g. 1000) and with a standard deviation equal to $\sqrt{N^{sing}}$. In this way one "simulates" how N^{sing} would have varied if one would have performed exactly the same experiment many times.

To perform this we have used the data from the Oslo experiment [Duc15]. Here, the telescope is divided in 56 strips with a solid angle of about 0.18% per strip. Because of this very small solid angle, the number of transfer reactions that are needed to have e.g. N^{sing} =1000 is very high. For this reason, assuming that N^{sing} is distributed according to a Gaussian distribution with mean value N^{sing} and standard deviation $\sqrt{N^{sing}}$ is completely justified. We have considered the ^{238}U(^{3}He,^{4}He) reaction because it has the advantage that there is no pollution from reactions on the target backing or on oxygen. The average fission probability $P_{fission}$ associated to this reaction is 0.37 and the fission detection efficiency is about 0.45, therefore according to eq. (27) we expect $Corr(N^{coin}; N^{sing}) \approx 0.408$. The following analysis was performed in the frame of the PhD thesis of Q. Ducasse [Duc15]. The events associated to each telescope strip were subdivided in groups of N^{sing} where the value N^{sing} of each group was randomly sampled from a Gaussian distribution with mean value $\left\langle N^{sing} \right\rangle$ and standard deviation $\sqrt{\left\langle N^{sing} \right\rangle}$. There was no overlap between the different groups, so that each group of N^{sing} events was completely independent from the others. For each strip we had a total number

of events that varied between 4000 and 5000. Therefore, if $\langle N^{sing} \rangle$=1000 we had around 4×56=224 independent groups. We also consider the interdependence between the quantities N^{acoin} and N^{coin}, where we recall that $N^{acoin} = N^{sing} - N^{coin}$.

Fig. 9 shows the results for different values of $\langle N^{sing} \rangle$. We can see that N^{sing} and N^{coin} are correlated, whereas N^{acoin} and N^{coinc} are uncorrelated. To determine quantitatively the variances and covariances from the data we use the estimators:

$$Var(N) = \frac{1}{n}\sum_{i=1}^{n}\left(N_i - \langle N \rangle\right)^2 \tag{28}$$

with variance

$$Var\left[Var(N)\right] = \frac{2Var(N)^2}{n} \tag{29}$$

and

$$Cov(N;N') = \frac{1}{n}\sum_{i=1}^{n}\left(N_i - \langle N \rangle\right)\left(N_i' - \langle N' \rangle\right) \tag{30}$$

In eqs. (28-30) $\langle N \rangle$ is given by $\langle N \rangle = \frac{1}{n}\sum_{i=1}^{n} N_i$ and n is the number of groups of data. The values for the estimators of the variances and covariances of the different sets of data are listed in Table 3.

$<N^{sing}>$	$Var(N^{sing})$	$<N^{coin}>$	$Var(N^{coin})$	$\sigma(Var(N^{coin}))$	$<N^{acoin}>$	$Var(N^{acoin})$	$Cov(N^{sing}, N^{coin})$	$Corr(N^{sing}, N^{coin})$	$Cov(N^{acoin}, N^{coin})$	$Corr(N^{acoin}, N^{coin})$
996	862	172	156	15	824	719	149	0.407	-7	-0.02
499	475	86	82	5	413	401	78	0.395	-4	-0.02
200	191	34	35	1.4	165	158	34	0.415	-1.3	-0.02

Table 3: Variances and covariances of N^{sing}, N^{coin} and N^{acoin} obtained for the ^{238}U(^{3}He,^{4}Hef) reaction. The experimental data were divided in independent groups with different values of $\langle N^{sing} \rangle$, representing the average number of N^{sing} events in each group.

Table 3 shows that the values of $Cov(N^{sing}, N^{coin})$ (eighth column) agree very well with $Var(N^{coin})$ (fourth column), thus demonstrating the validity of eq. (25). More precisely, the values of $Cov(N^{sing}, N^{coin})$ are always well within the error bars of $Var(N^{coin})$, which are given by $\pm\sigma(Var(N^{coin}))$ in the fifth column. We also see that the values for $Corr(N^{sing}, N^{coin})$ (ninth column) agree very well with the expected value of 0.408 obtained with eq. (27). The method proposed here can be used to evaluate the covariance between any other measured quantities and has been used in [Duc15] to evaluate the covariance of N^{sing} and N^{coin} with ε_{gamma}, when ε_{gamma} is obtained with the EXEM.

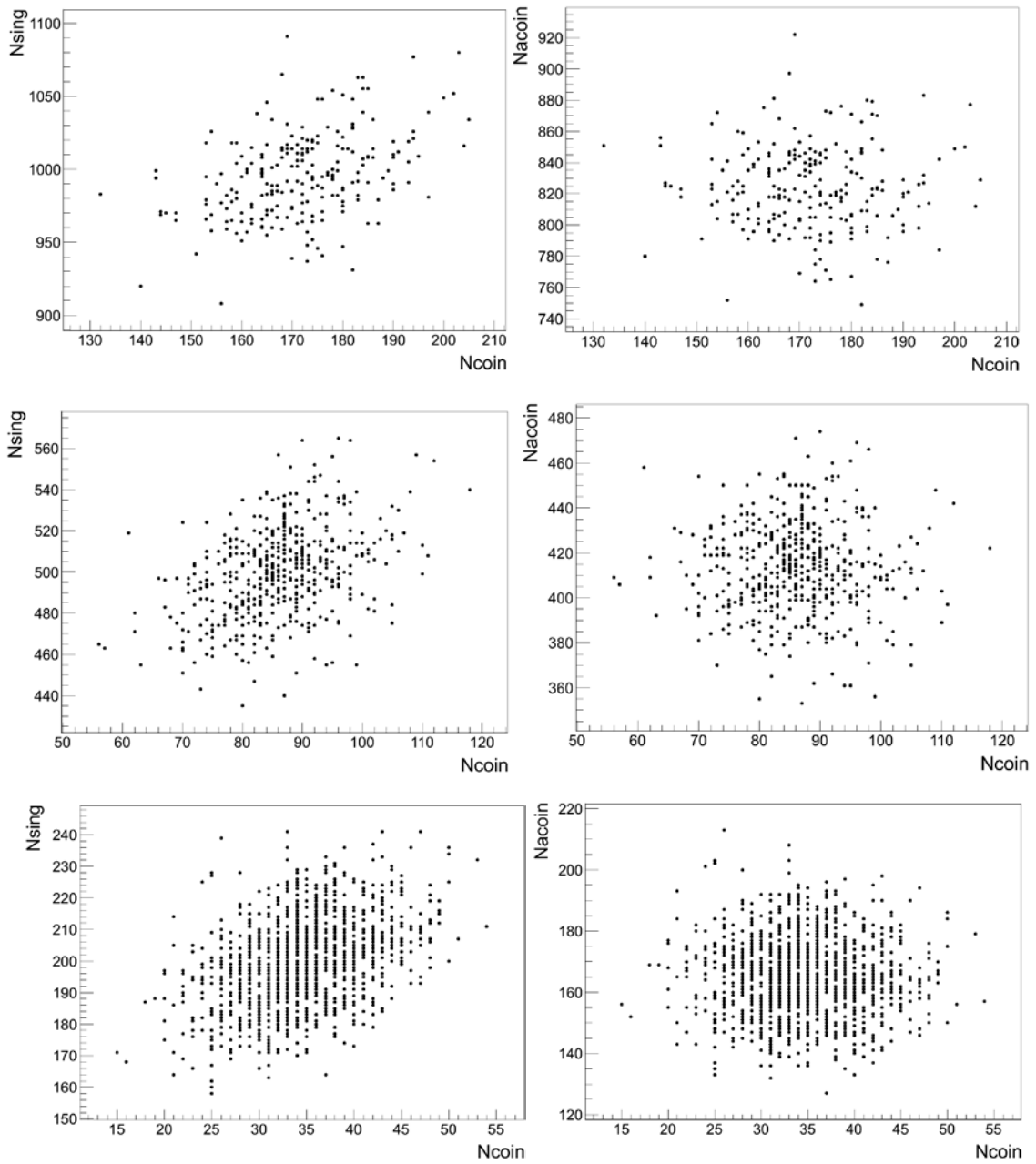

Figure 9: (Left) N^{sing} as a function of N^{coin}. (Right) N^{acoin} as a function of N^{coin}. N^{sing} has been sampled from a Gaussian distribution centred at $\langle N^{sing} \rangle$ and with standard deviation $\sqrt{\langle N^{sing} \rangle}$. For the two upmost panels $\langle N^{sing} \rangle$ = 1000, for the middle panels $\langle N^{sing} \rangle$ = 500 and for the lowest panels $\langle N^{sing} \rangle$ =200. The data correspond to the ^{238}U(^{3}He,^{4}Hef) reaction.

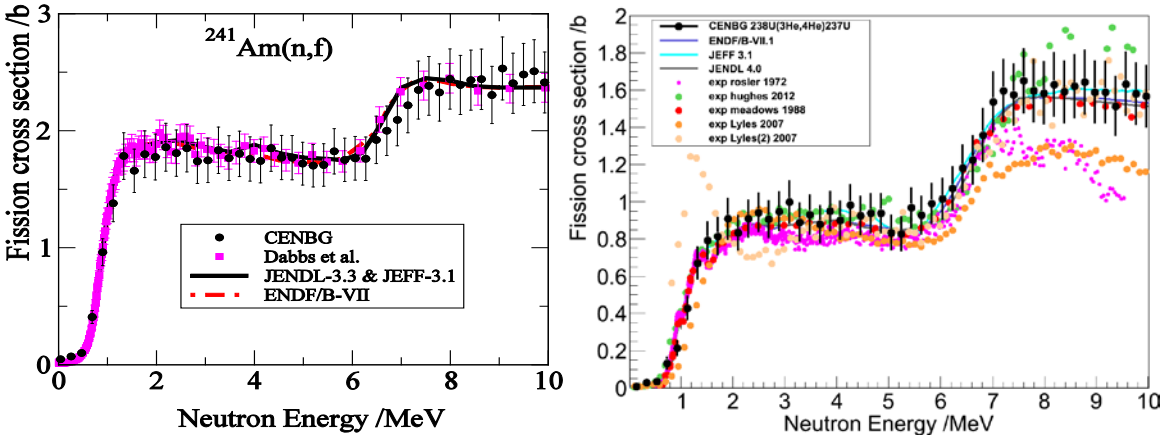

Figure 10: Fission cross section as a function of neutron energy. On the left are represented the results for ^{241}Am obtained with the ^{243}Am(^{3}He, ^{4}He) reaction and on the right the preliminary results for ^{236}U obtained with the ^{238}U(^{3}He, ^{4}He) reaction [Duc15]. Our results are represented by the black symbols, the color symbols represent other experimental data and the lines the evaluations.

7. Comparison between results obtained with the surrogate method and neutron-induced data

As stated above, to study the validity of the surrogate-reaction method, results obtained using surrogate reactions have to be compared to neutron-induced data. In the following we present some of the results obtained by the CENBG collaboration that are representative of our current understanding of the degree of applicability of the surrogate reaction method as represented by eq. (9).

7.1. Selected results for fission

The left part of Fig. 10 shows our results for the fission cross section of ^{241}Am obtained with the surrogate reaction ^{243}Am(^{3}He, ^{4}He), compared to the neutron-induced cross section by Dabbs et al. [Dab83] and to international evaluations. To obtain this cross section we have multiplied the measured fission probability (see Article IV) by the compound-nucleus cross section σ_n^{CN} calculated with a semi-microscopic deformed optical-model potential [Bau01, Bau00]. We can see that above a neutron equivalent energy of about 0.5 MeV there is an excellent agreement between our results and the neutron-induced data. The fission cross section of ^{236}U obtained with the ^{238}U(^{3}He, ^{4}He) surrogate reaction is represented on the right side of Fig. 10 [Duc15]. In this case, the compound nucleus cross section was obtained with the ECIS code [Cap13]. Above about 0.5 MeV, our results are in very good agreement with the neutron-induced data by Meadows et al. and the evaluations. It is interesting to notice that pre-equilibrium emission was not subtracted from the compound-nucleus cross sections used for the two reactions ^{241}Am(n,f) and ^{236}U(n,f), indicating the negligible contribution of pre-equilibrium decay for the energies considered. We find a very good agreement with the neutron-induced data down to relatively low neutron energies for the ensemble of our fission data. The fission data measured by the Livermore group present in general larger

discrepancies at the lowest energies. In many cases their results are somewhat shifted with respect to the neutron-induced data at the fission threshold, see e.g. the data labelled Lyles 2007 in Fig. 10. Before attributing this to the breaking down of the Weiskopf-Ewing limit, it is necessary to exclude systematic errors due, for example, to deficiencies in the beam-energy definition or in the energy calibration of the telescopes.

The data labelled Lyles 2007 [Lyl07] on the right side of Fig. 10 correspond to a measurement using the same surrogate reaction as in our experiment. However, in the experiment by Lyles et al., the ejectiles were detected at forward angles and the singles spectrum was polluted at high excitation energies by ejectiles coming from reactions with the target backing and light target contaminants. This leads to a clear underestimation of the fission cross section above 7 MeV. In our case, the ejectiles were detected at backward angles and the contaminant events were located at equivalent neutron energies well above 10 MeV. The data labelled Lyles (2) 2007 were obtained using the surrogate ratio method with the surrogate reactions ^{238}U(^{3}He, ^{4}He) and ^{235}U(^{3}He, ^{4}He) [Lyl07]. The discrepancies found at the fission threshold were attributed, by the authors, to angular-momentum effects. The most recent measurements by Hughes et al. were also obtained with the surrogate ratio method using the ^{238}U(p,d) and ^{236}U(p,d) reactions. The authors explain the disagreement observed beyond 7 MeV by the differences between the Q-values of the two surrogate reactions and the S_n values of the ^{237}U and ^{235}U compound nuclei.

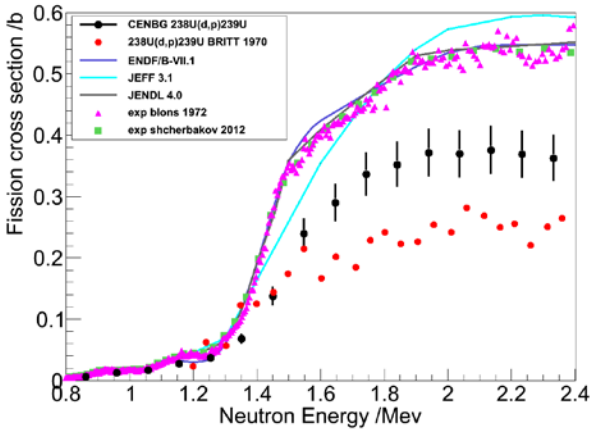

Figure 11: Preliminary neutron-induced fission cross sections of ^{238}U measured with the ^{238}U(d,p) reaction [Duc15]. Experimental neutron-induced data, the surrogate-reaction data by Britt et al. [Bri70] and several evaluations are also shown for comparison.

Radioactive-beam experiments are expected to provide much-needed information on compound-nuclear reactions involving short-lived nuclei, see Chapter 4. Since free-neutron targets are not yet available, surrogate reactions, such as (d,p), might be used to “simulate” neutron-induced reactions in inverse kinematics. Intuitively, the process of transferring a neutron from a deuteron projectile to a target seems very similar to bombarding the same target with a neutron beam. Fig. 11 shows preliminary results for the fission cross section of ^{238}U obtained from the ^{238}U(d,p) reaction as a function of equivalent neutron energy [Duc15]. In this case, the compound nucleus cross section has been calculated by the phenomenological optical model from TALYS [Rom13]. Below about 1.3 MeV, the surrogate-reaction results are in good agreement with the neutron-induced data. Above this energy our results are

clearly below the neutron-induced results. We observe differences up to 35%. Interestingly, the data by Britt and Cramer [Bri70] obtained using the same ^{238}U(d,p) reaction with a beam energy of 18 MeV are clearly below our data. The reason for the discrepancy with respect to the neutron-induced data may be that the neutron transferred to the ^{238}U target nucleus in the stripping (d,p) reaction escapes into the breakup phase space before the ^{239}U nucleus becomes a compound nucleus. This leads to a background of "sterile" protons that contaminates the singles proton spectrum. These protons are not correlated with the compound-nucleus formation and lead to a decrease of the measured fission probability, as shown by eq. (11). This hypothesis was already drawn by Britt and Cramer [Bri70] but only now it starts to attract theoretical efforts [Esc12]. In addition, because the oxidation of the target cannot be completely avoided, fusion of the deuteron beam with oxygen and the subsequent evaporation of protons have also to be taken into account. Again, this leads to the production of sterile protons, decreasing the measured fission probability. Therefore, this process might also be responsible for the differences observed between the surrogate data and the neutron-induced data, as well as between the two surrogate-reaction results. Indeed, in our experiment we limited as much as possible the oxidation of the ^{238}U metallic target, whereas the ^{238}U target used by Britt and Cramer was an oxide. To address this issue, detailed fusion-evaporation calculations will be performed with the PACE4 code. Moreover, it would also be interesting to make measurements for the ^{238}U(d,p) reaction at different incident energies, to see whether we can reproduce Britt and Cramer's results.

Deuteron breakup is a complex process. One distinguishes between elastic and inelastic breakup. In the elastic breakup, the impinging deuteron breaks up due to the Coulomb and/or nuclear interaction with the target and the resulting proton and neutron move apart leaving the target nucleus in the ground state. The inelastic breakup includes the processes in which the incident deuteron breaks up and the resulting proton and neutron move apart but the target nucleus is excited, as well as the cases where the resulting neutron fuses with the target nucleus leading to a compound nucleus. Moro et al. [Mor15] are currently performing CDCC (Continuum Discretized Coupled-Channel) calculations to compute the elastic and inelastic breakup cross sections for the ^{238}U(d,p) reaction at 15 and 18 MeV incident energy. In these calculations, the absorption of the neutron due to its interaction with the target nucleus is represented by the imaginary part of the neutron-target optical potential. However, the absorption produced by this potential accounts also for other processes, like e.g. target excitation, and it is not obvious to disentangle the different contributions to the inelastic breakup. The first results obtained at 15 MeV show that, in the range from 0 to about 2 MeV neutron energy, the elastic breakup gradually increases with neutron energy and reaches a maximum of 10% of the total cross section at 2 MeV. An attempt to extract the compound-nucleus cross section from these calculations is currently under study [Mor15].

Note that the problems just described for the (d,p) reaction are not present when using the (^{3}He,^{4}He) reaction, which gives results in good agreement with the neutron-induced data. For this pickup reaction, a neutron is removed from a deeply-lying bound state of the target, so there is no significant escape of neutrons before the compound nucleus is formed. Moreover, fusion of the ^{3}He beam with target oxygen and subsequent alpha evaporation may occur, but

the energies of the evaporated alpha particles (predicted by PACE4 calculations) are too low to traverse the ΔE part of the SiRi telescope.

7.2. Selected results for capture

As a first step, we studied the surrogate method applied to neutron-induced capture cross sections in the rare-earth region. In particular, we studied the ^{174}Yb(^{3}He,^{4}Heγ)^{173}Yb and ^{174}Yb(^{3}He,pγ)^{176}Lu transfer reactions as surrogates for the ^{172}Yb(n,γ) and ^{175}Lu(n,γ) reactions, respectively. We focused on the study of the ^{172}Yb(n,γ) and ^{175}Lu(n,γ) cross sections because they present the advantage to be very well known. The measurement was performed at the Tandem accelerator of the IPN Orsay in 2010 and is described in Article II. The obtained results for the radiative-capture cross sections are compared to existing neutron-induced data and to available evaluations on the left side of Fig. 12. Our surrogate-reaction data are a factor 10 higher than the neutron-induced data at the lowest energies.

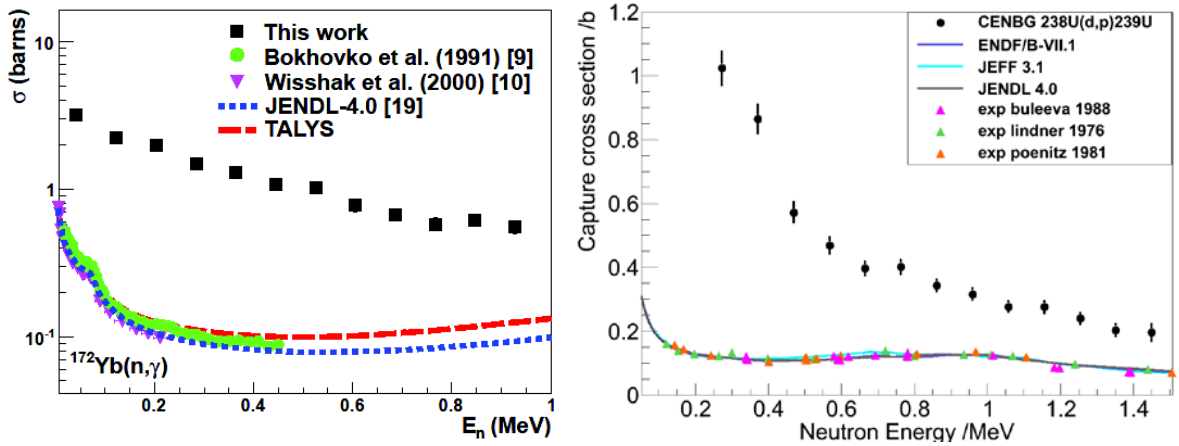

Figure 12: Radiative-capture cross sections as a function of neutron energy. On the left are shown the results for ^{172}Yb obtained with the ^{174}Yb(^{3}He,^{4}He) reaction and on the right preliminary results obtained with the ^{238}U(d,p) reaction. Our results are represented by the black symbols, the color symbols represent neutron-induced data and the lines the evaluations.

The differences observed for the capture cross sections may be due to the higher angular momentum induced by transfer reactions. For excitation energies close to S_n, gamma decay competes with neutron emission, leading to the population of the ground state or the first excited states of the residual nucleus A-1. Neutron emission at $E^* \approx S_n$ is very sensitive to the spin of nucleus A^*. Indeed, the low-lying states of the residual nucleus A-1 have a given spin and the average orbital angular momentum carried by the emitted neutron is in general quite low (around 1 $\hbar$). Therefore, if the angular momentum induced in the surrogate reaction is much larger than the angular momentum of the first states of nucleus A-1, neutron emission to the low-lying states of the residual nucleus will be strongly suppressed and the de-excitation will proceed essentially by gamma emission. In contrast, for a neutron-induced reaction, neutron emission to the ground state and to the first excited states of the residual nucleus is the dominant way of de-excitation right above S_n. Similar conclusions have been drawn by the

Livermore group in USA [Sci10], who observed important discrepancies between the surrogate-reaction data and the neutron capture cross sections of several Gd isotopes.

The spin/parity selectivity of neutron emission decreases strongly as the level density of the residual nucleus A-1 increases. Therefore, the discrepancies between surrogate-reaction results and neutron-induced data are expected to decrease as the mass and the E^* of the decaying nucleus increase. The right part of Fig. 12 presents preliminary results for the ^{238}U capture cross section as a function of equivalent neutron energy, obtained in the ^{238}U(d,p) reaction [Duc15]. The capture cross section obtained with the surrogate method is several times higher than the neutron-induced one over the whole energy range. At high energies, the discrepancies between the surrogate data and the neutron-induced data are somewhat smaller than for the rare-earth nuclei investigated in Article II. A minimum factor of about 2.5 is reached at 1 MeV. Deuteron breakup described in the previous section complicates the interpretation of the results obtained with the ^{238}U(d,p) reaction, since the presence of protons originating from the breakup of the deuteron in the singles spectrum reduces also the measured gamma-decay probability.

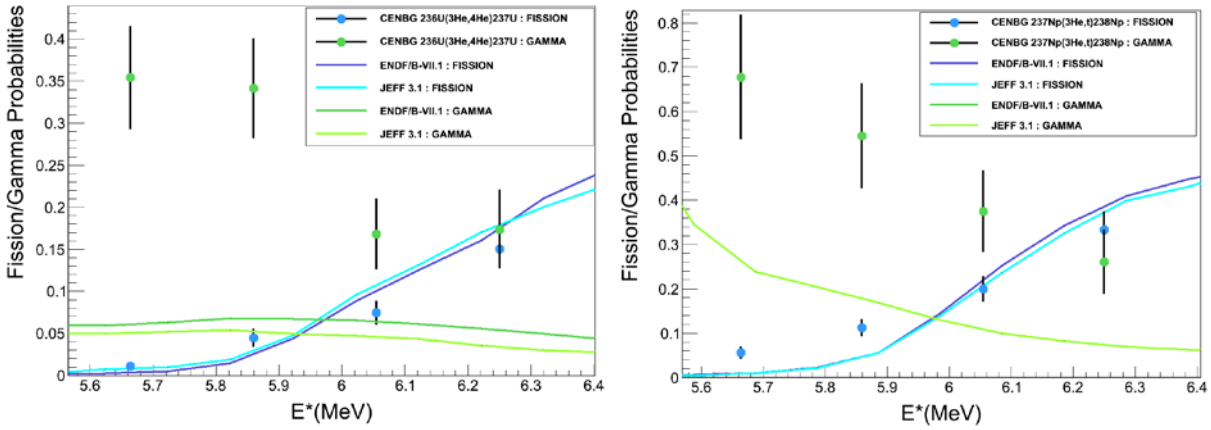

Figure 13: Fission (blue) and gamma-decay (green) probabilities as a function of excitation energy. The left panel shows the results obtained with the ^{238}U(^{3}He,^{4}He) reaction and the right panel with the ^{238}U(^{3}He,t) reaction. The full lines represent the evaluations. The decay probabilities have been obtained by dividing the evaluated neutron-induced cross section by the compound-nucleus cross section obtained with the ECIS optical potential [Cap13].

7.3. Simultaneous measurement of gamma-decay and fission probabilities

It has been argued that the suppression of neutron emission caused by the spin-parity mismatch would imply also a significant increase of the fission cross section [Rom12]. Yet, the available data seem to indicate that fission is much less sensitive to spin/parity differences than radiative capture. However, to really proof that fission behaves differently from gamma-decay, fission and gamma-decay probabilities have to be simultaneously measured for the same nucleus at the same excitation energy. The surrogate reaction ^{238}U(^{3}He,t)^{238}Np is a good candidate for such a study, because the neutron-induced capture cross section of ^{237}Np has relatively high values at the fission threshold. Therefore, for this nucleus we expect a sizeable

gamma-decay probability at the fission threshold. This is not the case for ^{239}U, for example, where fission sets in at a neutron energy of about 1 MeV. At the Oslo cyclotron we measured simultaneously the fission and the gamma-decay probability for the ^{238}U(^{3}He,t)^{238}Np and the ^{238}U(^{3}He,^{4}He)^{237}U reactions [Duc15]. Although the overlap region between fission and gamma decay of ^{237}U is somewhat smaller than for ^{238}Np, the comparison of the results obtained with the two surrogate reactions is interesting, because the populated spin/parity distributions and the structure of the involved nuclei are different. As discussed in section 4, the measurement of the gamma-decay probability in the overlap region is challenging, as it requires discriminating the gamma rays emitted by nucleus A^* from the prompt gamma rays emitted by the fission fragments.

The preliminary results displayed in Fig. 13 show large discrepancies between the gamma-decay probabilities obtained with surrogate and neutron-induced reactions, whereas a fairly good agreement is observed for the fission probabilities. Unfortunately, our results are affected by significant uncertainties due to the large error bars on the fission efficiency, and the limited statistics caused by the low ^{3}He beam intensity. We recall also the issue with the beam-energy definition at the Oslo cyclotron. For these reasons, we plan to perform a new dedicated experiment to measure these data more accurately.

The explanation of the results presented in Fig. 13 is not obvious. At excitation energies above S_n, the level density of actinides is quite high so that the number of open channels for gamma-decay is not very sensitive to the populated spin. Similarly, the good agreement observed for fission can be interpreted as the result of a high level density also on the top of the fission barriers and a weak sensitivity to the spin. If neutron emission is suppressed or significantly reduced for the surrogate reactions, one would expect that both, fission and gamma-decay probabilities increase. One may also question the validity of the hypothesis of compound-nucleus formation in the surrogate reactions. However, it is commonly believed that fission can only proceed through the formation of compound nucleus. Indeed, there is a sizable probability to cross the fission barrier (see Chapter 3) only for the macrostate of maximum entropy, where all the states on top of the barrier have equal probability to be populated [Wig38]. If there would be a mixture of events related to direct and to compound-nucleus reactions in the singles spectra, fission would not be possible for the direct events and the fission probability would be lower than the neutron-induced fission probability.

8. Short-term perspectives

In the previous section we have shown the interest of measuring simultaneously fission and gamma-decay probabilities in surrogate experiments. We have developed an experimental set-up that is optimized for this purpose. The setup is shown in Fig. 14. It consists of a reaction chamber housing the target, two particle telescopes placed at backward angles and the fission detector. The chamber is surrounded by two types of gamma detectors: four C_6D_6 liquid scintillators and six high-purity germanium detectors. Each telescope is composed of a 300 μm position-sensitive Si detector followed by a SiLi detector with 5 mm thickness. The fission detector consists of 16 solar cells positioned at different angles. This segmentation will allow us to measure the fission-fragment angular anisotropy. The vacuum chamber is

equipped with an airlock to isolate the ^{252}Cf source (which is needed to determine the solid angle of the fission detector) from the environment during the transportation from the glove box, where it will be mounted, to the experimental setup. A second airlock will be used for a target ladder containing the ^{238}U and ^{208}Pb targets, and the target backing. In April 2015, we will use this setup to measure simultaneously the fission and gamma decay probabilities for the ^{238}U(^{3}He,t) and ^{238}U(^{3}He,^{4}He) surrogate reactions at the Tandem accelerator of Orsay. The Tandem accelerator is very well suited for this measurement because it provides a high quality ^{3}He-beam with excellent energy resolution and definition, and significantly higher intensities than at the Oslo cyclotron (more than a factor 20).

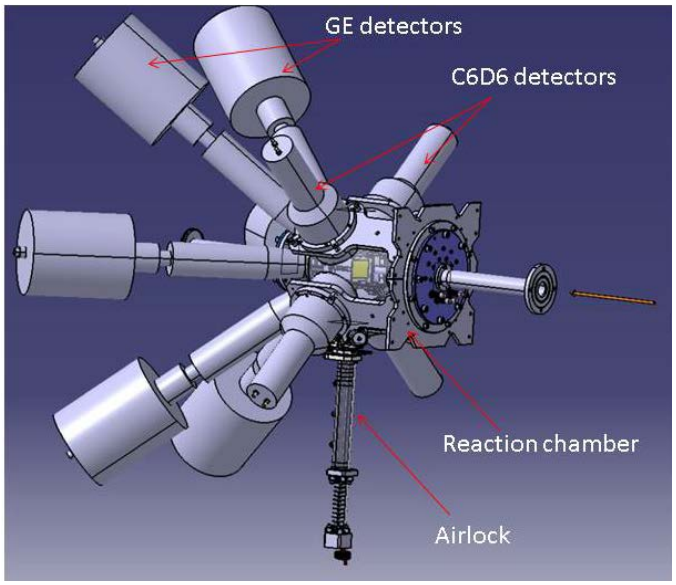

Figure 14: Schematic view of the experimental setup for simultaneous measurement of fission and gamma-decay probabilities.

8.1. New strategy for radiative capture reactions

Our results show that the surrogate method as represented by eq. (9) is not suited for determining capture cross sections. However, surrogate reactions remain presently the only possibility to access highly radioactive nuclei. To improve on the applicability of the method, a different strategy is needed:

(i) Predict the spin/parity distributions populated in surrogate reactions.
(ii) The calculated spin/parity distributions and the data obtained from surrogate reactions are used to determine key input information of the Hauser-Feshbach calculation, such as the parameters of the gamma-ray strength-function and the level-density.
(iii)The tuned Hauser-Feshbach calculation is then used to determine the capture cross section of interest.

Recent results obtained by J. Escher et al. [Esc13] show that this new strategy is very promising. Indeed, the uncertainties of the Hauser-Feshbach calculations are considerably reduced when surrogate-reaction data are used to constrain model parameters. [Esc13] also shows that this method can be used to determine (n,n') and (n,2n) cross sections.

We would like to contribute to the development of this new strategy for determining capture cross sections and to test its validity. This strategy requires predicting the spin/parity distributions populated in the surrogate reaction. As already said, this is a difficult task as it requires the modeling of the direct population of an unbound excited state in the continuum and its damping into a compound nucleus [Esc12, Car14]. Due to the complex structure of deformed nuclei, first calculations have been carried out by J. Escher et al. for nearly spherical Zr isotopes [Esc13]. Here, we propose to use the setup shown in Fig. 14 to measure the probability for specific gamma transitions as a function of angle and excitation energy of the spherical ^{207}Pb formed in the ^{208}Pb(^{3}He, ^{4}He) reaction, as well as the gamma-decay probability of ^{207}Pb. Note that the reactions on ^{208}Pb are anyway needed for the energy calibration of the gamma detectors and of the particle telescopes. Therefore, this measurement can be performed during our next experiment at Orsay. The measured gamma-decay probability of ^{237}U can also be used to test the new strategy at a later stage, when the models are sufficiently developed to treat heavy, deformed nuclei.

8.2. Data on short-lived heavy actinides

Our new setup can be used to measure fission and gamma-decay probabilities of short-lived actinides such as $^{239\text{-}243}$Am and $^{238\text{-}241}$Pu. These nuclei are important for reactor applications, in particular the neutron-induced cross sections of ^{242}Am($T_{1/2}$(GS)=16 h), ^{240}Am($T_{1/2}$=2.1 d) are relevant for the incineration of ^{241,243}Am and the neutron-induced fission cross section of ^{238}Pu($T_{1/2}$=87.7 y) is needed for the sodium fast reactor, as well as for transmutation schemes. Due to the short half-lifes, the corresponding neutron-induced cross sections present important discrepancies or are simply not available. The associated decay probabilities can be measured via ^{3}He-transfer and inelastic-scattering reactions on ^{240}Pu ($T_{1/2}$=6563 y) and ^{242}Pu($T_{1/2}$=3.75·10^{5} y) targets. Unfortunately, these targets are not yet available.

9. Conclusions

The surrogate reaction method is an indirect method to determine neutron-induced cross sections of short-lived nuclei. We have presented the fundamental ideas underlying the surrogate method and the conditions under which it is applicable. Given the limitations of current theoretical models, the validity of the method has to be evaluated by comparing the results obtained with the surrogate method with already existing neutron-induced data. The experimental methods used by the CENBG collaboration to measure the fission and gamma-decay probabilities have been presented, emphasizing the major experimental difficulties. The major problems to be faced are the determination of the gamma-cascade detection efficiency at the highest excitation energies, and the background due to target contaminants. In our studies we have also made a particular effort to determine the uncertainty of the measured probabilities in a complete and very rigorous way, taking into account the correlations of the different measured quantities.

Some selected results obtained by the CENBG collaboration have been discussed. For the ^{238}U(d,p) reaction we have observed a clear reduction of the fission probability which can be (at least partly) attributed to deuteron breakup. Our data are above the data measured by Britt

et al. [Bri70] with the same reaction at 18 MeV incident energy. To understand these results we will compare our data to model calculations describing the formation of a compound nucleus after the breakup of the weakly bound incident deuteron. It would also be interesting to perform measurements of the ^{238}U(d,p) reaction at different incident energies.

The ensemble of the data measured by the CENBG collaboration indicates that fission is much less sensitive to the reaction used to produce the decaying nucleus than radiative capture. In fact, the clearest proof of the weaker sensitivity of fission to the entrance channel has been given by the preliminary results measured at Oslo, where fission and gamma-decay probabilities have been measured simultaneously for one nucleus at the same excitation energy in the ^{238}U(^{3}He,^{4}He) and ^{238}U(^{3}He,^{4}He) surrogate reactions. Unfortunately, the data measured at Oslo suffer from large uncertainties. Therefore, we will measure them again with better accuracy in our next experiment at the Tandem accelerator of the IPN Orsay. The interpretation of the preliminary results obtained at Oslo is not obvious. We think that our data can considerably help in the understanding of the results obtained so far with the surrogate method and, more generally, that they can provide a stringent test to the statistical model.

Our results show that the surrogate method as expressed by eq. (9) cannot be used to infer radiative capture cross sections. However, surrogate reactions remain presently the only possibility to extend our studies to the most radioactive nuclei. A different strategy is thus required: it is necessary to develop theoretical models to predict the spin/parity distributions populated in the surrogate reactions. Experiments are required to test and validate these models. For example, gamma-decay probabilities and gamma-transition intensities are very sensitive to the angular-momentum and parity distributions. Once these distributions are known, the data obtained from surrogate reactions can be used to determine key input information of the statistical model, such as fission barriers, transmission coefficients and level-density parameters, and in that way considerably improve the model predictions for the cross sections of interest.

The continuation of our measurements, with the techniques presented in this chapter, depends on the production of good-quality, pure targets that are presently rather difficult to obtain. Luckily, the target issue can be overcome by measurements in inverse kinematics with radioactive beams, which offer very interesting new possibilities, as will be shown in Chapter 4.

Articles:

Article I: G. Kessedjian, B. Jurado et al., Phys. Lett. B 692 (2010) 297
Article II: G. Boutoux, B. Jurado et al., Phys. Lett. B 712 (2012) 319
Article III: G. Boutoux, B. Jurado et al., Nucl. Instr. Meth. 700 (2013) 59
Article IV: G. Kessedjian, B. Jurado et al., Phys. Rev. C 91 (2015) 044607

Chapter 3: Partition of intrinsic excitation energy and unpaired nucleons in fission: the energy-sorting process

1. The context: development of the GEneral Fission code (GEF)

Fission is a large-scale collective motion where a heavy nucleus evolves into two individual nuclei with nuclear properties that considerably differ from those of the initial nucleus. This transition from a mononuclear to a di-nuclear system involves a drastic rearrangement of nucleons and energy, and its understanding is highly important from the fundamental point of view. The understanding of fission is also relevant for applications. Indeed, fission is the mechanism that is at the origin of most of the energy that is generated in nuclear reactors, it is also important in nuclear medicine for the production of radio-isotopes and for the production of beams in radioactive ion-beam facilities.

Fig. 1 shows a schematic view on the evolution of a fission event after excitation of a heavy nucleus by neutron absorption. Thanks to dissipation, i.e. the coupling between intrinsic (single-particle or quasi-particle excitations) and collective degrees of freedom (coordinate motion of the ensemble or a part of nucleons), part of the intrinsic excitation energy generated by neutron absorption feeds a quadrupole vibration of larger and larger amplitude. The stretching of the nucleus leads to some necking and the fission fragments start to emerge. Because of the mutual Coulomb repulsion, the nascent fragments are generally highly deformed and finally fly apart with high kinetic energy after scission. Scission is the point where the fragments separate and are not in contact anymore. When the distance between the separated fragments is large, the Coulomb repulsion between the fragments decreases and the fragments eventually snap back to a smaller deformation. Again, due to the coupling between collective and intrinsic degrees of freedom, the deformation energy transforms into intrinsic excitation energy of the fully accelerated fragments. Since fission fragments are neutron-rich, the deexcitation proceeds almost exclusively by prompt-neutron emission and, subsequently, by prompt-gamma emission. The situation represented in Fig. 1, corresponds to low-energy fission, i.e. to initial excitation energies of few MeV. At higher excitation energies, neutrons, charged particles and gamma rays may also be emitted before scission.

In Chapter II, we have already stressed the importance of fission cross sections for reactor physics. However, a good knowledge of all the other fission observables is also necessary. Fission-fragment isotopic yields (i.e. the fission-fragment yields as a function of their mass A and charge Z) play a significant role in reactor physics, as they allow one to determine the radioactivity generated by the fission products, and in particular the decay heat. The decay heat is the energy that is generated after the reactor has been shut down, mainly due to the beta decay of fission fragments. If no cooling system removes the decay heat from a newly shut down reactor, the decay heat may cause the core of the reactor to reach unsafe temperatures within a few hours or days. Good knowledge of the multiplicity and the energy spectrum of prompt-fission neutrons is also essential, as the prompt-fission neutrons ensure

the maintenance of the chain reaction. There is also a clear need for an accurate knowledge of the multiplicity and the energy spectrum of prompt gamma-rays emitted by the fission fragments. Indeed, approximately 10% of the total energy released in fission is due to γ rays, of which around 40% of the heat originates from prompt gamma rays.

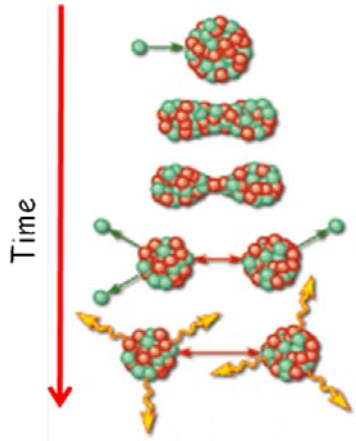

Figure 1: Schematic time evolution of the neutron-induced fission of a heavy nucleus.

Important progress has been made in the theory of fission over the last decades. For example, the potential-energy surface of the fissioning systems has been systematically mapped in five-dimensional deformation space [Möl01]. Stochastic methods [Ran11] and self-consistent microscopic approaches [Gou05] have been developed for dynamical calculations of low-energy fission. However, these calculations still face severe restrictions, due to the limited computing power and the lack of suitable theoretical formalisms. For this reason, even though these models are already very successful in describing general trends, they fail to properly reproduce experimental data.

This chapter includes the work done in collaboration with Karl-Heinz Schmidt for the development of the GEF code. Our motivation for this collaboration was to produce a fast code that is able to predict all fission observables with the required accuracy of technological applications. GEF is a semi-empirical code, it combines general laws of quantum and statistical mechanics with specific experimental information. Some of the physics ideas behind GEF will be thoroughly discussed in the next sections. Because it is based on robust physical concepts, GEF provides reliable predictions for essentially all fission observables of a broad range of fissioning nuclei, extending from Po to Sg, and covers spontaneous fission to fission at about 100 MeV excitation energy. Contrary to most of the fission models used in reactor physics, GEF can give also reliable results for nuclei where no experimental information is available.

A complete description of the code can be found in [Sch14]. The good quality of GEF predictions has been demonstrated via a thorough comparison to an enormous amount of experimental data, covering all the different fission observables and a broad range of fissioning nuclei and excitation energies, see [Sch14]. Ref. [Sch14] demonstrates that GEF can be a powerful tool for the evaluation of nuclear data. In the following we will describe

how the partition of the pre-scission excitation energy and unpaired nucleons between the fragments is determined in GEF, demonstrating that GEF is also a powerful tool for fundamental physics.

2. Low-energy fission

Before entering into the subject, it is important to clarify the different origins of the intrinsic excitation energy all along the fission process in low-energy fission. We will also present some key experimental data sensitive to the partition of energy and unpaired nucleons between the fragments.

In the frame of the liquid-drop model, the competition between the surface tension and the Coulomb repulsion during the stretching of the nucleus leads to a potential energy as a function of elongation that presents a fission barrier. After the fission barrier (or the saddle point), the Coulomb repulsion leads to a rapid decrease of the potential energy. This is shown on the left side of Fig. 2, which represents the potential-energy surface according to the liquid-drop model as a function of elongation and mass asymmetry for ^{236}U [Kar08]. As we can see, there is only one fission valley on the way from saddle to scission corresponding to symmetric fission. Therefore, the fission-fragment mass yields predicted by the liquid-drop model are symmetric. The right side of Fig. 2 shows the potential-energy surface including shell effects. We can see now some structure at the saddle point, leading to a double-humped fission barrier and two well separated asymmetric fission valleys on the descent from saddle to scission. The different fission valleys lead to different humps in the fragments mass yields, which are known in literature as fission channels [Bro90]. One distinguishes mainly between three fission channels: the symmetric channel that generally results from the liquid-drop potential, and the two asymmetric channels caused by shell effects: the less asymmetric channel is known as the Standard 1 (S1) and the more asymmetric as the Standard 2 (S2) channel.

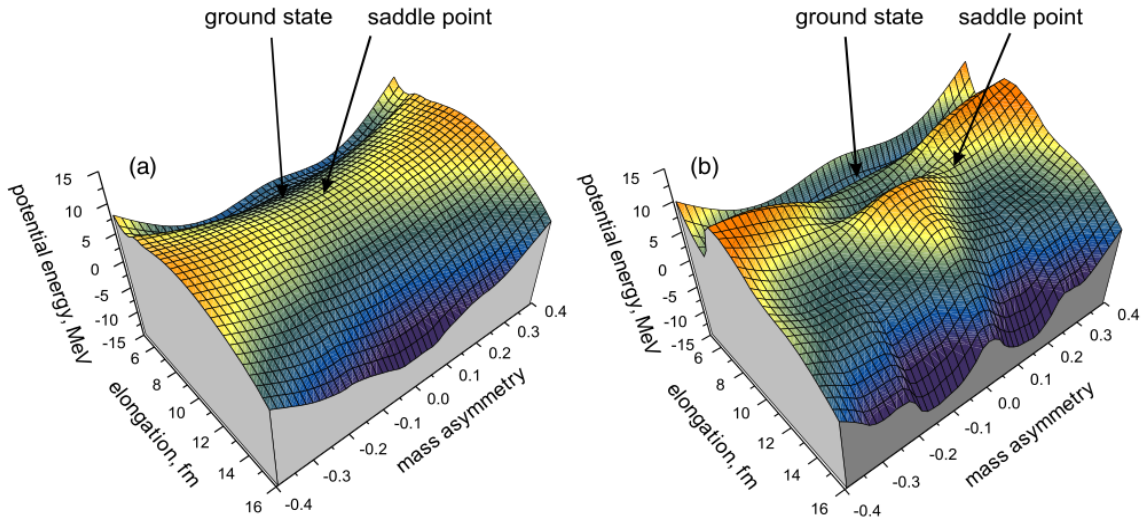

Figure 2: Potential-energy surface for the fission of ^{236}U according to the liquid-drop model (left) and with inclusion of shell effects (right). Figure taken from [Kar08].

2.1. Energetics of the fission process

Fig. 3, which is taken from Article VII, gives a one-dimensional view on how the energy available in the fission process (equal to the Q value and the kinetic energy of the neutron in the centre of mass) is divided into potential, intrinsic, collective and kinetic energy as a function of deformation. The inset of Fig. 3 shows that the energy release due to the decreasing potential energy before scission is partly dissipated into excitations of collective normal modes and intrinsic excitations. The remaining part feeds the pre-scission kinetic energy.

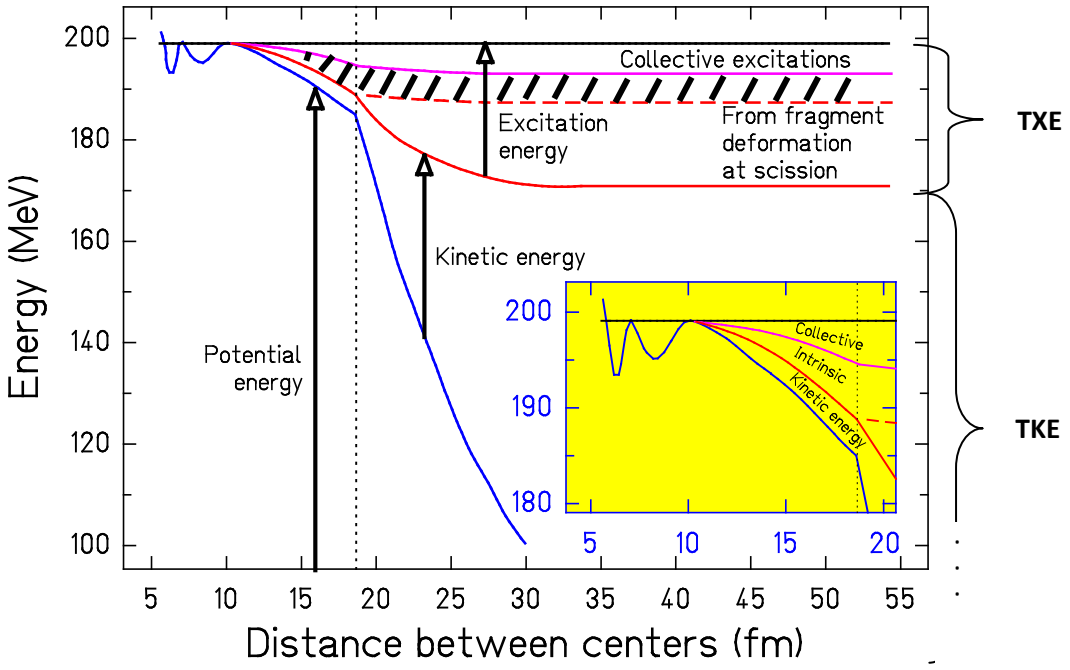

Figure 3: Schematic presentation of the different energies appearing in the fission process of ^{236}U with an initial excitation energy equal to the fission-barrier height. The vertical dotted line indicates the scission point. The arrows indicate the amount of potential energy, kinetic energy and excitation energy. The inset illustrates the region before scission in an enlarged scale. The values of the different energy contributions have been obtained with the GEF code [Sch14]. The hatched area is the total intrinsic excitation energy available before scission. TXE stands for Total eXcitation Energy and TKE for Total Kinetic Energy.

Different mechanisms lead to the transformation of the potential energy stored in the elongation degree of freedom into intrinsic excitation energy during the descent from saddle to scission: one-body [Sim14] and two-body dissipation due to level crossing [Mir09]. As shown in [Asg84], the potential-energy difference between saddle and scission increases with $Z_{CN}^2 / A_{CN}^{1/3}$, where Z_{CN} and A_{CN} correspond to the number of protons and the number of nucleons of the fissioning nucleus, respectively. In this work, we assume that the dissipated energy increases in proportion to this energy difference. More precisely, we consider that

about 35% of the potential energy difference from saddle to scission is dissipated. This fraction gives the best agreement between GEF and a significant amount of fission data [Sch14]. According to this, the dissipated energy (hatched area in Fig. 3) varies from about 3 MeV for ^{230}Th to 8.5 MeV for ^{250}Cf.

We have to consider also the intrinsic excitation energy above the fission barrier, which is equal to the total excitation energy of the nucleus minus the height of the outer fission barrier. In the case represented in Fig. 3, the fissioning nucleus has no excitation energy above the second barrier. Of course, if we would consider a higher incident neutron energy, the excitation energy above the barrier would be higher. This additional excitation energy has to be added to the energy that is dissipated (hatched area in Fig. 3) to obtain the total intrinsic excitation energy available before scission E_{tot}, which is the quantity of interest in this work.

The main part of Fig. 3 shows that the excitation energy of the fragments still increases after scission. The reason is that, as the fragments move apart, their mutual Coulomb repulsion decreases, the fragments become less and less deformed and the surface energy becomes available in the form of excitation energy. In addition, the energy stored in the collective normal modes (angular-momentum bearing and others) [Nix65] is shared between the fragments according to the corresponding coordinated motions of the nascent fragments before scission and appears as rotational energy in the separated fragments. Depending on the spectroscopic nature of the fragment, the angular momentum can be carried by single-particle excitations and/or by collective excitations (e.g. rotational states in deformed nuclei). E_{tot}, the deformation energy and the collective energy constitute the Total eXcitation Energy (TXE) of the fragments.

Fig. 3 also gives quantitative information on how the fission Q value (about 200 MeV) is distributed into TXE (that will be released in the form of prompt neutrons and gamma rays) and total kinetic energy (TKE), TKE = Q - TXE for the case shown in Fig. 3. We can see that only about 30 MeV become excitation energy of the fragments, the rest, about 170 MeV, become kinetic energy. In the example shown in Fig. 3, the largest contribution to the TXE comes from the deformation energy of the fragments.

The excitation energy available before scission E_{tot} has to be partitioned between the fragments before they separate at scission. In Section 3, we use statistical mechanics to investigate how this energy is distributed. We insist that the deformation and collective energies are dissipated into intrinsic excitation energy well after scission, when the fragments are not in contact anymore. These two types of energies cannot be exchanged between the fragments. Therefore, as we pointed out in Article VII, the assumption of most fission models used for the prediction of prompt-neutron emission in reactor physics [Mad82, Lem05, Ran09, Tal10, Lit10] that the total excitation energy *TXE* (see Fig. 2) is shared between the fragments according to the condition of statistical equilibrium is not correct.

2.2. Prompt-fission neutrons

The strong correlation between the excitation energy of the fragments and their deformation near scission is clearly reflected by the average number of prompt neutrons $<\nu>$ (or $\bar{\nu}$) as a function of the fragment mass. This quantity has been measured rather accurately for the spontaneous fission of ^{252}Cf and is shown in Fig. 4. We can see that the number of prompt neutrons first increases with the mass of the fragment, it suddenly drops at $A\approx130$ and increases again with the mass of the fragment. This particular shape of $<\nu>(A)$ is known in literature as the "saw tooth". The drop near A=130 is due to the spherical shape of the double-magic (Z=50, N=82) heavy fragment. The increase of $<\nu>$ with mass number can be explained by the increase of the fragment deformation. Indeed, shell-model calculations [Wil76, Rag84] reveal that shell effects at large prolate deformation show a strong correlation between the particle number (neutrons or protons) and the increasing deformation.

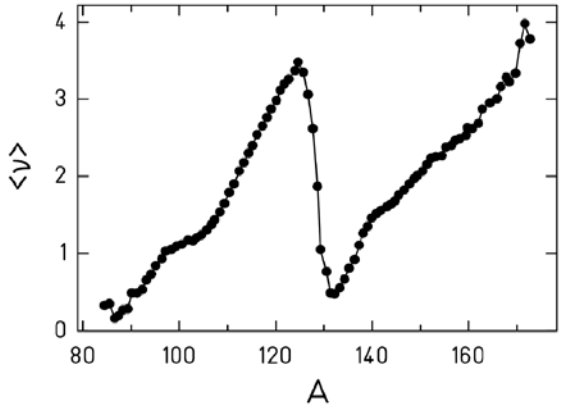

Figure 4: Measured average number of prompt neutrons as a function of the fission-fragment mass for the spontaneous fission of ^{252}Cf [Wah88].

The average number of evaporated neutrons as a function of the fragment mass of ^{237}Np has been studied very carefully at two different neutron energies [Naq86], see Fig. 5. As mentioned above, an increase of incident neutron energy translates into an increase of the intrinsic excitation energy above the barrier and, thus, into an increase of the total intrinsic excitation E_{tot} available before scission. One would expect that the increase in excitation energy would lead to an increase of the number of prompt neutrons emitted by both fragments. However, Fig. 5 shows a very peculiar feature: for asymmetric mass splits below A=110 and above A=130 the increase of intrinsic excitation energy leads to an increase of the number of evaporated neutrons for the heavy fragment, only. Actually, as shown in Article V, a quantitative analysis of the data from Fig. 5 reveals that all the additional intrinsic excitation energy appears in the heavy fragment. This observation is rather general, as it was also found for other fissioning systems such as ^{233}U and ^{238}U and other incident particles like protons [Bur70, Bis70, Mül84, Str90]. However, this effect remained unexplained for many years.

2.3. The odd-even effect in fission-fragment elemental yields

In addition to intrinsic excitation energy, the nascent fragments have also to share few unpaired nucleons before scission. The question arises in a very clear manner for odd-Z fissioning nuclei. In this case, there is, from the very beginning of the fission process, at least one unpaired proton. For even-Z fissioning nuclei, the unpaired protons can be generated during the fission process, for example if part of the potential energy stored in the elongation is dissipated into quasiparticle excitations on the way from saddle to scission.

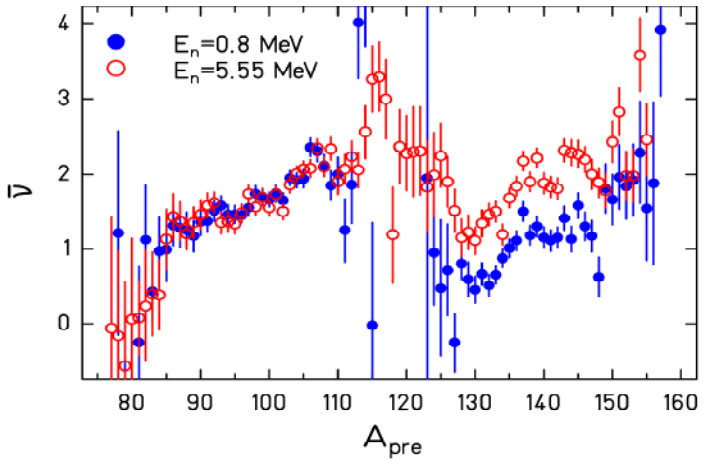

Figure 5: Average number of prompt neutrons as a function of the primary fragment mass for the neutron-induced fission of ^{237}Np at two incident neutron energies, data taken from ref. [Naq86].

Fig. 6 shows the measured fission-fragment yields as a function of proton number for the fissioning nucleus ^{229}Th. The data were measured in inverse kinematics at GSI. The ^{229}Th beam was excited in the Coulomb field of lead target atoms slightly above the fission barrier [Sch00]. The average excitation energy of the fissioning nucleus is 11 MeV, corresponding to the excitation energy induced by neutrons with 5.8 MeV kinetic energy. This inverse-kinematics experiment allowed the measurement of the odd-even structure continuously over a large range of mass splits. This was not possible in heavier actinides due to the extremely low yields for symmetric splits. The global shape of the data from Fig. 6 can be described by three humps, one centred at symmetry (Z≈45) and two at asymmetry (Z≈36 and 54). These humps result from the shape of the potential as a function of mass (or charge) asymmetry as given by the liquid-drop model with the influence of shell effects [Str68], see Fig. 2. The odd-even effect in fission-fragment yields is the fine structure that is superimposed to the gross shape of the yields showing an enhanced production of fragments with even Z. The production of odd-Z fragments evidences that pairs of nucleons are broken during the fission process.

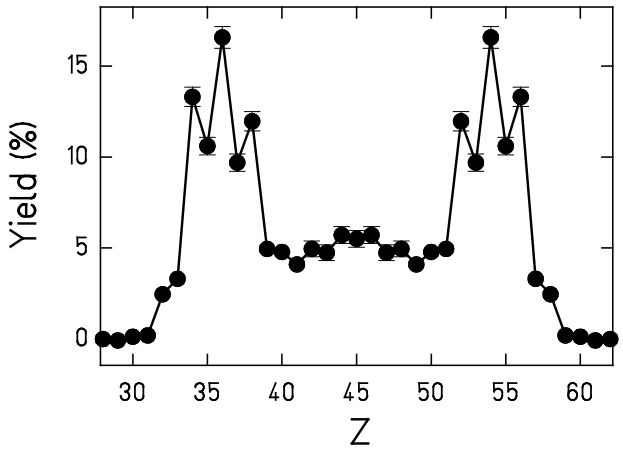

Figure 6: Element distribution observed in the electromagnetic-induced fission of ^{229}Th in inverse kinematics at GSI [Sch00].

Fig. 7 shows the fission-fragment charge distribution of the odd-Z nucleus ^{220}Ac measured also in inverse kinematics at GSI [Sch00]. We can see that for the most asymmetric splits (around Z = 32 and Z = 57) there is also an odd-even staggering and that there is a higher yield for light even-Z fragments (implying an odd-Z heavy fragment). Therefore, these data show that the unpaired proton prefers to stick to the heavy fragment.

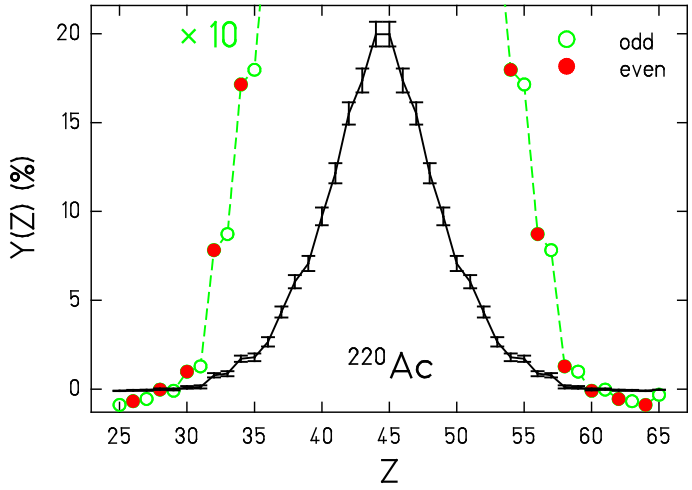

Figure 7: Element distribution observed in the electromagnetic-induced fission of ^{220}Ac [Sch00]. The green-dashed line shows the distribution multiplied by a factor 10 to highlight the yields for the most asymmetric splits.

It was proposed in [Tra72] to quantify the odd-even staggering by the local odd-even effect $\delta_p(Z)$, which corresponds to the third differences of the logarithm of the yields Y:

$$\delta_p(Z) = \frac{1}{8}(-1)^{Z_{low}}\left[lnY(Z_{low}+3) - lnY(Z_{low}) - 3\left(lnY(Z_{low}+2) - lnY(Z_{low}+1)\right)\right] \quad (1)$$

where Z_{low} is an integer defined as Z_{low}=Z - 3/2. As discussed in Article VIII, the quantity $\delta_p(Z)$ has the important advantage to filter out from the yields the variations that extend over a significant number of charges and are related to the global shape of the potential energy. To

better understand the meaning of $\delta_p(Z)$, we can consider two curves: one links the logarithms of the yields of neighbouring even-Z fragments $\ln Y_{even\ Z}(Z)$, and the other connects the logarithms of the yields of neighbouring odd-Z fragments $\ln Y_{odd\ Z}(Z)$. These two curves are continuous functions (if the yields $Y_{even\ Z}$ and $Y_{odd\ Z}$ follow a Gaussian shape, the curves are parabolas) and can be evaluated for any value of Z. As explained in [Tra72], $\delta_p(Z)$ equals half the distance between the two curves:

$$\delta_p(Z) = \frac{\ln Y_{even\ Z}(Z) - \ln Y_{odd\ Z}(Z)}{2} \tag{2}$$

Fig. 8 shows experimental results on $\delta_p(Z)$ as a function of charge asymmetry for different fissioning nuclei. In this figure, the charge asymmetry has been parameterized as the ratio of the charge of the light fragment Z_1 over the charge of the fissioning nucleus Z_{CN}. The curve named ^{229}Th,em has been obtained from the data shown in Fig. 6. The remaining data, corresponding to thermal-neutron-induced fission, have been taken from the compilation given in [Caa11]. Fig. 8 illustrates several general trends:

(i) The amplitude of δ_p decreases with increasing mass of the fissioning system and with excitation energy (cf. ^{229}Th,e.m.).

(ii) For a given fissioning nucleus δ_p increases with asymmetry.

(iii) Also odd-Z fissioning systems like ^{243}Am or ^{239}Np show an odd-even effect at large asymmetry whose magnitude is about the same as for even-Z systems of comparable mass.

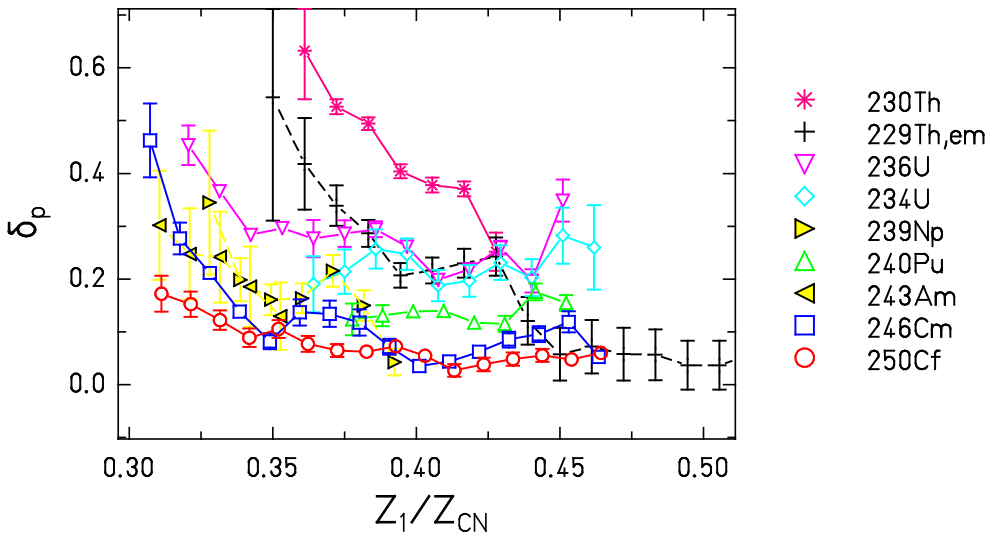

Figure 8: Measured local odd-even effect δ_p as a function of asymmetry. The legend indicates the fissioning nucleus. The data labelled ^{229}Th,em have been taken from [Sch00] and the rest from the compilation given in [Caa11].

Statistical arguments have been previously used to explain in a more or less quantitative way the different aspects of the odd-even effect in fission-fragment yields illustrated in Fig. 8 (see

Article VIII). However, a comprehensive model that explains the odd-even staggering in all its complexity is not yet available.

3. Application of statistical mechanics to two nascent fission fragments in contact

In the following, we investigate the partition of excitation energy and few nucleons between the nascent fission fragments within the frame of statistical mechanics. We have seen in Chapter 1 that statistical equilibrium represents the asymptotic state to which any system is driven to. Therefore, our approach can help to identify the main mechanisms that are behind the observations described in the two previous sections.

3.1. Starting point of the model

Theoretical investigations of the gradual transition from the mononucleus regime to the dinuclear system concerning shell effects [Mos71, Mos71-2], pairing correlations [Kra01] and congruence energy [Mye97] show that the fission-fragment properties are already rather well established in the vicinity of the outer saddle. As explained in [Mos71], the strong influence of the fragment shells on the single-particle states well before scission is due to a fundamental quantum-mechanical effect in which the nucleons are localized in the two fragments as soon as there is some necking. Very recently, Hartree-Fock calculations with BCS pairing residual interaction have been performed for ^{264}Fm in [Sim14]. These calculations confirm the very early onset of the fission fragment properties. One can see that the establishment of the shell gaps $Z = 50$ and $N = 82$ of the ^{132}Sn nascent fragments and the vanishing of the proton and neutron pairing energies occur well before the configuration where the neck disappears. Therefore, it is reasonable to assume that, well before scission, the fissioning system consists of two well-defined nuclei in contact through the neck.

The dissipated energy introduced in section 2.1 is gradually fed into the system on the way from saddle to scission, see Fig. 3. We assume that the system reaches statistical equilibrium at every point of the trajectory from saddle to scission and that the feeding of intrinsic excitation energy is faster than the relaxation time. Then, for simplicity, we can further assume that all the dissipated energy is already fed into the system at the point where the properties of the fragments are well defined. Therefore, at this point the total amount of available excitation energy E_{tot} is equal to the sum of the intrinsic excitation energy above the outer saddle and the energy acquired by dissipation from saddle to scission. Intrinsic excitations are expected to be homogeneously distributed within the nuclear volume. This is likely to hold also in the transition from a mononuclear to a dinuclear system that takes place very rapidly near the outer saddle [Mos71]. Consequently, a reasonable assumption is that E_{tot} is initially shared among the fragments according to the ratio of their masses.

We assume that the system formed by the two nuclei in contact then evolves to a state of statistical equilibrium, the macrostate of maximum entropy, where all the available microstates have equal probability to be populated, see Chapter 1. This implies that the total

available energy E_{tot} will be distributed among the two nascent fragments according to the probability distribution of the available microstates which is given by the total nuclear level density[1]. During the equilibration there is a strong restriction on the gross mass asymmetry which is fixed by the bottom of the potential in the fission valleys (see Fig. 2). This means that the number of protons and neutrons in the prefragments can only vary by very few units.

3.2. Nuclear level densities

The total nuclear level density of the system made of two fragments in contact is given by the product of the level densities of the two fragments $\rho_1(E_1)\rho_2(E_2)$. Before deepening into the equilibration process of the two fragments, it is important to have a closer look at the nuclear level densities, which are a key ingredient of our model. The experimental information on nuclear level densities is rather scarce and for a long time it has been limited to the lowest excitation energies through the counting of known, discrete levels and to excitation energies around the neutron separation energy studied by experiments on neutron resonances. Thanks to the analysis of neutron evaporation spectra in proton-induced reactions, e.g. [Svi06], and more recently, thanks to the Oslo method [Lar11], the region between the lowest excitation energies and the neutron separation energy has become accessible. These data show that for most nuclei the logarithmic slope of the level density remains nearly constant as a function of excitation energy, see Fig. 9. This is a rather peculiar behaviour and one can better understand its particularity by using the concept of temperature (a discussion on the pertinence of the use of this concept for nascent fission fragments is given below). Combining eqs. (7) and (8) of Chapter 1, we get that the temperature T corresponds to the inverse logarithmic slope of the level density:

$$T = \left[\frac{d(\ln(\rho(E))}{dE} \right]^{-1} \tag{3}$$

Therefore, the experimental results indicate that the nuclear temperature remains nearly constant when the excitation energy increases. That is, at low excitation energies nuclei behave nearly like thermostats. This recalls the behaviour of objects in nature that undergo a phase transition. During the melting of ice, the temperature remains constant until all the ice has turned into water. This occurs because the excitation energy that is put into the system is spent in the creation of new degrees of freedom. Different theoretical work (e.g. [Str58]) has shown that in nuclei the observed constant-temperature behaviour is due to the continuous melting of Cooper pairs, and recalls the superfluid-normal phase transition in some liquids [Nyh12].

[1] We replace the nuclear state density Ω introduced in Chapter 1 by the nuclear level density ρ because we neglect the degeneracy of magnetic substates, which contributes very little to the variation of the state density with excitation energy.

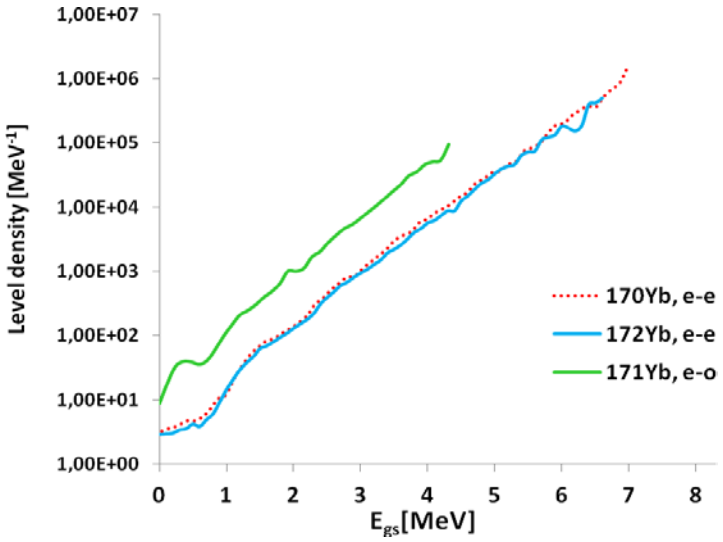

Figure 9: Experimental level densities of different Yb isotopes measured with the Oslo method [Gut01]. The excitation energy E_{gs} is measured with respect to the ground state of the different nuclei.

Pairing correlations lead to a net increase of the binding energy of the nuclear ground state and of excited states. This increase is named condensation energy. It is due to the residual interactions, which cause transitions between different single-particle configurations that preserve the total angular momentum and the parity of the nucleus. A single nucleon cannot participate in the pairing correlations, and, in addition, it blocks one of the levels, which is not available for the paired nucleons scattered by the pairing correlations. When the nucleus is excited, the energy gain by pairing correlations is gradually reduced and eventually disappears at the critical excitation energy. The reason is that with increasing excitation energy, more and more pairs are broken (quasi-particles are excited), and the two nucleons of a broken pair do not participate in the pairing correlations and block two additional levels. Empirical information on the critical energy has been extracted from the analysis of fission probabilities [Ign75] and of the fission angular anisotropy in low-energy fission [Ign82], where values around 10 MeV have been deduced.

The nuclear level density is also affected by shell effects and collective enhancement due to the vibrations and rotations built on top of the ground state and each single-particle state (see Chapter 2). Both effects vanish at high excitation energies. Therefore, at sufficiently high excitation energies, the nuclear level density is expected to follow the Fermi-gas level density formula, derived by Bethe [Bet36] assuming that the nucleus behaves like a gas of non interacting fermions with equidistant single-particle levels around the Fermi energy.

Given the limited experimental information on level densities, one is obliged to use model predictions or semi-empirical analytical formulas. We have made an effort to use in our model level densities that are consistent with the experimental observations and with our present understanding of nuclear properties. In Article VIII, we investigated the influence of pairing correlations on the level densities and performed a critical analysis of two empirical

parameterisations that are widely used in technical applications: The back-shifted Fermi-gas and the composite Gilbert and Cameron level-density formulas.

The expression for the back-shifted Fermi-gas level density is:

$$\rho_{FG}(U) = \frac{\sqrt{\pi}}{12} \frac{\exp\left(2\sqrt{aU}\right)}{a^{1/4}U^{5/4}} \tag{4}$$

With $U = E_{gs} - \Delta_0$ and E_{gs} being the excitation energy of the nucleus with respect to its ground state. Eq. (4) takes its origin from the level density derived by Bethe but includes an energy shift Δ_0. The parameters Δ_0 and a in eq. (4) are deduced from fits to experimental data. Even if the back-shifted Fermi-gas formula may appear to give good descriptions for the level densities of certain nuclei [Tof10], it has several important drawbacks. First of all, the use of the Fermi-gas formula, which is only valid in the independent-particle picture, in an energy range where pairing correlations are present is a severe inconsistency. In addition, this formula does not reflect the expected change in the slope of the level-density curve at the critical pairing energy. In most formulations of the back-shifted Fermi-gas model, the value of the energy shift Δ_0 is close to zero for odd-*A* nuclei, positive for even-even and negative for odd-odd nuclei. However, Δ_0 has a physical meaning: it accounts for the displacement of the ground state due to the condensation energy. Therefore, according to the back-shifted Fermi-gas model, pairing correlations tend to increase the binding energy of even-even nuclei, have little effect on the binding energy of odd-*A* nuclei and reduce the binding of odd-odd nuclei. This is in conflict with observations, which indicate the presence of pairing correlations in essentially all nuclei (may be with the exception of a few doubly magic nuclei).

The composite Gilbert-Cameron level-density formula [Gil65] is composed of a constant-temperature formula below a matching energy followed by a Fermi-gas formula with an energy shift. The constant-temperature part follows the expression:

$$\rho_{CT}(E_{gs}) = \frac{1}{T}\exp\left(\frac{E_{gs} - E_0}{T}\right) \tag{5}$$

where the nuclear temperature T and E_0 are parameters that serve to adjust the formula to the experimental data. According to the experimental systematics from ref. [Egi05], T decreases with the mass of the nucleus as $T = 17.45/A^{2/3}$. The matching energies are derived from purely mathematical arguments to ensure that the slopes and the absolute values of the two functions are the same. They vary between approximately 5 and 7 MeV. The Gilbert-Cameron formula has the positive feature that it includes the expected transition from the constant-temperature to the Fermi-gas regime with increasing energy. However, this transition occurs at energies given by the matching energies, which are too low, well below the critical pairing energy.

There exist different parameterisations of the composite Gilbert-Cameron formula. In the one proposed in RIPL-3 [Cap09], the energy shift of the Fermi-gas description is zero for odd-odd nuclei, equal to the pairing-gap parameter Δ ($\Delta \approx 12/\sqrt{A}$) for odd-mass nuclei and 2Δ for even-even nuclei. This means that the binding energy of odd-odd nuclei is not increased by pairing correlations, thus suggesting that there is no pairing in odd-odd nuclei. Since the first excited quasi-particle state in even-even nuclei has the same number of unpaired particles as an odd-odd nucleus in its ground state, one would also expect that pairing disappears at the first excited quasi-particle state in even-even nuclei. This is again in severe conflict with the presence of pairing correlations in essentially all nuclei, even at moderate excitation energies, with the eventual exception of a few doubly magic nuclei.

To cope with these problems, in Article VIII we have proposed a modified version of the Gilbert-Cameron formula in which we increase the energy shift of the Fermi-gas part by about 2 MeV, i.e. we use an energy shift $\Delta_{cond} = \Delta + 2$ MeV. This increased value of the energy shift leads to a higher matching energy for the transition from the constant temperature to the Fermi-gas regime that is much closer to the expected value of the critical energy of about 10 MeV. In addition, it leads to an increase of the level density in the Fermi-gas regime of a factor 50, which is in agreement with the expected effect of collective enhancement. Our modified composite formula (whose details are given in page 30 of [sch14]) is used in the GEF code and is essential for obtaining a good reproduction of for example the prompt-fission neutron spectra [Sch14], which are particularly sensitive to the level densities of the fragments.

In Fig. 9, we see that the level density of the even-odd ^{171}Yb is higher than the level density of the even-even ^{170,172}Yb nuclei due to the presence of an unpaired neutron in ^{171}Yb. Strutrinsky showed [Str58] that if we give an even-even nucleus an extra energy equal to the energy needed to break a pair of neutrons, it will have the same level density as the corresponding neighbouring nucleus with an odd number of neutrons. This theoretical expectation has been confirmed with experimental data in e.g. [Gai91, Gut00]. As discussed in [Gut00], the experimental level density of the even-odd ^{171}Yb can be expressed as the level density of the even-even ^{170}Yb or ^{172}Yb nuclei with an energy shift that is equal to the pairing gap parameter Δ, i.e. $\rho_{eo}=\rho_{ee}(E_{gs}+\Delta)$. This fundamental property of the nuclear level densities of neighbouring nuclei plays a crucial role in our model.

3.2.1. Level densities of nascent fission fragments

In Article IX we have discussed the adequacy of using the level-density formulae described above, in a situation before scission where the touching fragments are strongly deformed due to their mutual Coulomb repulsion. From a macroscopic point of view, the use of ground-state level-densities at significantly larger deformations is well justified because the level density parameter a of the Fermi-gas formula and the temperature parameter T of the constant-temperature formula vary very weakly with deformation. However, shell effects can have a significant impact on the level-density parameter a and on the temperature parameter T. The shell effects at large deformation are generally weaker than shell effects at ground-state

deformation. In addition, the magnitude with which the effect of the shell closure manifests depends on the relative yield of the different fission channels and this makes the inclusion of shell effects into the problem rather complicated. Finally, the amount and the quality of the experimental data are still too limited to be sensitive to the influence of shell effects on the equilibration process of the two nascent fragments. For all these reasons, in our model we have not considered shell effects on the level densities.

The fact that we neglect the effect of the Coulomb repulsion between the fragments implies that we neglect the interaction term H_{12} of the Hamiltonian of the global system given in eq. (12) of Chapter 1. In other words, we assume that the coupling between the two fragments is weak and we can use eqs. (13) and (14) of Chapter1.

3.3. Partition of intrinsic excitation energy according to statistical equilibrium : excitation-energy sorting

We now want to investigate how two warm nuclei in thermal contact share the total available intrinsic excitation energy E_{tot} according to statistical mechanics. To get an intuitive view of the equilibration process we will first use again the concept of temperature. Since the level densities of the fragments have a rather constant logarithmic slope, applying eq. (3) we get that the temperatures T_1, T_2 of the fragments are nearly constant. The temperature of the heavy fragment T_2 being lower than the temperature of the light fragment T_1. In normal experience, when two objects with different temperatures are set in contact, the heat flows from the hotter to the colder system until thermal equilibrium is reached where both objects have same temperature. The equilibration of temperatures cannot be achieved for two nascent fission fragments at low excitation energies. The energy will flow from the hot (light) to the cold (heavy) fragment, but, in the constant-temperature regime, the variations of the excitation energy do not lead to variations of the temperatures. In this regime, there is no solution for the division of intrinsic excitation energy with $T_1 = T_2$. Therefore, the excitation energy will continue flowing from the light to the heavy fragment until the excitation energy in the light fragment is practically exhausted. This process is what we call excitation energy sorting, and was first introduced in Article V.

Using eq. (11) of Chapter 1 we can determine the entropy of the system made of two fragments in contact at equilibrium:

$$S = S_1 + S_2 = \frac{E_1}{T_1} + \frac{E_2}{T_2} = \frac{E_1}{T_1} + \frac{E_{tot} - E_1}{T_2} = \frac{T_1 E_{tot} + (T_2 - T_1)E_1}{T_1 T_2} \qquad (6)$$

It is easy to see from eq. (6) that if $T_1 > T_2$ the entropy is maximum when E_1=0 and, consequently, E_2=E_{tot}. Therefore, the process of energy sorting is driven by entropy.

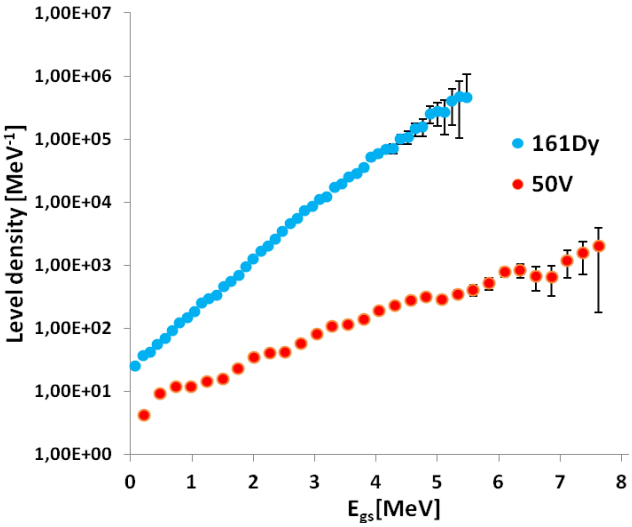

Figure 10: Experimental level densities of ^{50}V[Lar06] and ^{161}Dy[Gut03] obtained with the Oslo method. The excitation energy E_{gs} is measured with respect to the ground state of the nuclei.

As described in Article VII, the rigorous solution to the problem within the frame of statistical mechanics is obtained by calculating the average excitation energy of the fragments under the assumption of statistical equilibrium. Using eq. (14) of Chapter 1, we get that the average excitation energy of the light fragment at equilibrium is given by:

$$< E_1 >= \frac{\int_0^{E_{tot}} E_1 \rho_1(E_1)\rho_2(E_{tot}-E_1)dE_1 \Delta E_{tot}}{\int_0^{E_{tot}} \rho_1(E_1)\rho_2(E_{tot}-E_1)dE_1 \Delta E_{tot}} = \frac{\int_0^{E_{tot}} E_1 \rho_1(E_1)\rho_2(E_{tot}-E_1)dE_1}{\int_0^{E_{tot}} \rho_1(E_1)\rho_2(E_{tot}-E_1)dE_1} \quad (7)$$

Here, ΔE_{tot} represents the uncertainty in the total intrinsic excitation energy, which is a constant and cancels out in the ratio. Fig. 10 shows the experimental level densities of ^{50}V and ^{161}Dy, these two nuclei are representative of the fission fragments of a very asymmetric split. We see that both nuclei follow rather well the constant-temperature behaviour and that the logarithmic slope of the level density of the heavy fragment is much larger than the logarithmic slope of level density of the light fragment. The most probable partition of excitation energy is the one that maximises the total level density $\rho_1(E_1)\rho_2(E_2)$. Since the fragments must fulfil the condition $E_{tot}=E_1+E_2$, the most probable energy partition will be the one where the heavy fragment gets all the excitation energy $E_2 \approx E_{tot}$ and the light fragment is cold $E_1 \approx 0$.

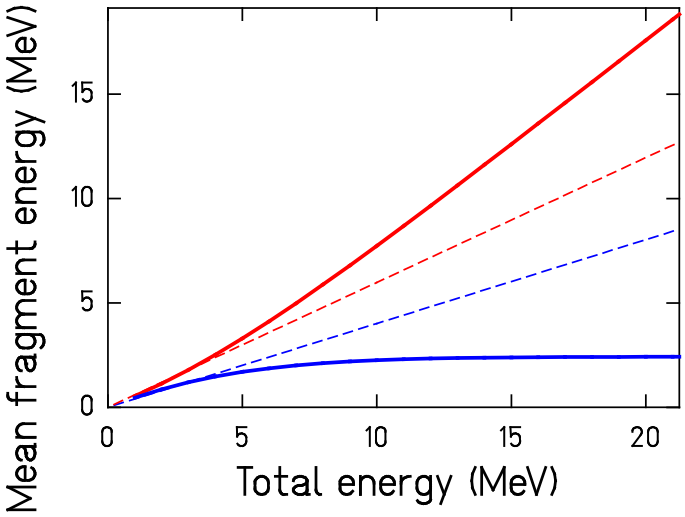

Figure 11: Mean excitation energies at equilibrium of the nuclei ^{94}Sr (lower lines) and ^{140}Xe (upper lines) in thermal contact as a function of the total intrinsic excitation energy. The full lines were obtained with level densities described by the constant-temperature formula. The temperature parameters of the two level densities were obtained from the empirical parameterization of Ref. [Egi05]. The dashed lines denote the partition according to the mass ratio.

Let us now consider the case of the two complementary fragments ^{94}Sr and ^{140}Xe, which are produced with high yields in the thermal-neutron-induced fission of ^{233}U. If we assume that the nuclear level densities of the two fragments follow the constant-temperature behavior for all possible total excitation energies, application of eq. (7) gives the result represented by the solid lines in Fig. 11. The dashed lines in Fig. 11 correspond to the solution that would result from using the Fermi-gas description for the level densities. In this latter case, the excitation energy is partitioned in proportion to the mass ratio of the fragments. The solid lines in Fig. 11 show that, in contrast to the result described at the beginning of this section where the light fragment exhausts all its excitation energy, the excitation-energy of the light fragment follows approximately the mass ratio up to a total intrinsic excitation energy of about 4 MeV. However, at higher total excitation energies the excitation energy of the light fragment levels off and remains at about 2 MeV. From this point on, practically all additional excitation energy ends up in the heavy fragment. Thus, for the considered mass split total intrinsic excitation energies in excess of about 4 MeV are subject to energy sorting.

The process of energy sorting explains in a transparent way the surprising observation illustrated in Fig. 5 on the dependence of $<\nu>(A)$ with the incident neutron energy. The dissipated excitation energy from saddle to scission of ^{238}Np is about 6 MeV. Therefore, energy sorting applies and easily explains why the increase of incident neutron energy by about 4.7 MeV leads to an increase of the number of neutrons emitted by the heavy fragment only. Article VII discusses also the situation in which the level density follows the composite Gilbert Cameron level-density formula given in RIPL3 [Cap09]. As shown in Fig. 4 of Article VII, energy sorting does not stop sharply at the matching energies (5 -7 MeV), but its effect is

still appreciable at total intrinsic excitation energies that are significantly above the matching energies.

3.4. Partition of unpaired nucleons according to statistical equilibrium: the odd-even effect and complete energy sorting

As we mentioned already, unpaired nucleons may be transferred from one fragment to the other. However, the net transfer of nucleons can only be limited to few nucleons because the mass of the fragments is tightly fixed by the valleys of the potential energy surface, which set in already near the second barrier, as shown in Fig. 2. In contrast, nucleon exchange between the fragments (i.e. the transfer of one nucleon from fragment 1 to fragment 2, plus the transfer of one nucleon from fragment 2 to fragment 1) is not constrained because it does not modify the mass of the fragments. We will show in section 3.5 that nucleon exchange is the main mechanism for the transfer of excitation energy between the fragments. In this section, we consider the net transfer of nucleons between the fragments within the frame of statistical mechanics, i.e. assuming statistical equilibrium. This was investigated in Article IX, where our model was used to derive the local odd-even effect.

To obtain the probability of populating a given configuration for Z and N at statistical equilibrium and derive the local odd-even effect δ_p (eq. 2) we need to define a unique total energy (consisting of intrinsic, collective and pre-scission kinetic energy, as well as potential energy) for all the possible fission-fragment mass and charge splits. As shown in Chapter 1, a fixed total energy is the reasonable common condition for all the systems belonging to the microcanonical ensemble. In other words, we have to use one and the same origin of the energy scale for all the fragments. This common origin has to be used for all type of energies (intrinsic, collective, etc), independently of their nature. This means that, for our present purpose, the excitation energy cannot be measured with respect to the ground state of each nucleus, as is done in Figs. 9 and 10. We may take as the origin for the energy scale the zero binding energy. However, this is not appropriate, because the application of statistical equilibrium would lead to the determination of the fragment yields, including the slowly-varying components that are filtered out by the quantity δ_p. We need a scale for the level densities where these effects are filtered out as well. As illustrated when discussing the meaning of δ_p in section 2.3, we can consider a smooth surface (in the neutron number N and Z space) that connects the yields of odd-odd fragments. This surface can be associated with the potential energy in the fission valley for the formation of odd-odd pre-fragments in the case of an even-even fissioning nucleus. The potential surface of odd-mass pre-fragments is at an energy $-\Delta$ (Δ being the corresponding pairing gap) with respect to the surface of odd-odd pre-fragments, and the potential surface of even-even pre-fragments is at an energy of -2Δ. Thus, the required filtering of the level densities can be obtained by placing the level densities of the nascent fragments in a reduced energy scale $U = E_{gs}-n\Delta$ where the excitation energies above the ground state E_{gs} of even-even fragments are lowered by 2Δ ($n = 2$), those of odd-mass fragments by Δ ($n = 1$) and are left unchanged for odd-odd fragments ($n = 0$).

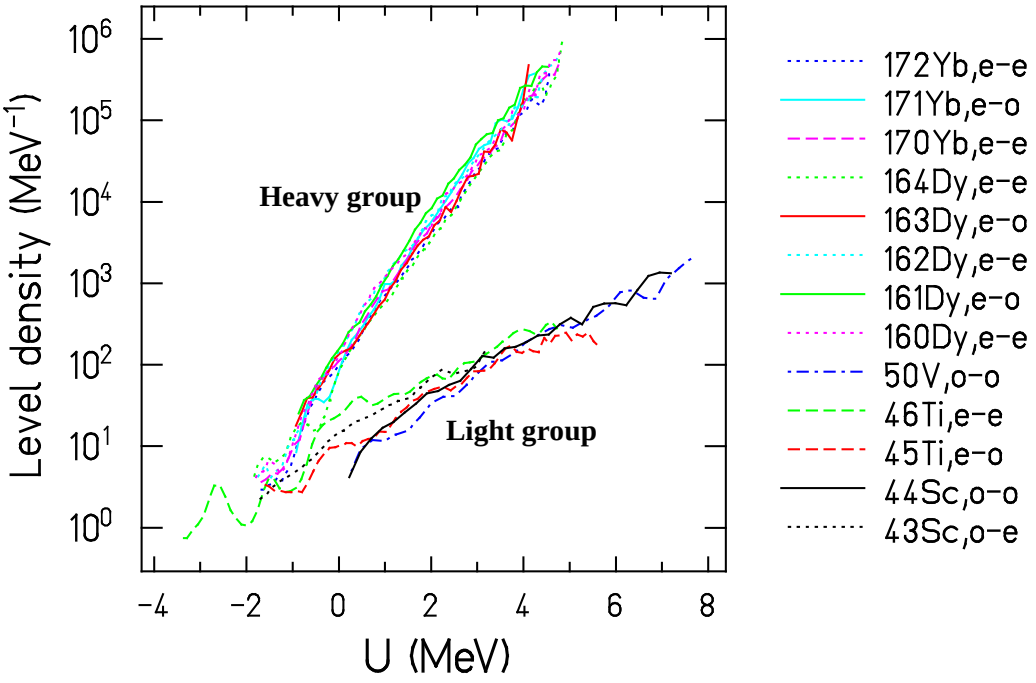

Figure 12: Experimental level densities of various nuclei [Gut03, Sch01, Agv04, Bür12, Lar07, Sye09, Gut11, Lar06] in a reduced excitation-energy scale $U = E_{gs}-n\Delta$. The excitation energy above the ground state E_{gs} is reduced by 2Δ (n = 2) for even-even (e-e) nuclei, by Δ (n = 1) for even-odd (e-o) or odd-even (o-e) nuclei and left unchanged (n = 0) for odd-odd (o-o) nuclei.

In Fig. 12, we have applied the reduced energy scale to experimental level densities determined by the Oslo method of various nuclei located around A=165 and 45. We can see that, in this scale, the level densities converge into two groups, which is a consequence of the property of the level densities of neighbouring nuclei discussed in section 3.2. Within the heavy-mass group, the level densities of neighbouring even-even and even-odd nuclei are almost identical. Sizeable differences appear only in the energy interval $-2\Delta_2<U_2<-\Delta_2$, where only even-even nuclei have states. For the light-mass group, the level densities converge well at positive reduced energies. Some fluctuations are present at negative reduced energies due to the melting of Cooper pairs. These two groups of experimental level densities represent the level densities of touching fission fragments corresponding to very asymmetric splits. Similarly to Fig. 10, Fig. 12 clearly shows that the logarithmic slope of the level densities is nearly constant and that the logarithmic slope of the heavy group is much larger than the one of the light group.

In statistical equilibrium, the total amount of possible configurations (or microstates) with particular values of Z_1 and Z_2 is directly related to the integral of the total level density for that particular split over the excitation energy of one fragment U_i, with the condition that $U_1+U_2=U_{tot}$, U_{tot} being the total available excitation energy. This integral reflects the freedom of the system in the division of excitation energy discussed in the previous section. Note that U_1, U_2, and U_{tot} are defined in the reduced energy scale, relative to the potential surface of odd-odd nuclei. The most probable configuration is the one that provides the highest total

level density $\rho_1(U_1)\rho_2(U_2)$. If all the excitation energy and unpaired nucleons are transferred to the heavy fragment to form an even-even light fragment in the ground state, the excitation energy in the heavy fragment increases to $U_2=U_{tot}+2\Delta_1$, which for the nuclei considered in Fig. 12 corresponds to an increase of the level density of the heavy fragment of more than three orders of magnitude, while $U_1=-2\Delta_1$. It becomes clear that configurations of two fragments in contact where the light fragment is fully paired (i.e. it has no quasi-particle excitations) are strongly favoured for very asymmetric fission.

Quantitatively, for an even-even fissioning nucleus, the number of configurations with Z_1 even is given by:

$$N^{ee}_{even\ Z_1}(Z_1) = \int_{-2\Delta_1}^{U_{tot}+2\Delta_2} \rho_1(U_1)_{(ee)}\,\rho_2(U_{tot}-U_1)_{(ee)}\,dU_1 + \int_{-\Delta_1}^{U_{tot}+\Delta_2} \rho_1(U_1)_{(eo)}\,\rho_2(U_{tot}-U_1)_{(eo)}\,dU_1 \tag{8}$$

where $\rho_i(U_i)_{(ee)}$ and $\rho_i(U_i)_{(eo)}$ are the level densities of representative even-even and even-odd nuclei, respectively, with mass close to A_1 or A_2. The number of configurations with Z_1 odd is:

$$N^{ee}_{odd\ Z_1}(Z_1) = \int_{-\Delta_1}^{U_{tot}+\Delta_2} \rho_1(U_1)_{(oe)}\,\rho_2(U_{tot}-U_1)_{(oe)}\,dU_1 + \int_{0}^{U_{tot}} \rho_1(U_1)_{(oo)}\,\rho_2(U_{tot}-U_1)_{(oo)}\,dU_1 \tag{9}$$

where $\rho_i(U_i)_{(oe)}$ and $\rho_i(U_i)_{(oo)}$ are the level densities of representative odd-even and odd-odd nuclei, respectively, with mass close to A_1 or A_2. The yield for even-Z_1 nuclei is :

$$Y^{ee}_{even\ Z_1}(Z_1) = \frac{N^{ee}_{even\ Z_1}(Z_1)}{N^{ee}_{even\ Z_1}(Z_1) + N^{ee}_{odd\ Z_1}(Z_1)} \tag{10}$$

By calculating $Y^{ee}_{odd\ Z_1}(Z_1)$ and applying eq. (2) we can deduce δ_p.

In a similar way, for an odd-even fissioning nucleus, we have:

$$N^{oe}_{even\ Z_1}(Z_1) = \int_{-2\Delta_1}^{U_{tot}+\Delta_2} \rho_1(U_1)_{(ee)}\,\rho_2(U_{tot}-U_1)_{(oe)}\,dU_1 + \int_{-\Delta_1}^{U_{tot}} \rho_1(U_1)_{(eo)}\,\rho_2(U_{tot}-U_1)_{(oo)}\,dU_1 \tag{11}$$

$$N^{oe}_{odd\ Z_1}(Z_1) = \int_{-\Delta_1}^{U_{tot}+2\Delta_2} \rho_1(U_1)_{(oe)}\,\rho_2(U_{tot}-U_1)_{(ee)}\,dU_1 + \int_{0}^{U_{tot}+\Delta_2} \rho_1(U_1)_{(oo)}\,\rho_2(U_{tot}-U_1)_{(eo)}\,dU_1 \tag{12}$$

Similar equations hold for even-odd and odd-odd fissioning systems. In the reduced energy scale used in eqs. (8-9 and 11-12), the level densities of neighbouring even-even, odd-A and odd-odd nuclei are very similar for positive reduced excitation energies (see Fig. 12). Therefore, the difference between the number of configurations $N_{even\ Z_1}$ and $N_{odd\ Z_1}$ is essentially given by the integrals over U_1 = -2Δ_1 to 0 and over U_1 = U_{tot} to U_{tot} + 2Δ_2. This shows that only the population of the energy states below the pairing gap of even-even nascent fragments (light or heavy) is responsible for the odd-even effect in fission. This happens when the excitation energy U_{tot} and all the unpaired nucleons (protons and neutrons) are in the complementary fragment. At asymmetry, due to the higher level density of the

heavy fragment, the main contribution to the odd-even effect comes from the configurations where the light fragment is fully paired.

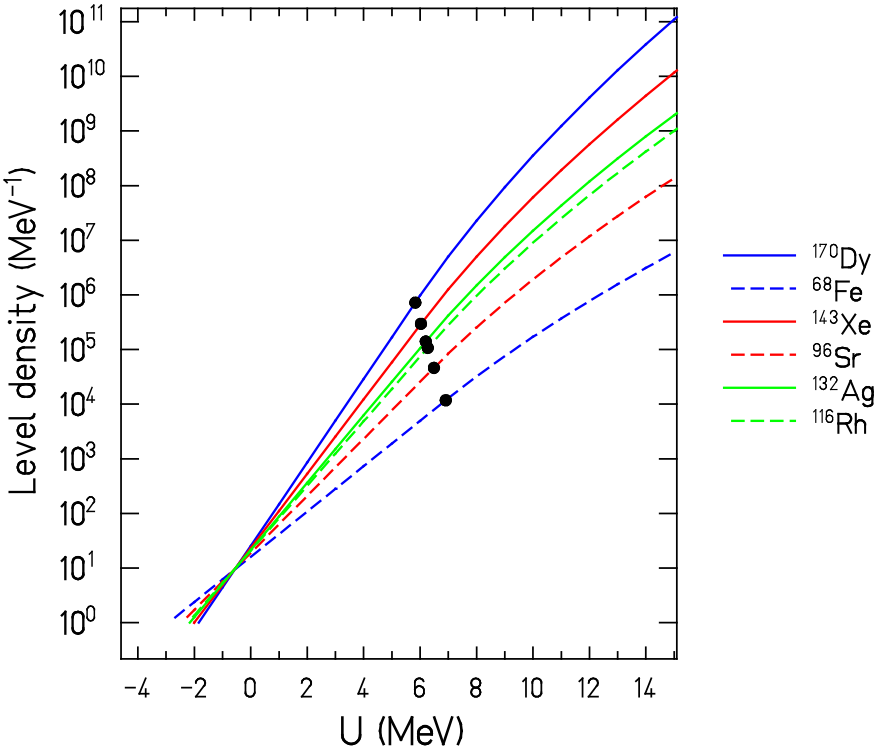

Figure 13: Level densities in an energy scale E_{gs}-$n\Delta$. The curves were obtained using the modified composite level-density formula of Article VIII. The level densities of complementary fission fragments are represented with the same colour. The full dots indicate the excitation energies where the transition from the constant-temperature to the Fermi-gas regime occurs.

In practice one cannot always find experimental level densities representative of even-even, odd-A or odd-odd nuclei for each value of Z_1 and Z_2 covered by the fission yields. However, given the similarity between the experimental level densities of neighbouring nuclei in the reduced energy scale, we have replaced in eqs. (8-9, 11-12) the representative level densities by the level densities ρ_i of the two fission fragments considered, namely A_1, Z_1 and A_2, Z_2. The level densities ρ_i are obtained using our modified composite formula, described in section 3.2. Fig. 13 shows the level densities used in our calculations for various nuclei. As the splits become more asymmetric, the difference between the logarithmic slopes of the level densities of the two complementary fragments increases. Therefore, the probability to populate the lowest-energy states of even-even or even-odd emerging light fragments increases, leading to an increase of δ_p with increasing asymmetry. Fig. 13 also illustrates that the logarithmic slope of the Fermi-gas part of the level density gradually decreases with increasing excitation energy. This implies that the relative statistical weight of configurations with a fully-paired light fragment will be less important than in the constant-temperature regime. Thus, the transition from the constant-temperature to the Fermi-gas regime that may occur when U_{tot}

increases will lead to a considerable decrease of δ_p. This explains why δ_p decreases with increasing mass of the fissioning nucleus.

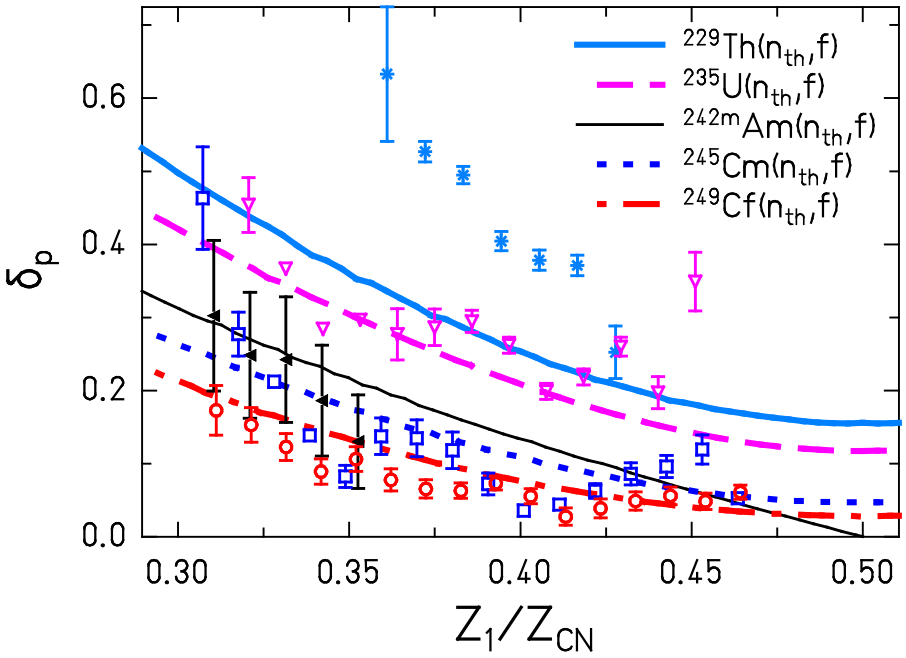

Figure 14: Local even-odd effect δ_p as a function of asymmetry. The symbols represent experimental data from the compilation of [Caa11] and denote the target nuclei: ^{229}Th (stars), ^{235}U (open triangles), ^{242}Am (full triangles), ^{245}Cm (open squares), ^{249}Cf (open circles). The lines correspond to the results of the model developed in this work.

The results of our calculation are compared with experimental data in Fig. 14. The increase of δ_p with asymmetry and the decrease of δ_p with increasing mass of the fissioning nucleus are fairly well reproduced. Only for ^{230}Th the measured values are substantially underestimated by the model. For ^{236}U, the data point that is closest to symmetry is appreciably higher than the calculation. This effect may be associated to the influence of the Z=50 shell in the complementary fragment, which is known to enhance the yield of tin isotopes. Similarly, the most asymmetric data point of ^{246}Cm is exceptionally high, which may be due to the influence of the Z=28 shell. Our calculation is also in good agreement with the data for the odd-Z fissioning nucleus ^{243}Am, which shows an odd-even effect of similar magnitude as even-Z fissioning nuclei of comparable mass. This is particularly interesting and clearly demonstrates the strong influence of complete energy sorting (i.e. the formation of an even-even light fragment with no quasiparticle excitations) on the odd-even effect in fission. Indeed, an important contribution to the odd-even effect from heavy fragments with a fully paired proton configuration would enhance the odd-even effect for even-Z fissioning systems and reduce the odd-even effect for odd-Z fissioning systems, leading to an odd-even effect of different magnitude for the two types of fissioning nuclei. Our calculation gives a zero local odd-even effect at symmetry for ^{243}Am. There is no experimental data at symmetry for this nucleus, but the electromagnetic-induced data measured in inverse kinematics at GSI confirms that there is no local odd-even effect at symmetry for odd-Z fissioning nuclei [Ste98].

When U_{tot} is small, as is the case for ^{230}Th, δ_p varies very rapidly with U_{tot}. Therefore, ^{230}Th is particularly sensitive to the uncertainties on the dissipated energy. The disagreement found for ^{230}Th may be caused by the neglect of fluctuations in the dissipated energy. In fact, for a great part of the fission events the available energy may be so low that they reach the scission point in a completely paired configuration due to the threshold character of the first quasi-particle excitation.

From a dynamical point of view, the time to form a fully-paired light nascent fragment is the sum of the time needed for the light fragment to transfer its energy to the heavier one, and the time to transfer few unpaired nucleons through the neck. If this time is longer than the saddle-to-scission time, our model will over predict the magnitude of the odd-even effect. Therefore, the general agreement between the experimental data and our calculation suggests that the time for the population of a fully-paired light fragment in accordance with statistical equilibrium is shorter than the saddle-to-scission time. It would be interesting to investigate whether microscopic models can confirm this finding.

In our approach, we have considered a given fixed total excitation energy. The inclusion of an excitation-energy distribution and of a decrease of the available excitation energy with the asymmetry of the mass split, discussed in [Möl14], can easily be done if the necessary information is available from some theoretical estimation. However, the general good agreement found between our calculations and most of the experimental data indicates that these additional effects might only have a weak impact, although they can help to improve our results for ^{230}Th.

3.5. Microscopic view of the energy transfer between two nascent fragments in contact

In Article VI, we have shown that the transfer of excitation energy between the nascent fragments may be performed by the exchange of nucleons across the neck. To understand this, we assume a simplified situation in which we consider the fragments as systems with non-interacting nucleons that follow an occupation probability as a function of single-particle energy ε given by the Fermi-Dirac distribution:

$$P_p(\varepsilon) = \frac{1}{\exp(\frac{\varepsilon}{T}) + 1} \tag{13}$$

where ε is counted with respect to the Fermi level (which corresponds to the chemical potential at zero temperature). The occupation functions of the two nascent fragments are shown in Fig. 15.

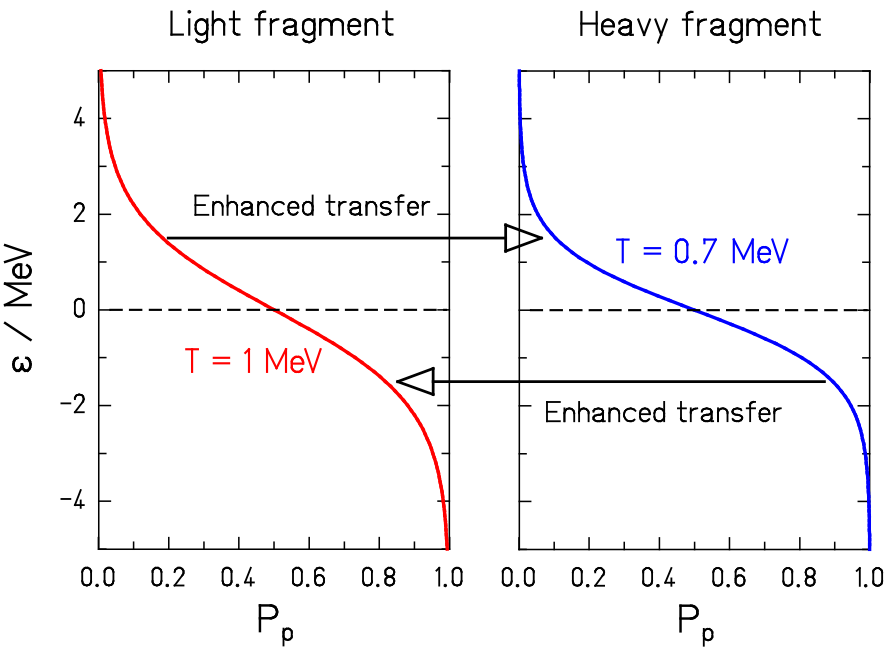

Figure 15: Fermi-Dirac single-particle occupation probabilities P_p of the two nascent fragments in the pre-scission configuration. ε is the single-particle energy with respect to the Fermi level.

The different temperatures of the fragments lead to different slopes that cause an enhanced transfer of particles from the heavy to the light fragment below the Fermi surface, and an enhanced transfer of particles from the light to the heavy fragment above the Fermi surface. Since the excitation energy is given by the sum of particle and hole energies with respect to the Fermi energy, both processes lead to a transport of excitation energy from the light to the heavy fragment. Note that the Fermi levels of the two fragments are the same, because there is no net mass transfer, since the positions of the fission valleys in terms of mass asymmetry are stable, once the fragment shells are established slightly beyond the outer saddle. In this simple case, we can calculate analytically the probability of energy transfer by one nucleon transfer from fragment 1 with T_1 to fragment 2 with T_2. This is given by the product of the probability P_{p1} of having a nucleon in fragment 1 and the probability of having a hole $(1\text{-}P_{p2})$ in fragment 2 at a given energy ε:

$$P_{12}(\varepsilon) = P_{p1}(\varepsilon) \cdot (1\text{-}P_{p2}(\varepsilon)) \tag{14}$$

The probability of energy transfer by one nucleon transfer from nucleus 2 to nucleus 1 is given in an analogous way. Fig. 16 shows the two distributions of the energy transferred by these two processes for T_1=1 MeV and T_2=0.7 MeV. On the average, the transfer of nucleons in either direction transports excitation energy from the hotter to the colder nucleus. The mean energy transported by the transfer of one nucleon is about 0.48 MeV in the case of the given example.

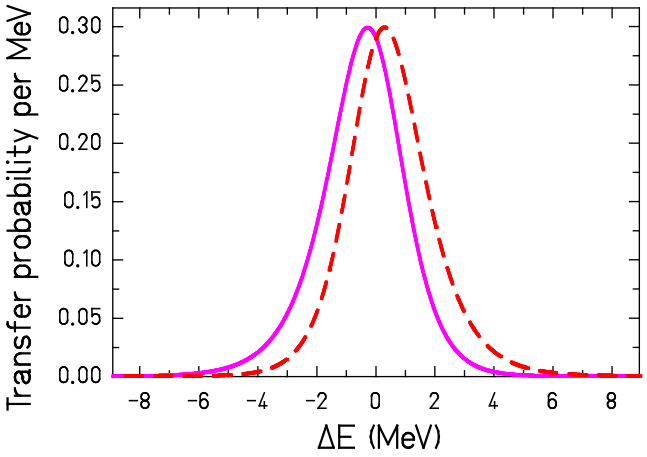

Figure 16: Probability function for energy transfer ΔE between two nuclei with T_1 = 1 MeV and T_2 = 0.7 MeV in thermal contact by the transfer of one nucleon. Full line: change of excitation energy ΔE_1 of the first nucleus by the transfer of one nucleon from the first to the second nucleus. Dashed line: change of excitation energy ΔE_2 of the second nucleus by the transfer of one nucleon from the second to the first nucleus.

By randomly sampling from the distributions shown in Fig. 16 we can obtain the probability distribution of excitation energy transfer due to one nucleon exchange, i.e. transfer of a nucleon from fragment 1 to fragment 2 plus transfer of a nucleon from fragment 2 to fragment 1. The distribution in shown in Fig. 17. The mean energy transferred by one nucleon exchange amounts to 0.96 MeV and the standard deviation of the energy-transfer distribution amounts to 3.0 MeV for the given example. Similar numerical calculations with different temperatures showed that in one nucleon-exchange the mean energy transfer is generally in the order of $3\cdot(T_1 - T_2)$ and that the standard deviation is in the order of $2\cdot(T_1 + T_2)$. These two results make sense. Indeed, we know from every-day life that the rate of heat transfer increases with the "thermal pressure" or the temperature difference between the two bodies set in contact. In addition, the standard deviation of the distribution of energy transfer is connected to the energy range of partly filled single-particle states near the Fermi level, which increases with the nucleus temperature, see Fig. 15.

The distribution in Fig. 17 shows that the transferred energy by nucleon exchange is a considerable fraction of the total excitation energy of the system. Therefore, the process of energy exchange cannot be considered as a continuous process, but it proceeds in rather large and fluctuating steps. This means that for the systems of the microcanonical ensemble the "story" of the energy transfer (i.e. the number of steps and the energy transferred in each step) will vary considerably from system to system. At the first glance, this seems to complicate the application of statistical mechanics to the di-nuclear system even more, but the contrary is true. The transfer of energy between the two nascent fragments in large, fluctuating steps causes an averaging of the properties of the two nuclei. This averaging smoothes out the fluctuations in the region where the nuclear level density is continuous but subject to fluctuations. Even more, in the region of discrete, not overlapping levels, this effect averages over the levels in a finite interval.

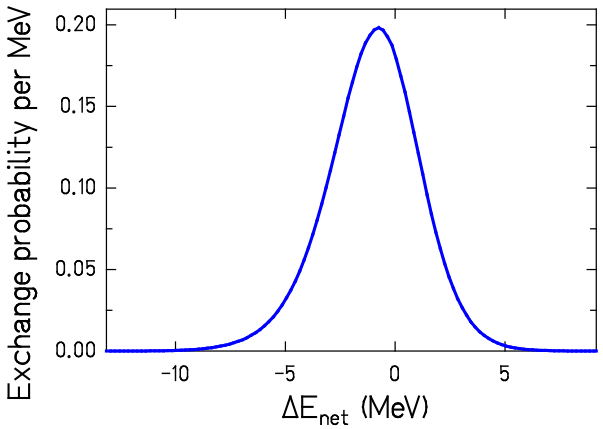

Figure 17: Probability function for net energy transfer between two nuclei in contact with T_1 = 1 MeV and T_2= 0.7 MeV by the exchange of one nucleon. The curve shows the net change ΔE_{net} of the excitation energy of the first nucleus.

The magnitude of thermal averaging is illustrated in Fig. 18, where the measured level density of ^{172}Yb is compared with the result of a smoothing procedure. As a conservative estimate, the smoothing was performed using a Gaussian function with a standard deviation equal to the average nuclear temperature T = 0.57 MeV as given by the inverse of the global logarithmic slope of the level density. Thus, the standard deviation of the smoothing function is about a factor of 4 narrower than the distribution of the individual energy-exchange values. Even with this rather weak smoothing, all the fluctuations and the structures in the measured level density around 1.2 MeV and 2.4 MeV (corresponding to the first quasi-particle excitations) are completely washed out. This result reveals that the averaging wipes out nuclear-structure effects to a large extend, thus justifying the application of the Fermi-Dirac occupation function in our schematic calculation. In addition, the thermal averaging demonstrates that the use of the smooth level-density formulae described in section 3.2. and, therefore, the definition of a nuclear temperature for two nascent fission fragments in contact is also justified.

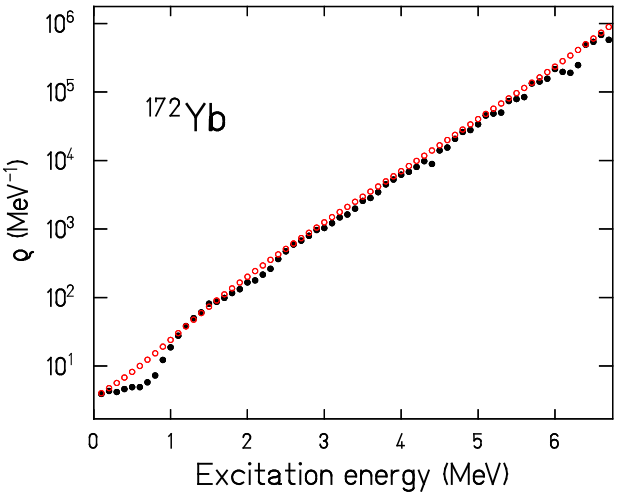

Figure 18: Measured level density [Gut01] of ^{172}Yb (full symbols) compared to the result of a smoothing procedure (open symbols). The logarithm of the level density was convoluted with a Gaussian function with a standard deviation equal to the temperature T of this nucleus.

3.6. Influence of the net transfer of few unpaired nucleons on the partition of the excitation energy

When we discussed the partition of intrinsic excitation energy in section 3.3, we did not take into account that during the relaxation process there is an exchange of nucleons and even a net transfer of few nucleons between the nascent fragments. The exchange of nucleons does not modify the number of nucleons in the fragments, but the net transfer does. Therefore, during the process of the equilibration in energy we also have to deal with different neighbouring nuclei and a common energy scale is required. As was done when we considered the partition of unpaired nucleons in section 3.4, we think it is reasonable to assume that the associated variations in the binding energy will lead to variations of the available intrinsic excitation energy only. If we neglect the impact of the slowly-varying part of the potential on the excitation energy, we can also use the reduced energy scale introduced in section 3.4 to compute the intrinsic excitation energy in the nascent fragments. Within this frame, the average excitation energy of a light even-even fragment originating from an even-even fissioning nucleus is:

$$< U_1 >^{ee}_{even-even} (Z_1, N_1) = \frac{\int_{-2\Delta_1}^{U_{tot}+2\Delta_2} U_1 \rho_1(U_1)_{(ee)} \rho_2(U_{tot} - U_1)_{(ee)} dU_1}{\int_{-2\Delta_1}^{U_{tot}+2\Delta_2} \rho_1(U_1)_{(ee)} \rho_2(U_{tot} - U_1)_{(ee)} dU_1} \quad (15)$$

We have similar equations for splits where both fragments are odd-A and odd-odd nuclei. Note that eq. (7) is the equation associated to a split where both fragments are odd-odd. Because of the different limits of the integrals, the average excitation energy $<U_1>$ for a split where both nascent fragments are even-even is higher than when both fragments are odd-A nuclei or odd-odd nuclei.

Since the nucleons are transferred during the equilibration process, the exact distribution of excitation energies in the two fragments needs to be determined with a dynamical model. Indeed, the energy equilibration of an even-even/even-even split is not always ruled by the level densities of the even-even fragments. At some point, when a nucleon is transferred, the process will be ruled by the level densities of the neighboring odd-A nuclei. Therefore, the energy distribution of the even-even/even-even split cannot adapt to the solution at statistical equilibrium given by eq. (15). The exact result will be some complex average of the solutions given by equations of the type of eq. (15). This will lead to additional fluctuations of the average excitation energy in the fragments, but will preserve the saturation of the excitation energy in the light fragment shown in Fig. 11, since this is a consequence of the constant-temperature behavior of the level densities.

4. Conclusions and perspectives

We have used statistical mechanics to investigate the equilibration of a fissioning nucleus from the point where the properties of the nascent fission fragments are well defined. We

have shown that this is fairly equivalent to considering the equilibration of two nuclei in thermal contact. The number of microstates at statistical equilibrium of the global system is obtained with nuclear level densities in which the effects of pairing correlations are consistently included. That is, the level densities follow the constant-temperature formula at low excitation energies and the Fermi-gas description at high excitation energies. The constant-temperature behaviour of the nuclear level density is at the origin of the energy sorting process, a very peculiar entropy-driven phenomenon in which the light fragment transfers its excitation energy to the heavy fragment. The energy sorting process explains in a transparent way different experimental observations that remained unexplained for decades: the neutron-energy dependence of the prompt-fission neutron yields as function of fragment mass, and the dependence of the odd-even effect in fission-fragment yields with the asymmetry of the fission fragments and the mass of the fissioning nucleus. Whereas the prompt-neutron yields demonstrate how the energy sorting determines the average excitation-energy of the two fragments, the odd-even effect reflects complete energy sorting, that is, the preferential population of the ground state of the light fragment by the transfer of all its excitation energy and unpaired nucleons to the heavy fragment.

In our model we have considered a given fixed total excitation energy proportional to the potential-energy difference from saddle to scission. One possible improvement could be the inclusion of an excitation-energy distribution that takes into account the dynamics of the evolution from saddle to scission, and a possible variation of the available excitation energy with the asymmetry of the mass split discussed in [Möl14]. This can easily be done if the necessary information is available from a theoretical estimation.

It would be highly desirable to further verify the validity of our model with additional high-quality experimental data on the mass-dependent prompt-neutron yields and on the odd-even staggering. In particular, new data spanning a broad range of asymmetry at different initial excitation energies and for a wide variety of fissioning nuclei are needed. In Chapter 4, we will show that these data can be measured at HIE-ISOLDE via transfer-induced fission experiments in inverse kinematics with short-lived pre-actinide and actinide beams.

Articles:

Article V: K.-H. Schmidt and B. Jurado, Phys. Rev. Lett. 104, 212501 (2010)
Article VI: K.-H. Schmidt and B. Jurado, Phys. Rev. C 83, 014607 (2011)
Article VII: K.-H. Schmidt and B. Jurado, Phys. Rev. C 83, 061601 (R) (2011)
Article VIII: K.-H. Schmidt and B. Jurado, Phys. Rev. C 86, 044322 (2012)
Article IX: B. Jurado and K.-H. Schmidt, J. Phys. G: Nucl. Part. Phys. 42, 055101 (2015)

Chapter 4: Medium and long-term perspectives

We have seen in Chapter 2 that the continuation of the investigation of the surrogate-reaction method depends on the availability of appropriate targets. As discussed in Chapter 2, it is nowadays rather difficult to obtain good-quality actinide targets. In addition, the targets needed for surrogate experiments are difficult to produce, as they have to be chemically pure (absence of light and heavy target contaminants) and deposited on very thin backings to limit the pollution due to reactions on the contaminants and the backing. In Chapter 3, we have stressed the lack of good-quality data on prompt-fission neutron yields as a function of fragment mass and on the odd-even effect to further investigate the energy-sorting process. In this chapter, we will show that a wealth of new high-quality data for surrogate reactions and for fission can be measured via experiments in inverse kinematics with radioactive beams.

1. Transfer-induced reactions with radioactive-ion beams in inverse kinematics

A pioneering transfer-induced fission experiment in inverse kinematics was conducted at GANIL by F. Farget et al. [Caa13, Rod14]. In this experiment a ^{238}U beam at 6.14 A MeV impinged on a ^{12}C target and about 10 heavy actinides ranging from ^{237}U to ^{246}Cm were produced via multinucleon transfer from the carbon target to the ^{238}U projectile. Although the main objective of this experiment was to measure the fission-fragment yields of the produced nuclei, this experiment has demonstrated the feasibility of transfer-induced fission-probability measurements in inverse kinematics. The carbon-like ejectiles were detected with a position-sensitive Si telescope and the fission fragments were detected in coincidence by the VAMOS spectrometer. The VAMOS spectrometer served not only to count the fission fragments but also to identify them isotopically. The fission probabilities as a function of excitation energy of ^{238}U, ^{239}Np, ^{240}Pu, ^{241}Pu, ^{242}Pu, ^{244}Cm were also obtained. They are in good agreement with other results obtained with surrogate reactions in direct kinematics using light-charged projectiles and with neutron-induced data several MeV above the fission threshold. However, important discrepancies were observed at the fission threshold. It is not obvious to attribute these discrepancies to a deficiency of the surrogate-reaction method since this data suffered from a limited excitation-energy resolution of 2.7 MeV (FWHM) and significant uncertainties in the acceptance of the VAMOS spectrometer. The limited excitation-energy resolution was partly due to the uncertainty in the position and the size of the ^{238}U beam. In this experiment, the uncertainty in the position was 2 mm, and the uncertainty in the horizontal and vertical size of the beam was of about 2 and 3 mm, respectively. The typical size spread of the ^{238}U beam delivered by GANIL is 2 mm FWHM in horizontal and vertical positions.

A broad range of possibilities for fission and surrogate-reaction measurements open up with radioactive-ion beam facilities. One of the best suited facilities for surrogate-reaction studies is HIE-ISOLDE. HIE stands for High Intensity and Energy. This is the upgrade of the existing ISOLDE facility at CERN. HIE-ISOLDE will deliver the radioactive beams of ISOLDE with

increased intensity and a maximum beam energy of 10 A MeV, which is particularly well suited for transfer reactions. Table 1 shows some of the pre-actinide beams currently available at ISOLDE. We can see that HIE-ISOLDE will provide actinide beams over isotopic chains of an unprecedented range. Radioactive beams of Ac and Th have also been extracted from the source but not yet post-accelerated.

Element	Isotopic chain	Half lifes
Rn (Z=86)	$^{204\text{-}212}$Rn	$2.4h \leq T_{1/2} \leq 28.5min$
	$^{219\text{-}221}$Rn	$3.96s \leq T_{1/2} \leq 25min$
Fr (Z=87)	$^{207\text{-}213}$Fr	$14.8s \leq T_{1/2} \leq 20min$
	$^{220\text{-}228}$Fr	$27.4s \leq T_{1/2} \leq 21.8min$
Ra (Z=88)	$^{221\text{-}222,224\text{-}226,228}$Ra	$28s \leq T_{1/2} \leq 1600y$

Table 1: Some pre-actinide beams available at ISOLDE.

A letter of intent was sent to the HIE-ISOLDE committee in 2009 by F. Rejmund et al. [Rej09] to study transfer-induced fission. The objective was to measure the fission-fragment element yields, mass yields and total kinetic energy, as well as the fission probability, as a function of the excitation energy for long isotopic chains of pre-actinide and actinide beams. In this work we will present a new fission project where transfer-induced fission is combined with a storage ring.

1.1. Transfer-induced reaction studies at HIE-ISOLDE with the TSR storage ring

Recently, it has been decided to transfer the Test Storage Ring (TSR), initially located at the Max-Planck Institute in Heidelberg, to the HIE-ISOLDE facility, opening unique possibilities for nuclear and atomic physics studies. The physics program and a very detailed study of the feasibility of the coupling of the TSR to HIE-ISOLDE are described in [Gri12].

An essential component of the TSR is the electron cooler which serves to achieve and maintain a small beam emittance, i.e. a beam of reduced size and energy spread. In the electron cooler, the ions scatter with the electrons of an electron gas where the velocity of the electrons is kept equal to the average velocity of the ion beam. In this way, the relative velocities of the ions with respect to the electron gas are reduced. The cooling time is of the order of 1 s, which gives the lower limit in the life time of the ions that can be stored. At the TSR the beam injection proceeds in multiple steps. First the horizontal acceptance of the storage ring is filled with ions. After several tens of revolutions the ions are electron cooled which compresses the phase space and empties a part of the ring acceptance. This emptied phase space is then used to inject new ions. Injection and cooling are alternated until the maximum possible intensity of stored ions is achieved. The maximum intensity is either given by the space charge limit or by the equilibration between the injection rate and the beam loses.

The typical beam-energy resolution expected at HIE-ISOLDE is about 3 MeV for heavy ions (A≈230) and the beam size is of few mm. Thanks to the coupling of HIE-ISOLDE with the TSR a much better beam quality will be obtained. The beam energy resolution can be improved by a factor 14 and the beam size reduced to 1 mm diameter. Besides, the storage ring can be employed for removal of isobaric contaminants. Reaction measurements can be performed inside the storage ring but the cooled beams can also be extracted and exploited by external spectrometers. An essential issue are the loses of the stored ions caused by atomic charge exchange reactions with the atoms of the internal target and residual gas atoms, and by electron capture in the electron cooler. To limit the beam loses, the storage ring has to be operated in ultra-high vacuum (UHV), i.e. a pressure between $4\text{-}6\cdot10^{-11}$ mbar.

Although not included in the physics program detailed in [Gri12], we think that the coupling of the TSR to HIE-ISOLDE offers highly interesting possibilities for surrogate-reaction and fission experiments. We will present these ideas at the next TSR@HIE-ISOLDE workshop in spring 2015.

1.1.1. Measurements inside the TSR

Recent experiments conducted inside the Experimental Storage Ring (ESR) at GSI have demonstrated the feasibility of reaction measurements inside a storage ring using windowless thin gas-jet targets, see e.g. [Sch14-2]. In [Sch14-2], the ^{56}Ni(p,p) and ^{56}Ni(p,p') reactions have been studied by detecting the protons in a particle telescope in coincidence with the recoiling ^{56}Ni. To cope with the demanding vacuum requirements in the storage ring, the ΔE part of the telescope was used as active window separating the UHV from an auxiliary vacuum where non-bakeable components were placed. In this way, additional dead layers were avoided and a low energy threshold was maintained. A number of solutions for combining detector arrays with UHV requirements of a storage ring have been validated by the EXL (EXotic nuclei studied in Light-ion induced reactions at the NESR storage ring) collaboration [Fai06, Moe11]. In particular, an intense program has been conducted to design and construct a recoil detector for target-like ions, which has to fulfil demanding experimental conditions regarding the angular and energy resolution, dynamic range and UHV conditions.

A dedicated gas-jet target will be constructed at HIE-ISOLDE with a maximum thickness of about 10^{14} atoms/cm^2, a reduced spatial extent (less than 1 mm) and light gases as H_2, D_2, ^{3}He and ^{4}He. The limited target thickness and the beam loses are compensated by accumulation and recirculation of the ions inside the ring. Indeed, when equilibrium between the injection rate and beam loses is established, the effective intensity I of the beam circulating inside the storage ring is given by $I = i\varepsilon f\tau$, where i is the intensity of the post accelerated beam in HIE-ISOLDE, ε is the injection efficiency, f is the revolution frequency (about 790 kHz at 10 A MeV) and τ is the is the lifetime of the ions inside the ring, which can be significantly reduced with respect to the nucleus lifetime because of the loses in the electron cooler and in the gas-jet target. We can see that the revolution frequency leads to an increase of the effective intensity of the beam by almost a factor 10^6.

The use of windowless, pure targets represents an enormous advantage for the measurement of decay probabilities, as there will be no pollution from reactions in the target backing or in target contaminants. As shown in Chapter 2, this is one of the most significant complications for the measurements in direct kinematics. In addition, because of the reduced straggling in the target, a better excitation-energy resolution is expected in reaction measurements with an internal target. A good excitation-energy resolution is particularly relevant at the fission threshold, where the fission probability varies rapidly with the excitation energy and sub-barrier structures may be present, see Article IV.

In the following, we will study the feasibility of fission measurements in the storage ring. For this purpose we will consider the simpler case of the interaction of a ^{232}Th beam on a ^{3}He target. Since ^{232}Th is stable, the lifetime and the intensity of the stored beam will be quite high. In addition, the CENBG collaboration has already studied this reaction in direct kinematics [Pet04, Boy06], and the results obtained at the TSR can be compared to the data measured in direct kinematics and to neutron-induced data. The beam energy of 9 A MeV gives the best compromise between the fusion-fission cross section and the elastic scattering cross section. Indeed, the fusion cross section increases very rapidly with the beam energy, whereas the Rutherford elastic cross section decreases with increasing beam energy.

Because of the magnetic rigidity limit of the TSR of $B\rho$ =1.5 Tm, the storage of ^{232}Th ions with a beam energy of 9 A MeV requires a charge state q = 67+. However, the maximum charge state for ^{232}Th that can be produced by the present IBIS source at ISOLDE is q = 53+. Therefore, an upgrade of the IBIS source is needed. In fact, there are many other experiments foreseen at TSR@HIE-ISOLDE that encounter this problem and a charge breeder is under investigation. Once the feasibility of the measurements is established for the ^{232}Th+^{3}He reaction, the proposed method can be extended to radioactive beams. For example, the neutron-rich Fr isotopes are produced with excellent yields by ISOLDE and similar intensities as for ^{232}Th can be obtained.

Reaction	Q-value (MeV)
^{232}Th+^{3}He→^{231}Th+^{4}He	14.14
^{232}Th+^{3}He→^{232}Th+^{3}He’	0
^{232}Th+^{3}He→^{232}Pa+t	-0.513
^{232}Th+^{3}He→^{233}Pa+d	-0.244
^{232}Th+^{3}He→^{234}Pa+p	2.75
^{232}Th+^{3}He→^{235}U	9.46

Table 2: Main reactions that take place when a ^{232}Th beam interacts with a ^{3}He target and the associated Q-values.

At 9 A MeV, the excitation energy available in the centre of mass for the ^{232}Th+^{3}He reaction is the same as for the ^{3}He+^{232}Th reaction in direct kinematics with a ^{3}He beam of 27 MeV. To determine the counting rates for the ^{232}Th + ^{3}He reaction we will use the counting rates of ^{3}He+^{232}Th reaction at 24 MeV, studied in [Pet04, Boy06]. In addition to ^{3}He elastic and inelastic scattering, we expect to populate four main transfer channels and thus produce five

different compound nuclei simultaneously, see Table 2. The difference between the beam energy and the energy of the centre of mass for the ^{232}Th+^{3}He reaction is 26.65 MeV. Given the Q-values for the different transfer reactions considered, shown in Table 2, it is energetically possible to populate a broad excitation-energy distribution ranging from the ground state to energies well above the fission barrier (between 5 and 6 MeV for the nuclei shown in Table 2). There is also a high probability that the ^{232}Th beam fuses with the ^{3}He target nuclei leading to ^{235}U with 36.1 MeV excitation energy. In that case, there will be no target-like nuclei accompanying the reaction products because the probability that the neutron rich ^{235}U evaporates charged particles is very low. Therefore, inelastic and transfer reactions can be unambiguously selected by requiring a coincidence between the target-like nuclei and the reaction products. Note that some of the nuclei formed by transfer reactions between ^{232}Th and ^{3}He are very interesting from the nuclear-data point of view, in particular ^{232,234}Pa. The latter nuclei are formed by neutron absorption of the short-lived ^{231,233}Pa, which are highly relevant for the development of the Th/U cycle.

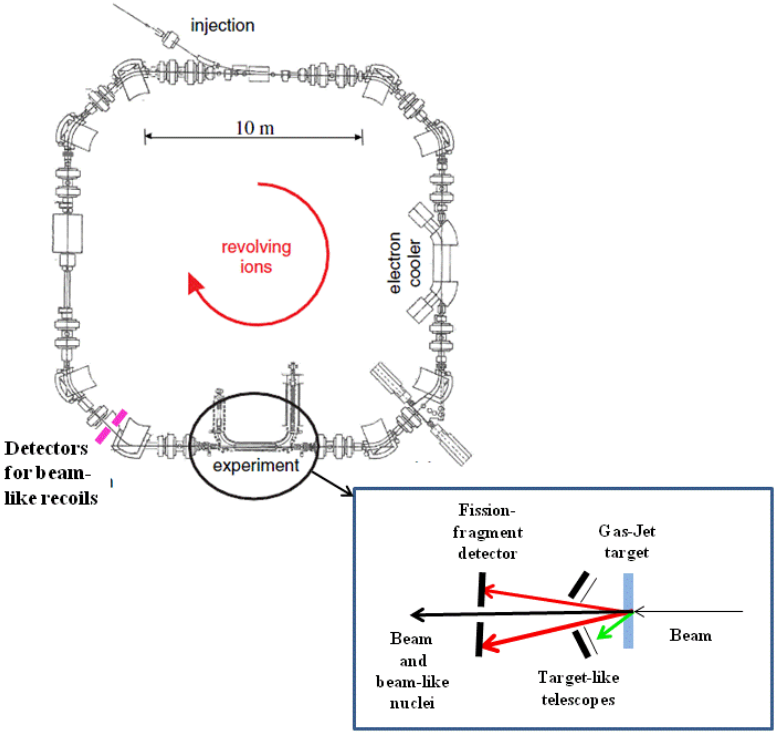

Figure 1: Schematic drawing of the test storage ring (TSR) adopted from [Gri12]. The injection, electron cooler and particle-detector setups are indicated. The inset shows a possible set-up for fission studies. Two particle detectors are schematically shown behind the first dipole after the target to detect the beam-like nuclei.

The maximum number of ^{232}Th ions with q = 67+ and 9 A MeV that can be stored is limited by the charge space of the ion beam and is $2.6 \cdot 10^{8}$ [Gri15]. From previous measurements [Pet04, Boy06], we estimate a cross section for the ^{232}Th(^{3}He,tf) reaction of about 0.5 mb at backward angles (theta centred at 130 degrees). The ^{232}Th(^{3}He,t) reaction is, among all the transfer reactions shown in Table 2, the reaction with the smallest cross section. We need

about 50000 fission coincidence events to have a statistical error in the fission probability of about 5% per excitation-energy bin of 200 keV. Assuming 10% solid angle for the ^{3}He-like telescope and 45% efficiency for the fission detector, we would need a luminosity of about $2.6 \cdot 10^{27}$ cm$^{-2} \cdot$s^{-1} to make a measurement in 10 days. For a target density of 10^{14} atoms/cm^{2} the life time of the stored ^{232}Th beam is too low due to electron capture in the target. Therefore, a reduction of the ^{3}He target thickness from 10^{14} to 10^{13} atoms/cm^{2} should be considered. Assuming a frequency in the ring of 750 kHz [Gri15], the required luminosity implies having $3.5 \cdot 10^{8}$ stored ions, which is rather close to the maximum possible number given above by the charge-space limit. Note that we have considered the most difficult case, at the TSR the situation will be more favourable than in direct kinematics since the ^{3}He-like nuclei can be detected near the grazing angle where the transfer cross sections are higher.

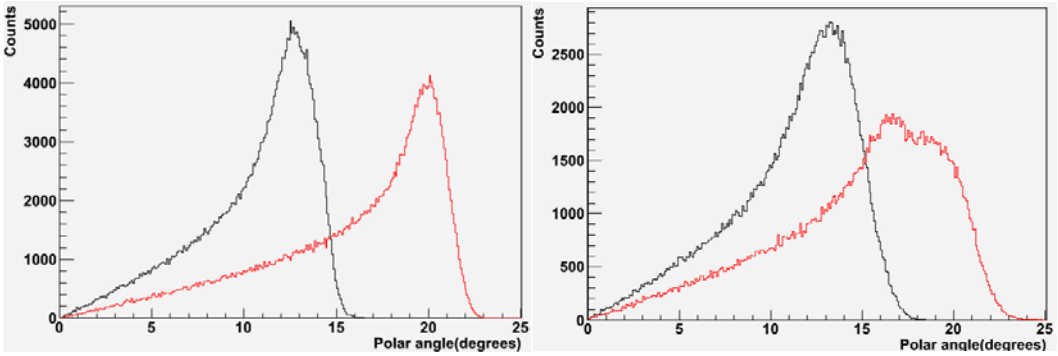

Figure 2: Simulated polar angle of the fission fragments, assuming isotropic emission in the centre of mass. On the left are represented the results for the fission of ^{231}Th at 10 MeV excitation energy and 2020 MeV kinetic energy, and on the right the results for ^{235}U at 33 MeV excitation energy and 2061 MeV kinetic energy. The black spectrum corresponds to the heavy and the red spectrum to the light fission fragment. The kinetic energies of the fission fragments in the centre of mass frame have been calculated with the GEF code [Sch14].

Fig. 1 shows the TSR and a schematic drawing of a possible in-ring set-up for fission-probability measurements. It consists of two Si telescopes to detect the target-like nuclei, followed by a detector for the fission fragments. The target-like telescopes are centred at the grazing angle, which is 42 degrees for the ^{232}Th+^{3}He reaction at 9 A MeV. A simulation performed with the GEF code [Sch14] has shown that for the ^{232}Th(^{3}He,^{4}He) reaction at 9 A MeV and 10 MeV excitation energy the fission fragments are emitted with a maximum polar angle theta of 23 degrees, with 92% of the fragments emitted with polar angles between 5 and 23 degrees, see the left panel of Fig. 2. This curve is representative of the situation for transfer-induced fission. For the fusion-fission reaction, the maximum polar angle is about 23 degrees, see the right side of Fig. 2. The difference in the shape between the left and right panels of Fig. 2 is due to the fact that for ^{231}Th at 10 MeV excitation energy fission is mainly asymmetric, whereas for ^{235}U at 36 MeV there is a significant contribution from symmetric fission. In any case, the simulations show that the fission fragments do not hit the target-like telescope. In addition, most of the fission fragments can be well separated from the beam and the beam-like nuclei produced in the transfer reactions, since the latter are emitted within a

polar cone of less than 1 degree[1]. Both detectors have to be segmented to be able to determine the angle of the detected nuclei.

As discussed in Chapter 2, the excitation energy of the fissioning nuclei can be obtained by measuring the kinetic energy and angle of the ^{3}He-like nuclei. In inverse kinematics there can be a strong dependence of the energy of the ^{3}He-nuclei with the emission angle theta. Fig. 3 shows one example, which is the ^{232}Th(^{3}He,^{4}He) reaction at 5 MeV excitation energy of ^{231}Th. We see that in the range from about 20 to 50 degrees, a variation of the emission angle of one degree implies a change in the kinetic energy of the ^{4}He of about 2 MeV. Therefore, we would need an angular resolution of about 0.1 degree in order to have an excitation-energy resolution of few hundreds keV, which is rather challenging. Another important aspect to consider is the rate of elastic scattered ^{3}He on the telescope, which can considerably deteriorate the energy resolution of the detector because of radiation damage. We estimate this rate to be of about 75 Hz for a Si strip of 1% solid angle located at 5 cm from the target and 20 degrees with respect to the beam axis and about 500 Hz for a strip with the same geometry located at 60 degrees. This rate can be diminished by increasing the distance to the target. One should find the appropriate detector distance, angle and segmentation that give the best compromise between efficiency and energy resolution.

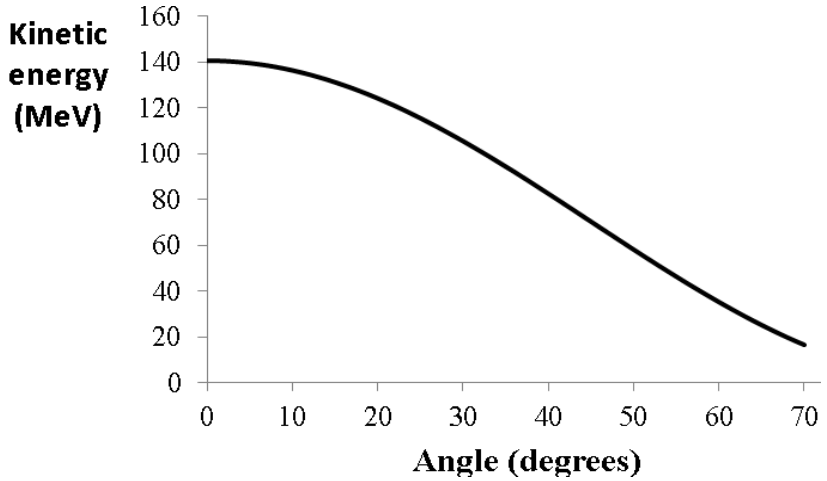

Figure 3 : Kinetic energy as a function of the emission angle for the target-like nucleus of the ^{232}Th+^{3}He→^{231}Th +^{4}He reaction at 9 A MeV and 5 MeV excitation energy of ^{231}Th.

Because of momentum conservation, the light fission fragments are generally emitted with higher velocities than the heavy fission fragments. Therefore, light fragments will be emitted with larger angles than heavy fragments, see Fig. 2. This has interesting consequences for the fission-fragment detection efficiency. If we consider an annular detector for fission with 30 cm diameter and an inner hole of 5 cm of diameter (to let the uncooled beam go through) placed at 35 cm from the target, we would have an efficiency of 97 % for detecting the light fragments and of 95% for detecting the heavy fragments originating from the ^{232}Th(^{3}He,^{4}He)

[1] We neglect the effect of the emission of one or two neutrons and/or gamma rays on the angular spread of the recoiling nuclei.

reaction. In addition, with the appropriate segmentation we could even detect the two complementary fragments in coincidence. Indeed, our simulation shows that at 35 cm both fragments are detected in opposite sides of the detector for 94% of the events. If the same detector is placed as far as 70 cm from the target, the efficiency for detecting the light fragments would be 21% but, because of their smaller polar angles, the efficiency for detecting the heavy fragment is still 53%. However, the number of coincidences is reduced to 19%.

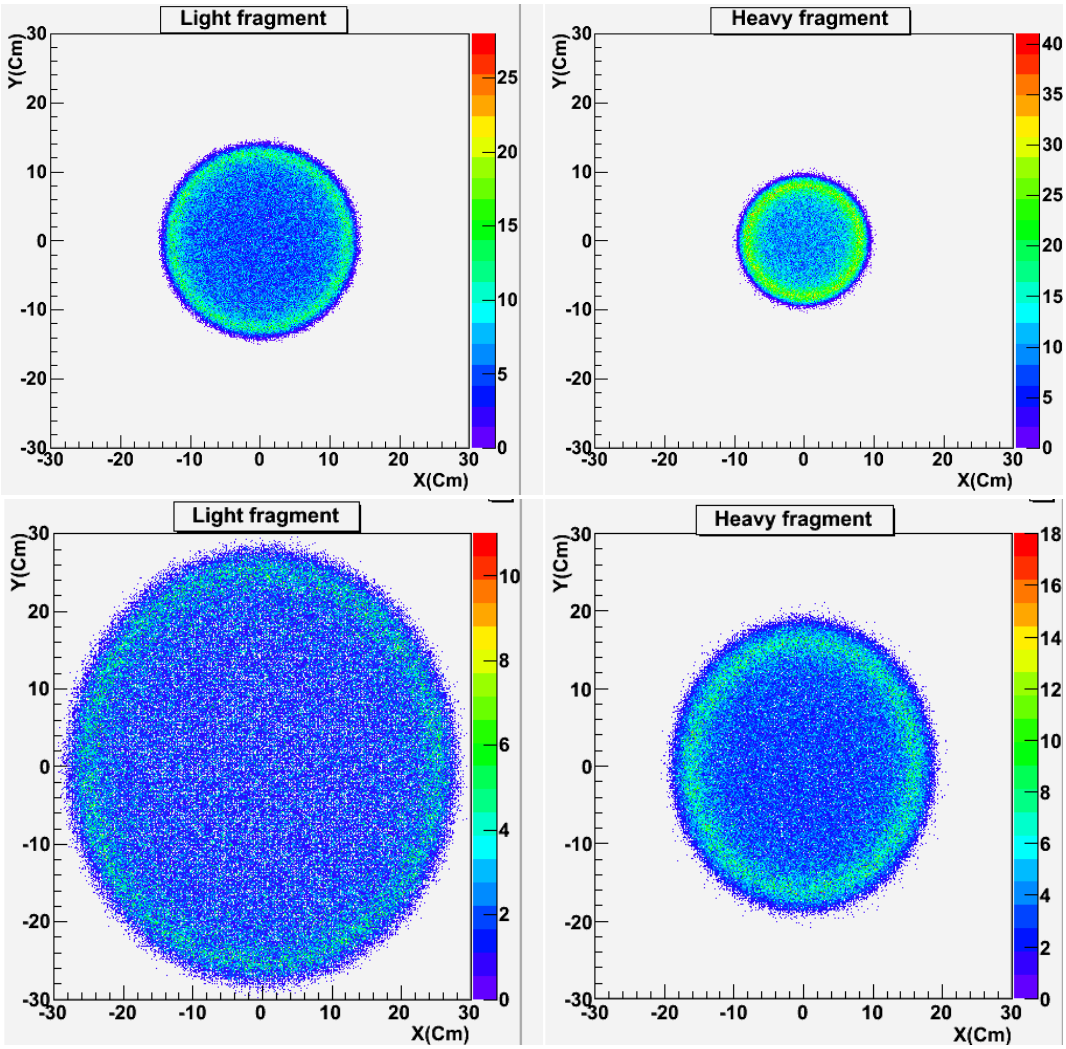

Figure 4: Simulated horizontal and vertical positions on a plane perpendicular to the beam of the fission fragments produced in the fission of ^{231}Th at 10 MeV excitation energy and 2020 MeV kinetic energy. For the upper panels the plane is located at 35 cm from the target and for the lower panels at 70 cm. The kinetic energies of the fission fragments in the centre of mass frame have been obtained with the GEF code [Sch14].

These results can be understood looking at Fig. 4, where the horizontal and vertical positions of the fission fragments in a plane perpendicular to the beam are represented. When the plane is located at 35 cm (upper panels), the vertical positions of light and heavy fragments stay within the outer edge of the detector, which explains the large number of coincidences. On the

other hand, at 70 cm, the majority of the light fission fragments are not intercepted by the detector plane, whereas the heavy fragments are in many cases within the detector limits. The measurement of the fission probability can be done by detecting only one fission fragment. Therefore, using an annular detector of the size given above we can have a relatively good fission efficiency even at rather large distances.

We have to consider the important rate of fusion-fission events. Indeed, while for the ^{232}Th+^{3}He reaction at 9 A MeV we estimate a transfer-induced fission cross section of the order of 10 mb, the fusion-fission cross section is 524 mb, according to PACE4 calculations. With the above-described detector placed at 35 cm from the target we have 97% efficiency for detecting the light fragments and 95% efficiency for detecting the heavy fragments. This gives a rate of about 1.2 kHz of heavy fission fragments originating from fusion-fission impinging on the detector. One possibility would be to use a detector made of photovoltaic cells, as in the experiments described in Chapter 2. We have observed that there is no significant degradation of the spectra in spite of rather high rates of fission fragments coming from fusion-fission reactions. In addition, they have the advantage that they are rather inexpensive, so one can build several arrays with large solid angles at a low cost, which can be replaced when the detector response gets strongly deteriorated. However, we would need to investigate the behaviour of the photovoltaic cells when the fission-fragments energy is about 9 A MeV and not 1 A MeV, as is the case in direct kinematics. With such a detector we would be able to measure fission probabilities and, thanks to the detection in coincidence of complementary fragments, also the total kinetic energy (TKE) of the fragments, which is also very interesting from the fundamental point of view and for applications (see Chapter 3). In fact, the storage ring is particularly well suited for the measurement of the kinetic energy of the fragments because there are no layers of matter between the target and the fission detector and the straggling of the fragments in the gas-jet target and in the UHV is very small.

The energy resolution of the photovoltaic cells is rather limited and they cannot be used to obtain an accurate identification of the fission fragments. However, this can be achieved with good-quality Si telescopes. It has been demonstrated recently [Car12] that using a telescope with silicon detectors of carefully selected properties in terms of doping homogeneity, thickness uniformity and crystal orientation, it is possible to obtain full charge separation from Z=2 to Z=54 at 30 A MeV. Using such a high-quality telescope would allow us to identify at least the light fission fragments in charge, although we have to investigate what would be the Z-separation at 9 A MeV. In low-energy fission no protons are emitted, therefore, with this information we would be able to directly measure, in addition to the fission probability, the fission-fragment elemental yields as a function of excitation energy.

According to our experience, a silicon detector of about 300 mm^2 stands a rate of heavy ions of about 1 kHz for a few days, i.e. 3.33 ions/(s·mm^2). From the right side of Fig. 2 we see that in our case the highest rate will come from the heavy fission fragments with angles ranging from 12 to 14 degrees, which we estimate to be 0.054 ions/(s·mm^2). One can also consider the use of ionization chambers to measure the fragments charge, as they are much less affected by radiation damage. This is technologically quite challenging due to UHV constraints, but the

use of ionization chambers for detecting fission fragments in a storage ring has been studied within the frame of the ELISe project [Tai09].

In some cases, beam-like particles (for example the nuclei produced in the transfer reaction after gamma or neutron emission) can be sufficiently separated from the circulating beam and detected before, inside or after the dipole located after the target, as is schematically represented in Fig. 1. The feasibility of this has been demonstrated in the ESR by detecting the ^{97}Ru recoil ions produced in the ^{96}Ru(p, γ)^{97}Rh reaction [Zho10]. For each particular decay of the compound nuclei formed, one has to evaluate the momentum spread to check whether the measurement is feasible and decide at which position the detectors should be placed. One should in particular consider whether it is possible to separate the beam-like nuclei from other charge states of the beam circulating in the ring and other possible background. In case it would be possible to detect the beam-like nuclei, we would be able to determine simultaneously with the fission probability, the gamma-decay and/or neutron-emission probabilities. This is particularly interesting, the advantage with respect to conventional experiments in direct kinematics to infer the gamma-decay probability, described in Chapter 2, would be having a well-known detection efficiency close to 100%.

The systematic measurement of fission and possibly gamma and neutron-emission probabilities over long isotopic chains would allow us to investigate the influence of the populated angular-momentum distribution on the decay probabilities, since it would be possible to access the same excited nucleus with different transfer reactions. For example, the reactions $_{Z}A(^{3}\mathrm{He,t})$ and $_{Z}A\text{-}1(^{3}\mathrm{He,d})$ lead to the same nucleus $_{Z+1}A$. The comparison of the decay probabilities of the same compound nucleus obtained with different transfer reactions is also interesting for investigating the influence of the breakup of the ^{3}He and of the target-like nuclei, discussed in Chapter 2. Note that the measured fission probabilities can be also used to extract rather direct information on the fission barriers of the produced nuclei and on level densities at very large deformation, see Article IV. Moreover, GSI data on electromagnetic-induced fission [Sch00] have shown the interest of measuring elemental fission-fragment yields over long isotopic chains to study the influence of deformed shells on the fission process. Two important advantages of the proposed measurements are the extension towards unknown regions of the chart of nuclei and the possibility to study also the evolution of fission observables with the excitation energy, which is not possible in current GSI measurements.

1.1.2. Measurements with extracted beams from the TSR

To measure the prompt-fission neutron multiplicity as a function of the fragment mass $<\nu(A)>$ one needs setups involving large detectors, long flight paths of several meters or a dipole magnet with sufficient acceptance and bending power. These types of setups are not well adapted for in-ring experiments because of the limited space. Therefore, for these measurements it is necessary to use the extracted cooled beams from the TSR. The quality of the extracted beams is somewhat deteriorated by the extraction procedure and the beam

intensity is reduced by about a factor 10 with respect to the intensity inside the ring. In this section we will describe briefly the method to determine $<\nu(A)>$ and possible setups.

$<\nu(A)>$ can be determined indirectly as the difference between the fission-fragment mass before A_{pre} and after A_{post} prompt-neutron emission, which can be obtained from the measurement of the kinetic energy and the velocity of the complementary fragments in coincidence, see e.g. [Ter62, Mül84]. In low-energy fission, prompt neutrons are emitted within 10^{-18} and 10^{-14} s and we can only directly measure quantities after prompt-neutron emission. Therefore, with the kinetic energies and the velocities of both fragments we can in principle only determine A_{post}. However, if we assume that prompt neutrons are emitted isotropically, their emission will not modify on average the velocity of the fragments. Therefore, the average velocity of the fission fragments of a given mass after prompt neutron emission $<V_{post}(A)>$ is equal to the velocity of the fragments before prompt-neutron emission $V_{pre}(A)$. Then, applying momentum and mass conservation we have:

$$\begin{aligned} &A_{1,pre} \cdot V_{1,pre} = A_{1,pre} \cdot <V_{1,post}> = A_{2,pre} \cdot V_{2,pre} = A_{2,pre} \cdot <V_{2,post}> \\ &A_{1,pre} + A_{2,pre} = A_{CN} \end{aligned} \qquad (1)$$

where A_{CN} is the mass of the fissioning nucleus, which is known from the identification of the target-like nuclei in the telescope. From eqs. (1) it is possible to the deduce $A_{i,pre}$. As $<\nu(A)>$ is only about 1% of the fragment masses (see Chapter 3), it is essential that the mean masses $<A_{i,pre}>$ and $<A_{i,post}>$ are determined to 0.1 % or better.

The needed experimental set-up should provide the mass, charge and excitation energy of the fissioning nucleus, as well as the time-of-flight (TOF), the flight length and the kinetic energies of both fragments in coincidence. We think that a good target choice could be a ^{12}C target as in [Rod14]. With this target it is possible to populate about 10 different transfer channels simultaneously and produce fissioning nuclei several nucleons heavier that the beam. A telescope placed few centimetres downstream of the target and covering the grazing angle may be used to isotopically identify the carbon-like nuclei and measure their kinetic energies and emission angles. The remaining setup could be similar to the one proposed in [Rej09]. It could consist of two arms located after the target-like telescope to detect the two fission fragments in coincidence. Each arm would consist of a position sensitive detector like e.g. a Multi Channel Plate (MCP) or a Secondary Electron Detector (SED) [Dro02] that would also serve as a start detector for the TOF measurement. At the end of the arm we may place another SED that would provide the other position measurement and the stop signal for the TOF, followed by a Si wall to stop the fission fragments and provide their kinetic energies. The length of the flight path should be the one that gives the best compromise between the TOF resolution and the fission-detection efficiency of the setup. In any case, the reduced emittance of the extracted TSR beams will considerably help to obtain the required mass resolution. As suggested in [Rej09], a more advanced version of the setup could include a dipole magnet and a ionisation chamber in each arm, which would allow us to measure $A_{i,post}$ with better resolution using the Bρ-ΔE-TOF technique as in the GANIL [Caa13] and the

SOFIA experiments [Tai15]. This more advanced set-up would also provide the charges of the fission fragments. Moreover, if the fission-detection efficiency is well known, the two described setups would allow us to measure also the fission probability.

Note that multi-chance fission, i.e. neutron emission prior to fission, complicates the indirect measurement of $<\nu(A)>$ because it induces an uncertainty in the mass of the fissioning nucleus A_{CN}. Therefore, $<\nu(A)>$ can only be determined indirectly for excitation energies below the onset of second chance fission (about 10-12 MeV). Measurements at higher excitation energies would require the direct detection of the prompt neutrons.

One should also take into account that the use of a carbon target is associated with some difficulties. As discussed in Chapter 2, the use of a carbon target induces an uncertainty in the excitation energy of the fissioning nuclei because, as demonstrated in [Rod14], in some cases the carbon-like nuclei can be excited. In addition, one has to deal with the possible oxygen contamination in the target. Finally, it is important to take into account that the populated transfer reactions are much more difficult to model than the transfer reactions involving a ^{3}He target. This complicates considerably the interpretation of the results for the fission probability regarding the angular-momentum dependence and the use of the fission probability to infer the fission barriers.

2. Long-term perspectives

The technical developments performed within the frame of our project at TSR@HIE-ISOLDE can be very useful for the realisation of two highly interesting future facilities.

As proposed by Reifarth and Litvinov [Rei14], a real breakthrough in the measurement of neutron-induced cross sections of short-lived nuclei would be possible by coupling an ISOL facility with a storage ring to a nuclear reactor. The reactor would serve to fill in permanence a certain volume of the storage ring with a gas of neutrons practically at rest, thus providing a neutron target. Such a facility would make possible the measurement of neutron-induced cross sections in inverse kinematics for beams with half lifes of only few minutes or even less. Capture cross sections could be measured using Schottky spectroscopy, and two-neutron emission and charged-particle-emission cross sections could be obtained by detecting the beam-like products at the appropriate positions inside the ring. Because of the rather isotropic emission of the fission fragments in the centre of mass, the study of neutron-induced fission with this facility is only possible with a reasonable efficiency for beam energies beyond few A MeV.

Fission experiments complementary to the ones presented in this chapter will be possible at the ELISe (ELectron-Ion scattering in a Storage ring – eA collider) [Ant11] facility of the future instrumental complex FAIR (Facility for Ion Research) at GSI, Germany. The ELISe facility is designed as a high-luminosity heavy ion-electron collider. It consists of the coupling of the New Experimental Storage Ring (NESR) with an electron accelerator. The electron-ion collision A(e,e')A^* allows to produce excited heavy ions with excitation energies

between 0 and 20 MeV. The scattered electrons are detected with an electron recoil spectrometer, providing a measurement of the excitation energy of the actinide. A specific set-up for fission measurements at ELISe called F-ELISe is presented in [Tai09]. This setup is very close to the set-up of the SOFIA experiment [Tai15] and would allow the full identification of the fission fragments. The mayor progress of F-ELISe with respect to SOFIA is the determination of the excitation energy of the fissioning nucleus.

3. Conclusions

We have presented a new project to measure fission data by using the HIE-ISOLDE radioactive beams in combination with the TSR storage ring. The data includes decay probabilities, fission-fragment yields and prompt-fission neutron multiplicities. The systematic study of these observables over long isotopic chains of fissioning nuclei and as a function of excitation energy can significantly contribute to our understanding of the fission process, and decay processes in general. In the long term, a new era of experiments will be possible by coupling heavy-ion storage rings to a nuclear reactor or to an electron accelerator.

As illustrated by [Sch00, Caa13, Tai15], the development of highly complicated facilities able to produce and accelerate radioactive beams, and of advanced experimental methods to detect the fission fragments has opened up very important new possibilities for experiments on nuclear fission. They are to a great extent at the origin of a revival of the research on nuclear fission. The experiments we have proposed add an additional degree of sophistication by the coupling to a storage ring and prove that the steps done up to now can still be extended.

References

[Agv04] U. Agvaanluvsan et al., Phys. Rev. C 70, 054611 (2004)

[And70] B. L. Andersen, B. B. Back and J. M. Bang, Nucl. Phys. A 147 (1970) 33

[Ant11] A.N. Antonov et al., Nucl. Instr. and Meth. A 637 (2011) 60

[Asg84] M. Asghar and R. W. Hasse, J. Phys. Colloques 45, C6-455 (1984)

[Bau00] E. Bauge, et al., Phys. Rev. *C* 61 (2000) 034306

[Bau01] E. Bauge, J.P. Delaroche, M. Girod, Phys. Rev. C 63 (2001) 024607

[Bet36] H. A. Bethe, Phys. Rev. 50, 332 (1936)

[Boh36] N. Bohr, Nature 137 (1936) 344

[Boh98] A. Bohr and B. R. Mottelson, Nuclear Structure Vol. II, 1998 World Scientific

[Boy06] S. Boyer et al., Nucl. Phys. A 775 (2006) 175

[Bis70] C. J. Bishop, R. Vandenbosch, R. Aley, R. W. Shaw Jr., I. Halpern, Nucl. Phys. A 150, 129 (1970)

[Bri70] H. C. Britt and J. D. Cramer, Phys. Rev. C 2 (1970) 1758

[Bro90] U. Brosa, S. Grossmann, and A. Mueller, Phys. Rep. 197, 167 (1990)

[Bür12] A. Bürger et al., Phys. Rev. C 85, 064328 (2012)

[Bur70] S. C. Burnett, R. L. Ferguson, F. Plasil, H. W. Schmitt, Phys. Rev. C 3, 2034 (1970)

[Caa11] M. Caamano, F. Rejmund and K.-H. Schmidt, J. Phys. G: Nucl. Part. Phys. 38, 035101 (2011)

[Caa13] M. Caamano, O. Delaunne, F. Farget et al., Phys. Rev. C 88, 024605 (2013)

[Cap09] R. Capote et al., Nucl. Data Sheets 110 (2009) 3107

[Cap13] R. Capote, private communication (2013)

[Car14] B. V Carlson, J. E. Escher and M. S. Hussein, J. Phys. G: Nucl. Part. Phys. 41 (2014) 094003 (21pp)

[Cea14] CEA Energy Handbook, CEA Saclay, France (2014) (www.cea.fr)

[Cra70] J. D. Cramer, H. C. Britt, Nucl. Sci. Eng. 41 (1970) 177

[Dab83] J. W. T. Dabbs et al., Nucl. Sci. Eng. 83 (1983) 2

[Des10] P. Descouvemont and D. Baye, Rep. Prog. Phys. 73 (2010) 036301 (44pp)

[Diu01] B. Diu, C. Guthmann, D. Lederer, B. Roulet, “Physique Statistique”, Collection Enseignement des sciences, 37, Paris (2001)

[Dro02] A. Drouart et al., Nucl. Instr. Meth. A 477 (2002) 401]

[Duc15] PhD Thesis of Q. Ducasse, Université de Bordeaux (2015)

[Esc06] J. E. Escher and F. S. Dietrich, Phys. Rev. C 74 (2006) 054601

[Esc12] J. E. Escher et al., Rev. Mod. Phys. 84 (2012) 353

[Esc13] J. Escher et al., contribution to the CNR*13 Workshop, October 2013, Sao Paulo, Brazil

[Egi05] T. von Egidy, D. Bucurescu, Phys. Rev. C 72, 044311 (2005)

[Fai06] FAIR Baseline Technical Report 2006

[Fes54] H. Feshbach, C. E. Porter and V. F. Weisskopf, Phys. Rev. 96 (1954) 448

[Gai91] J. –J. Gaimard and K.-H. Schmidt, Nucl. Phys. A 531 (1991) 709

[Gav76] A. Gavron et al., Phys. Rev. C 13 (1976) 2374

[Gil65] A. Gilbert, A. G. W. Cameron , Can. J. Phys. 43, 1446 (1965)

[Gou05] H. Goutte, J. F. Berger P. Casoli, D. Gogny, Phys. Rev. C 71 (2005) 024316

[Gri12] M. Grieser et al., Eur. Phys. J. Special Topics 207 (2012) 1-117

[Gri15] M. Grieser, private communication (2015)

[Gut00] M. Guttormsen et al., Phys. Rev. C 61 (2000) 067302

[Gut01] M. Guttormsen, M. Hjorth-Jensen, E. Melby, J. Rekstad, A. Schiller, and S. Siem, Phys. Rev. C 63, 044301 (2001)

[Gut03] M. Guttormsen et al., Phys. Rev. C68, 064306 (2003)

[Gut11] M. Guttormsen et al., Phys. Rev. C 83, 014312 (2011)

[Gut11-2] M. Guttormsen et al., Nucl. Instr. Meth. A 648 (2011)168

[Hau52] W. Hauser and H. Feshbach, Phys. Rev. 87 (1952) 366

[Hod87] P. E. Hodgson, Rep. Prog. Phys. 50 (1987) 1171-1228

[Ign75] A. V. Ignatyuk et al., Sov. J. Nucl. Phys. 21 (1975) 612

[Ign82] A. V. Ignatyuk, K. K. Istekov, G. N. Smirenkin, Sov. J. Nucl. Phys. 36, 32 (1982)

[Jur10] B. Jurado, G. Barreau and C.-O. Bacri, Nucl. Instr. Meth. A 613 (2010) 343

[Kar08] A. V. Karpov, A. Kelic, K.-H. Schmidt, J. Phys. G: Nucl. Part. Phys. 35 (2008) 035104

[Kaw08] T. Kawano et al., Nucl. Data Sheets 109 (2008) 2817

[Kno00] G. F. Knoll, Radiation, detection and measurement, third edition (2000) John Wiley & sons, Inc.

[Kra01] H. J. Krappe and S. Fadeev, Nucl. Phys. A 690 (2001) 431

[Lar06] A.C. Larsen et al., Phys. Rev. C 73, 064301 (2006)

[Lar07] A. C. Larsen et al., Phys. Rev. C 76, 044303 (2007)

[Lar11] A. C. Larsen et al., Phys. Rev. C 83, 034315 (2011)

[Lem05] S. Lemaire, P. Talou, T. Kawano, M.B. Chadwick, D.G. Madland, Phys. Rev. C 72, 024601 (2005)

[Lew75] M. B. Lewis, Phys. Rev. C 11 (1975) 145

[Lit10] O. Litaize and O. Serot, Phys. Rev. C 82, 054616 (2010)

[Lyl07] B. F. Lyles et al., Phys. Rev. C 76 (2007) 014606

[Mad82] D. G. Madland and J. R. Nix, Nucl. Sci. Eng. 81, 213 (1982)

[Meo13] V. Méot, private communication, (2013)

[Mir09] M. Mirea, Phys. Lett. B 680, 316 (2009)

[Mit10] G. E. Mitchell, A. Richter, and H. A. Weidenmüller, Rev. Mod. Phys. 82 (2010) 2845

[Moe11] H. Moeini et al., Nucl. Instr. Meth. A 634 (2011) 77

[Möl01] P. Möller, D. G. Madland, A. J. Sierk, A. Iwamoto, Nature 409 (2001) 785

[Möl14] P. Möller, J. Randrup, A. Iwamoto and T. Ichikawa, Phys. Rev. C 90, 014601(2014)

[Mor13] B. Morrillon, private communication (2013)

[Mor15] A. Moro and J. Lei, private communication (2015)

[Mos71] U. Mosel and H. W. Schmitt, Nucl. Phys. A 165, 73 (1971)

[Mos71-2] U. Mosel, J. Maruhn and W. Greiner, Phys. Lett. B 34, 587 (1971)

[Mül84] R. Müller, A. A. Naqvi, F. Käppeler, F. Dickmann, Phys. Rev. C 29, 885 (1984)

[Mye97] W. D. Myers and W. J. Swiatecki, Nucl. Phys. A 612, 249 (1997)

[Naq86] A. A. Naqvi, F. Käppeler, F. Dickmann, R. Müller, Phys. Rev. C 34, 218 (1986).

[Nix65] J. R. Nix and W. J. Swiatecki, Nucl. Phys. 71, 1 (1965).

[Nyh12] H.T. Nyhus, Phys. Rev. C 85 (2012) 014323

[Pet04] M. Petit et al., Nucl. Phys. A 735 (2004) 345

[Ple05] C. Plettner et al., Phys. Rev. C 71 (2005) 051602 (R).

[Rag84] I. Ragnarsson and R. K. Sheline, Phys. Scr. 29, 385 (1984)

[Ran09] J. Randrup, R. Vogt, Phys. Rev. C 80, 024601 (2009)

[Ran11] J. Randrup, P. Möller, Phys. Rev. Lett. 106 (2011) 132503

[Rej09] F. Rejmund, et al. Letter of Intent to HIE-ISOLDE, "Transfer-induced reactions with radioactive-ion beams in inverse kinematics", 2009.

[Rei14] R. Reifarth and Y. Litvinov, Phys. Rev. ST Accel. Beams 17, 014701 (2014)

[Rei14-2] R. Reifarth, C. Lederer and K. Käppeler, J. Phys. G: Nucl. Part. Phys. 41 (2014) 053101 (42pp)

[Rod14] C. Rodriguez-Tajes, F. Farget et al., Phys. Rev. C 89, 024614 (2014)

[Rom12] P. Romain et al., Phys. Rev. C 85 (2012) 044603

[Rom13] P. Romain, private communication (2013)

[Sci10] N. D. Scielzo et al., Phys. Rev. C 81 (2010) 034608

[Sch01] A. Schiller et al., Phys. Rev. C 63, 021306 (R) (2001)

[Sch00] K.-H. Schmidt et al., Nucl. Phys. A 665, 221 (2000)

[Sch14] K.-H. Schmidt, B. Jurado, Ch. Amouroux, "The GEneral Fission model (GEF)", JEFF-Report 24, NEA Data Bank (June 2014) available from https://www.oecd-nea.org/databank/docs/2014/db-doc2014-1.pdf
See also: www.in2p3.fr/GEF or http://www.khs-erzhausen.de/GEF

[Sch14-2] M. von Schmid et al., EPJ Web of Conferences 66, 03093 (2014)

[Sim14] C. Simenel and A. S. Umar, Phys. Rev. C 89 (2014) 031601 (R)

[Ste98] S. Steinhäuser et al. Nucl. Phys. A 634 (1998) 89

[Str90] M. Strecker, R. Wien, P. Plischke, W. Scobel, Phys. Rev. C 41, 2172 (1990)

[Str58] V.M. Strutinsky, in: Proc. Int. Conf. Nucl. Phys., Paris (1958) 617

[Str68] V. M. Strutinsky, Nucl. Phys. A 122, 1 (1968)

[Svi06] M.I. Svirin, Phys. Part. Nucl. 37 (2006) 475

[Sye09] N. U. H. Syed et al., Phys. Rev. C 80, 044309 (2009)

[Tai09] J. Taieb et al., Int. J. Mod. Phys. E, 18 (2009) 767

[Tai15] J. Taieb et al., submitted to Phys. Rev. Lett. (2015)

[Tal10] P. Talou and T. Kawano, EPJ Web of Conferences 2, 08005 (2010)

[Ter62] J. Terrell, Phys. Rev. 127 (1962) 880

[Tof10] H. K. Toft, A. C. Larsen, U. Agvaanluvsan, A. Buerger, M. Guttormsen, G. E. Mitchell, H. T. Nyhus, A. Schiller, S. Siem, N. U. H. Syed, A. Voinov, Phys. Rev. C 81, 064311 (2010)

[Tho06] I. Thompson and J. Escher, Technical Report UCRL-TR-225984, Lawrence Livermore National Laboratory, 2006

[Tor14] T.G. Tornyi et al., Nucl. Isntr. Meth. A 738 (2014) 6

[Tra72] B. L. Tracy et al., Phys. Rev. C 5, 222 (1972)

[Vag71] Z. Vager, Phys. Lett. B 36 (1971) 269

[Wah88] A. C. Wahl, Atom. Data Nucl. Data Tables 39, 1 (1988)

[Wei09] H. A. Weidenmüller and G. E. Mitchell, Rev. Mod. Phys. 81 (2009) 539

[Wig38] E. Wigner, Trans. Faraday Soc. 34, part 1, 29 (1938)

[Wik76] B. D. Wilkins et al., Phys. Rev. C 14, 1832 (1976)